CHARACTERIZING THE CORRELATION BETWEEN MOTOR CORTICAL NEURAL FIRING AND GRASPING KINEMATICS

by

M. Chance Spalding

B.S. Biological Sciences, Ohio University, 2001

D.O., Ohio University, 2010

Submitted to the Graduate Faculty of

the Swanson School of Engineering in partial fulfillment

of the requirements for the degree of

Doctor of Philosophy

University of Pittsburgh

2010

UNIVERSITY OF PITTSBURGH

SWANSON SCHOOL OF ENGINEERING

This dissertation was presented

by

M. Chance Spalding, Ph.D.

It was defended on

June 3, 2010

and approved by

Aaron Batista, Ph.D., Assistant Professor, Department of Bioengineering

Douglas J. Weber, Ph.D., Assistant Professor, Department of PM&R

Marco Santello, Ph.D., Professor, School of Biological and Health Systems Engineering

Robert E. Kass, Ph.D., Professor, Department of Statistics

Dissertation Director: Andrew B. Schwartz, Ph.D., Professor, Department of Neurobiology

CHARACTERIZING THE CORRELATION BETWEEN MOTOR CORTICAL NEURAL FIRING AND GRASPING KINEMATICS

M. Chance Spalding, Ph.D.

University of Pittsburgh, 2010

The hand has evolved to allow specialized interactions with our surroundings that define much of what makes us human. Comprised of numerous joints allowing 23 separate degrees-of-freedom (DoFs) (joint motions) of movement, the hand and wrist are exceedingly complex. In order to better understand the constraints and principles underlying the neural control of the hand, we have carried out a series of neurophysiological experiments with monkeys performing a variety of reaching and grasping tasks. This work uses linear regression and low dimensional analysis to probe the neural representation of hand kinematics.

We find that the kinematics of the three wrist DoFs (flexion, abduction and rotation) are rashly independent from hand-shape DoFs, and are considered separately. With respect to the wrist DoFs, we show that the firing patterns of individual motor cortical cells are more linearly related to joint position than joint angular velocity. Using tuning functions from multivariate linear regressions, the firing rates from a population of cells accurately predicted three DoFs of wrist orientation. We used principal components analysis to simplify the complex kinematics of the hand. Although the majority of the variability in hand kinematics can be explained with a small number (~7) of characteristic hand shapes (synergies), we find that these synergies do not capture the majority of neural variability. Both higher-order and lower-order synergies are well represented in the neural data. Although the kinematic synergies do not fully characterize neural firing, they can be utilized to simplify hand shape decoding. Using an optimal linear estimator,

we predicted the average wrist and hand shape from the firing rates of 327 motor cortical cells with an accuracy as high as 92%.

Individual motor cortical neurons are not well correlated with single joint variables; rather, they correlate with a number of joints in a complex way. This work provides evidence that hand movements are likely controlled through an intricate network of motor systems, of which motor cortical neurons contribute by making fine adjustments to a basic substrate. Further understanding of the control system will be gained by establishing a model that captures both the hand kinematic and neural variability.

TABLE OF CONTENTS

PREFACE ..... **XIV**

1.0 INTRODUCTION AND BACKGROUND **1**

1.1 PROSTHETICS AND CLINICAL SIGNIFICANCE **8**

2.0 METHODS **10**

2.1 BEHAVIORAL SETUP **10**

2.2 KINEMATIC DATA COLLECTION **16**

2.3 ESTIMATING JOINT ANGLES **18**

2.3.1 Model Labeling **19**

2.3.2 Calculating Joint Angles **22**

2.3.3 Joint Center Estimations **25**

2.4 SURGICAL PROCEDURE **28**

2.5 NEURAL DATA PROCESSING **32**

2.5.1 Neural Recording **32**

2.5.2 Fractional-interval firing rates **36**

2.5.3 Kinematic and Neural data processing **38**

2.6 EXPERIMENTAL DETAILS **44**

3.0 KINEMATIC ANALYSIS AND GRASP SYNERGIES **46**

3.1 OBJECT SELECTION **49**

3.2 JOINT ANGLE ACCURACY 52

3.3 DIMENSIONALITY REDUCTION 57

3.3.1 Intuitive Kinematic Analysis 57

3.3.2 Basics of Dimensionality Reduction 64

3.3.3 Application of PCA to Grasping Data 65

3.4 STATIC GRASPING SYNERGIES IN JOINT ANGLE SPACE 70

3.4.1 What data points, and how many descriptors for PCA 71

3.4.2 Postural Synergies 77

3.5 DISCUSSION 82

4.0 CORRELATION BETWEEN SPIKING ACTIVITY IN MOTOR CORTEX AND WRIST DOFS 84

4.1 WRISTDATA OVERVIEW 85

4.1.1 Wrist Kinematics – Isolated Degrees of Freedom 88

4.1.2 Wrist Kinematics – Joint Correlations 94

4.2 INDIVIDUAL DEGREE OF FREEDOM TUNING 101

4.2.1 Motor cortical spiking correlation between position and velocity variables 103

4.3 MULTIPLE DEGREE OF FREEDOM TUNING 108

4.4 PREDICTING WRIST JOINT ANGLE FROM POPULATIONS OF MOTOR CORTICAL CELL SPIKING ACTIVITY 115

4.5 DISCUSSION 125

5.0 GRASPING KINEMATICS CORRELATION TO THE SPIKING ACTIVITY OF SINGLE MOTOR CORTICAL CELLS 128

5.1 SPIKING ACTIVITY AS A LINEAR FUNCTION OF JOINT POSITION, JOINT VELOCITY, AND GRASP SYNERGIES 131

5.1.1 Multiple Degree of freedom tuning 132

5.2 PREDICTING HAND SHAPE AND WRIST ORIENTATION FROM THE SPIKING ACTIVITY OF A POPULATION OF MOTOR CORTICAL CELLS 139

5.3 SYNERGY CORRELATIONS WITH MOTOR CORTICAL FIRING ... 148

5.4 DISCUSSION 157

6.0 CONCLUSIONS 160

6.1 SUMMARY OF MAIN CONCLUSIONS 160

6.2 FUTURE WORK 163

6.2.1 Lower dimensional representation of neural data 163

6.2.2 Furthering the current study 163

6.2.3 Motor restorative devices 164

BIBLIOGRAPHY 166

LIST OF TABLES

Table 1. Sample of the files and number of cells recorded. 35

Table 2. Object names and orientations. 86

Table 3. Wrist DoFs paired correlation. Early versus late training. 99

LIST OF FIGURES

Figure 1. Representation of the behavioral setup..... 11

Figure 2. Motion tracking glove. 12

Figure 3. Tool changing mechanism for object presentations. 13

Figure 4. Progression of a reach-to-grasp trial..... 14

Figure 5. Marker data displayed in the grasp viewer. 20

Figure 6. Marker data correction in Grasp Viewer. 21

Figure 7. Segment marker placement. 22

Figure 8. Joint angle calculations - two markers per segment. 23

Figure 9. Joint angle calculations - one marker per segment. 24

Figure 10. Simplified joint center estimation. 25

Figure 11. Re-sampled marker data used for joint center estimation. 27

Figure 12. Chamber surround. 29

Figure 13. Implantation of chamber surrounds and head posts. 31

Figure 14. Penetration sites in relation to central sulcus. 33

Figure 15. Fractional interval spike rates. 37

Figure 16. Trajectories across days..... 39

Figure 17. MCP1 flexion over many days 40

Figure 18. Hand angle and velocity 41
Figure 19. Aligned joint velocity tracings 43
Figure 20. Graphical representation of objects. 45
Figure 21. Continuous real-time joint angle data..... 48
Figure 22. Joint angle excursion as a function of object..... 50
Figure 23. Cost analysis for original and final object set. 51
Figure 24. Marker movement with markers placed directly above a joint. 53
Figure 25. Joint angle calculation and graphic of joint angle error estimation..... 54
Figure 26. Marker movement with inter-segmental marker placement. 56
Figure 27. MCP1 joint movements. 58
Figure 28. Correlated grasping movement..... 60
Figure 29. Joint angle correlation matrix. 62
Figure 30. Joint angle covariance matrix. 63
Figure 31. Dimensionality reduction example. 64
Figure 32 Hand shape projections onto the first four eigenvectors. 69
Figure 33. Data points used in PCA – reconstruction comparison. 73
Figure 34. SVM object classification using the complete joint angle data set. 74
Figure 35. SVM Classification based on the first eigenvector. 75
Figure 36. Object classification from eigenvectors. 76
Figure 37. Angle data used in PCA. 78
Figure 38. Joint angle variance explained from first 9 eigenvectors. 79
Figure 39. Correlation between actual and reconstructed joint angle data. 80
Figure 40. Object orientations..... 87

Figure 41. Possible wrist DoFs range and actual. 88

Figure 42. Wrist angles over consecutive trials. 89

Figure 43. Wrist DoFs - single and multiple presentations. 91

Figure 44. Aligned wrist angular velocities over many trials. 93

Figure 45. Wrist flexion joint angular velocity vs. joint angle. 94

Figure 46. Wrist angle correlations as a function of training. 96

Figure 47. Wrist DoFs paired correlation. 98

Figure 48. Wrist DoFs correlation over training sessions 100

Figure 49. Number of trials completed per day. 101

Figure 50. Motor cortical cell firing- wrist flexion angle. 103

Figure 51. Motor cortical cell firing- with abduction velocity. 104

Figure 52. Angular velocity R^2 vs. angle R^2 106

Figure 53. Position and velocity correlation difference histograms. 107

Figure 54. Position histograms. 109

Figure 55. Velocity histograms. 111

Figure 56. Position correlation histograms. 113

Figure 57. Firing rate versus predicted firing rate. 114

Figure 58. R^2 distribution for cells used for wrist predictions. 116

Figure 59. Three dimensional wrist angle preferred direction vectors. 117

Figure 60. Uniformity of preferred directions. 119

Figure 61. Predicted versus actual wrist orientation. 122

Figure 62. Cross validation of wrist decoding model 124

Figure 63. Accuracy of prediction across all presentations. 125

Figure 64. Object related spiking activity. 130

Figure 65. Joint names and corresponding numbers. 134

Figure 66. Multiple linear regressions – joint position. 135

Figure 67. Multiple linear regressions – joint angular velocity. 136

Figure 68. Multiple linear regression – reconstructed joint angles from a few synergies. 137

Figure 69. Difference in R^2 – position, velocity and reconstructed hand shape. 138

Figure 70. Distribution of correlation coefficients – entire population. 140

Figure 71. Predicted vs. reconstructed hand shape- small handle. 144

Figure 72. Joint angle prediction correlation as a function of object presentation. 145

Figure 73. Correlation between actual and predicted hand shape. 146

Figure 74. Correlation between actual and reconstructed joint angles for all eigenvectors. 147

Figure 75. Example R^2 profiles. 149

Figure 76. Average R^2 profile for all cells. 150

Figure 77. Best correlated synergies. 152

Figure 78. Top three synergies for joint and synergy cells. 154

Figure 79. Best synergy as a function of penetration site. 156

Figure 80. Best synergy as a function of chamber position. 157

PREFACE

I would like to take this opportunity to thank all of the people who have helped me both academically and emotionally.

First and foremost I thank my family, especially my wife, for giving me the encouragement and freedom to pursue a longtime passion. Her relentless pursuit to appear interested while listening to my latest struggle was most inspiring. I thank my Pittsburgh family for the frequent breaks, general fun, and most importantly good food. In addition, I thank my advisor, Andrew Schwartz, for taking a chance on my abilities, for his guidance, and consistently advocating for my success. Finally, I would like to thank Steve Chase, my second reader, for helping transform this document from a strong anesthetic into a mild sedative.

I would also like to acknowledge all of the members of our team who worked in the motor lab, both past and present. Without their support and hard work the completion of this project would not have been possible. I owe a tremendous debt of gratitude to Meel Velliste, Beata Jarosiewicz, Michael Palazzolo, Samuel Clanton, Andrew Whitford, Sagi Perel, Marco Wu, George Fraser, Jeong-Woo Sohn, Angus McMorland, Jeffrey Graybill, Michael Handke, Edgar Ecu, and Ingrid Albrecht. Most importantly, I would like to extend a heart-felt thank you to Laurel Sinko who helped establish the set up for the experiment, trained the monkeys, constructed gloves, and made the electrodes.

1.0 INTRODUCTION AND BACKGROUND

The primate hand has evolved to allow specialized interactions with our surroundings that define much of what makes us human. The movements in which we use our hands, the neural control of these behaviors, and our hands themselves are exceedingly complex. The primate hand is a system containing 27 bones, 18 joints, and 39 intrinsic and extrinsic muscles [1] with a potential for over 20 joint motions for hand shaping [2]. Movement of the fingers requires a coordinated interplay of both extrinsic and intrinsic muscles [3, 4, and 5]. Detailed analytical investigations into these movements have only recently begun. Fortunately, recent methods that detail hand movement and new analytical techniques for extracting these details from recorded neural activity allow us to gain initial insight into some of the principles used to generate these behaviors

Compelling arguments, based on a sparse fossil record, show that the human hand has evolved from an effector used primarily in arboreal locomotion to one used for tool manipulation. The length, strength and mobility of the thumb, the abduction of the fifth digit and the structure of the bones at the base of the fingers are thought to be factors that evolved to make it possible for hands to cup objects with enough strength to manufacture prehistoric stone tools [6, 7]. Our early hominid ancestors adapted the ability to throw stones and swing clubs at their adversaries. It was these actions that gave them an evolutionary advantage for millions of years

[8]. The manipulation of stones for throwing and sticks for clubbing made upright posture advantageous, later giving rise to habitual bipedalism in humans [9]. Our ancestors depended on binocular depth perception to shape the hand for object accommodation and accurate hand placement. The acquisition of these skills was correlated with a simultaneous evolution of the musculoskeletal and nervous systems which can be described by studying the structure and control of the hand.

Because of the limited fossil record, and its inability to detail neurophysiology, investigators have concentrated on living primate phylogeny [10, 6, 11, 12, 13, and 14]. Starting with tree shrews, prosimians and lemurs, proceeding through new world monkeys (marmoset, squirrel, capuchin and spider), to old world monkeys (macaque, baboon and colobus), all the way to gibbons, apes (orangutan, chimpanzee and gorilla) and culminating with humans, there is a clear progression of hand structure. Hollow claws become flattened nail with a concomitant enlargement of the fleshy glabrous finger pads with tactile sensory apparatus. The thumb becomes more mobile. This is clear, for example, in the differences between apes and humans "power grip" [6, 12 and 13]. Chimpanzee's (anatomically most similar hand to humans) utilize a 'hook grip' of four flexed fingers [11, 15] while humans use a 'finger-active palm squeeze' that relies on activation of powerful thumb musculature. The human grip allows for the thumb to wrap around and squeeze an object to the palm. Therefore, humans are able to stabilize tools, which are used as an extension of the hand and forearm [16].

Comparative anatomy of living primates shows that cortical development is correlated with the visual, tactile and motor behaviors associated with complex hand movement [17].

Specifically, the “least automatic” dexterous movements of the hand during exploration and manipulation of objects are thought to signify essential human behavior at the pinnacle of evolution. Historically, the importance of neural control as a limitation to the dexterity of the hand has been emphasized.

The function of the corticospinal projections for dexterous behavior comes mostly from studies in which the medullary pyramids were sectioned in macaques [18, 19, and 20]. The animals tolerate the lesion well. “An hour or so after completion of the operation the animal can usually sit up; after 24 hours it begins to take food, and by the end of a week it is fully recovered except for the specific effects of the lesion” [18]. In general, the recovered animals’ gross movements appear normal. They climb and swing with minimal deficits. With unilateral sections there is a flaccid paralysis on the contralateral side with a deficit in prehension. The ability to move the fingers independently and oppose the thumb is lost. Instead, grasping entails a cupping motion seen in infants or phylogenetically lower primates - suggesting a control reversion. These deficits were permanent, with the conclusion that the corticospinal tract is essential for dexterous control of the hand.

Human grasping has a characteristic ontogenetic development [21]. Before grasping can take place, reaching must be mastered. This begins in four to five month-old infants, but regulated grasping takes another four to five months. Early grasping is driven primarily by tactile and proprioceptive reflexes with crude closing of all the fingers. This reflex becomes less prominent by the tenth month. This coincides with increased independent finger movement. As humans progress through adulthood their grasp changes from crude closing to a highly adaptable

end effector. These actions have been examined by investigations focusing on both complex and simplified grasping movements.

In the early 90's, Schieber began a series of studies to examine the role of motor cortical cells in the control of individual finger movements [22, 23]. In his investigations a manipulandum was built to isolate each finger, and animals were trained to flex or extend a single specific finger when cued. It was found, using sensitive strain gauges that the non-instructed fingers moved as well [11, 24]. Thus demonstrating the monkeys' limited ability to make individuated finger movements.

When motor cortical units were recorded during individual finger movements [25], it was found that most were modulated with multiple fingers. The neurons active with different finger movements overlapped extensively in their cortical location. It was concluded that a widespread population of neurons were active for a particular movement [26, 27]. It has been known for years that motor cortical neurons projecting to different muscles are intermingled on the cortical surface [17], that a given cortical neuron projects to multiple muscles [28] and a given muscle is innervated by neurons spread over a large portion of motor cortex. This organization and the need to activate multiple muscles for individuated finger movements, means that neuronal populations direct finger movements through widespread networks [29].

The lack of completely independent finger movements is also true of humans. Even in skilled movements such as typing and piano playing, multiple fingers move together [30, 31, 32]. It was these studies that first described the hand in terms of "degrees of freedom" (DoFs) in

which specific rotations around each joint were specified. Digits two through four each have four DoFs– rotation around the proximal (PIP) and distal interphalangeal (DIP), and the metacarpophalangeal (MP) joints as well as ab-adduction at the MP. The thumb has four DoFs (flexion-extension at the IP, MP and carpometacarpal (CMC) joints, ab-adduction CMC joint [33]. Ascribing a precise number of DOFs to the hand is difficult, as many bones in the palm of the hand are mobile. This mobility aids the hand in cupping and opposition. However, the hand is generally considered to have "more than 20 degrees" of freedom.

Napier [6] divided hand movements into prehensile and non-prehensile categories. Prehension is the most common type of hand movement [29] and is only found in mammals. This evolution was driven by arboreal locomotion, infants clinging to their parents, and the necessity to reach for food [34]. The reach-to-grasp motion is characterized by an open hand early in the reach that continuously changes shape to approximate the grasped object. The coordination of the finger movements during grasp has been the focus of many investigations.

Studies have shown that static grasp posture can be described using a small number of postural synergies [35, 36, 37]. These synergies can be defined as a spatial configuration or "primitives" of the hand shape that is common across various tasks. Using principal component analysis, only three components were needed to describe approximately 90% of the variance, with the first two components explaining approximately 84% [35]. This work focused on the end, or static phase, of grasping while the object was in contact with the hand. The authors concluded that there were a few general patterns of coordination for coarse control of hand shape. More sophisticated control of individual fingers was thought to be represented in the

higher-order components which were not combined in any regular pattern [37]. The presence of postural synergies describing hand movement throughout the reach was not investigated, yet the results suggest a common strategy exists.

More recent work has shown that modulation of hand shape that begins prior to movement and continues to object contact can be modeled with a few postures [1]. These findings expand and confirm the results that hand shape evolves gradually throughout movement [36, 38, 39, 40, and 41]. More importantly, this work illustrates that the entire reach-to-grasp movement can be described using a small number of variables.

These correlation functions may represent a simplifying strategy utilized by the motor cortex. The controller may direct the hand with a reduced the number of descriptors and thereby reduce the complexity of the control problem [35, 42, 43].

Monkeys have similar reach characteristics as humans [41, 44, and 45]. They preshape their hands during reaching and scale their aperture for object size in an object- and accuracy-specific manner. The previously mentioned psychophysics studies used human subjects. Examining similar patterns of coordination Mason et al. [46] also carried out these experiments in monkeys. Monkeys reached to grasp and squeeze sixteen different regular solids to exert a specified force on the object in the absence of vision. Singular value decomposition applied to the marker data showed that the first component accounted for more than 90% of the variance and the second explained about 5%. This shows that the fingers moved in a stereotypical manner across many objects. Furthermore, there is no relationship between the eigenvectors and the

squeeze-force applied to the objects. The authors concluded that hand shape was independent of the applied force. These results, in the absence of vision, were interpreted as evidence that hand shaping takes place as feed-forward operation.

A more recent study, [47] blindfolded human subjects and had them perform a haptic exploration task of 50 different objects. The authors compared the patterns of coordination found during haptic exploration with a grasping task under visual guidance. As expected the haptic behavior required more eigenvectors (7) to explain 90% of the variance than the earlier studies. Nine eigenvectors were consistent across subjects. As with the other studies, the first component was dominated by the MCP joints which were used to open and close the hand. The third and fourth components were dominated by thumb movement. This may be reflective of the wider range of hand postures required for this task. The components derived from the search task could be used to reconstruct the hand shapes of the reach-to-grasp task as well. In constructing a particular movement, only a few components were needed. This suggests that there were object-specific sub-spaces. This only becomes evident when the task space is rich enough to generate many coordination patterns. This is also consistent with earlier studies suggesting that there was a dichotomy of control where there were basic patterns for crude control combined with higher-order patterns for more complex control.

In order to better understand the constraints and principles of organization used for controlling the hand, we have carried out a series of studies describing both the detailed kinematics of the hand and of motor cortical activity as monkeys reach and grasp a variety of objects. Monkeys were trained to make these movements in a consistent way as objects were

presented in different locations and orientations with the objective of sampling a wide variety of hand shapes and orientations. The complex nature of this study will provide insight into how individual motor cortical cells modulate as a function of natural movements of the wrist, hand and fingers.

1.1 PROSTHETICS AND CLINICAL SIGNIFICANCE

Motor restorative prosthetics is an active area of research intended to assist patients with limited or no ability to move. Two broad categories of patients can be assisted by these devices. The first group of patients are those with limited interactive capacity (i.e. brain stem strokes and late stages of amyotrophic lateral sclerosis). These patients may benefit from rudimentary brain computer interfaces [48, 49, 50, and 51] and categorical based neural prosthetics [52]. The second group includes those patients with communicative capacity, but decreased volitional movements. For example, patients with spinal cord injury (SCI) (between 200 – 400,000) and patients with amputations [53].

Neurophysiology research has provided the fundamentals for motor restorative prosthetics research for more than 30 years [54–64]. Early researchers showed that arm movements can be predicted from populations of motor cortical cells [55, 61]. Researchers have since used spiking activity from populations of motor cortical cells to control prosthetic devices [65-71]. Compared to the natural arm, current motor restorative devices have a limited number of simultaneously controlled DoFs. The current work provides a set of basic findings that can

develop into an extraction algorithm for control of a complex motor restorative system that directs wrist and hand movements from populations of motor cortical cells.

2.0 METHODS

This chapter provides an overview of the behavioral setup (2.1), kinematic data collection (2.2), joint angle calculations (2.3), surgical procedure (2.4), neural recordings (2.5) and experimental details (2.6).

2.1 BEHAVIORAL SETUP

This experimental setup was designed to study reach-to-grasp movements, with an emphasis on the hand and wrist degrees-of-freedom (Figure 1).

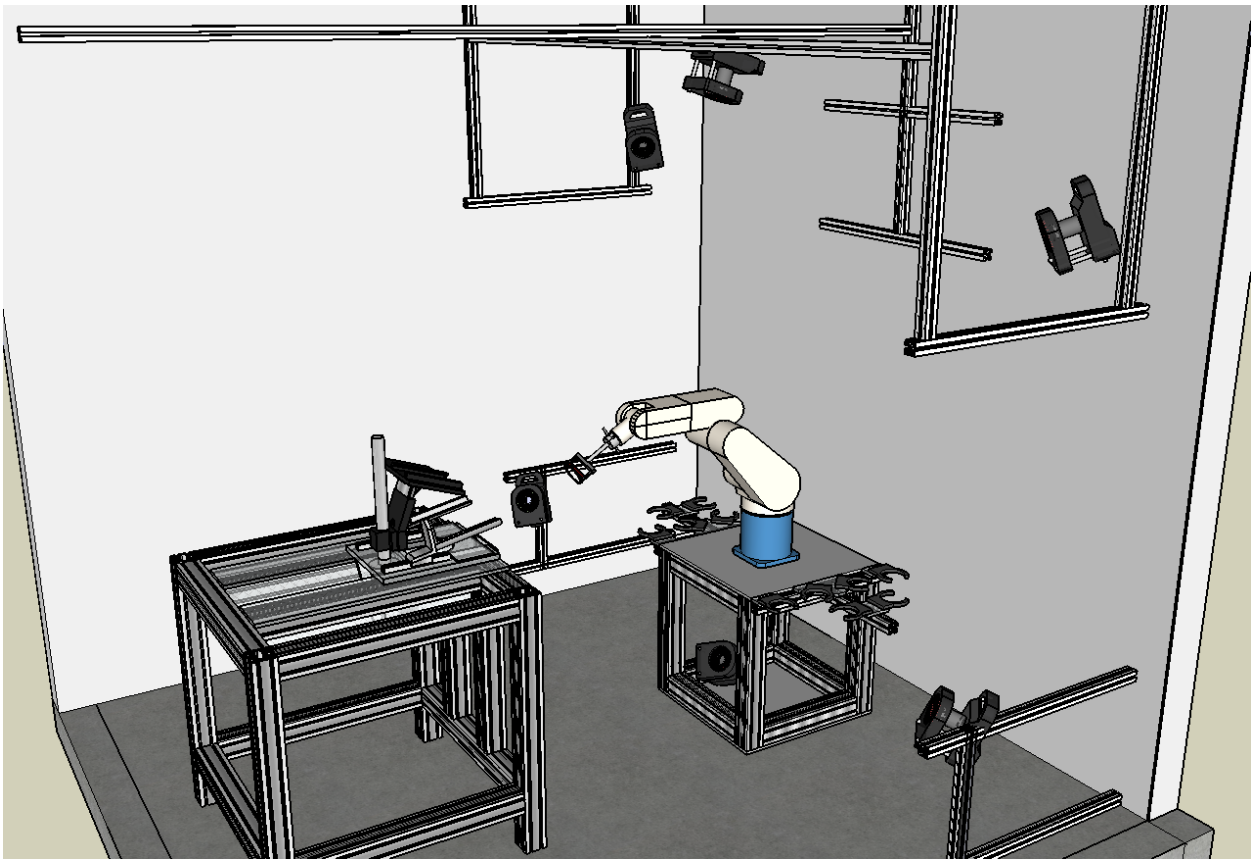

Figure 1. Representation of the behavioral setup.

The blue and white robotic arm was used to present objects. The restraint chair is shown in black on a frame separate from the robot. The black boxes mounted to the walls and ceiling represent cameras around the room.

A monkey was placed into a restraint chair in front of a Denso industrial robotic arm. A custom-made glove with reflective markers was secured to the monkey's hand. The hand markers were tracked using a Vicon® passive motion tracking system. There were 12 cameras (only six shown in Figure 1) situated in a half circle in front of the monkey, a configuration optimized to track positions from all sides of the hand. A camera reconfiguration occurred depending if the left or right hand was being tracked. The cameras had infra-red light emitting diodes around the perimeter of the lens. The light emitted from each camera hit a retro-reflective

marker situated on the monkey's hand. Using the 2-D gray scale image of a marker tracked by at least two cameras, the Vicon system reconstructed the 3-D position.

Each glove that the experimenter placed on the monkey's hand was custom-made for each monkey from a template tracing. The glove was made of a stretch black lycra which ensured a tight fit and reflective markers were sewn on. The area of the glove with the majority of the markers (19 out of 23) was about 10 cm long by 5 cm wide.

Figure 2. Motion tracking glove.

Picture of a motion tracking glove made for the right hand of monkey V. The lycra material was sewn together with flexible thread. Reflective markers were located at all the inter-joint segments of the fingers and thumb. Three markers formed a plane on the palm, and four markers made a forearm plane. There were twenty three 3mm markers on each glove.

The Denso robot used in this experiment had six degrees-of-freedom, four air solenoids, and ten electrical connections that passed from the base to the end-effector. The robot was able

to present objects at different x, y, and z positions with varying orientations. The robot effector was fitted with an ATI QC-11 master tool changer with a ten contact electrical module for interfacing with the tool (Figure 3). Each tool was attached to an ATI QC-11 slave tool changer (Figure 3). The robot picked up many different tools by pneumatically driving a piston located in the master.

Figure 3. Tool changing mechanism for object presentations.

The left panel shows the master portion of the tool changer. The white rectangle to the upper left houses ten electrical connections. The silver component in the middle of the master is the pneumatic piston. The right panel shows the slave portion of the tool changer. Each object was mounted to a single slave.

A computer with custom software controlled the Denso robot arm in real-time, ran the state based behavioral program, and sent behavioral cues to the monkey through a Digital I/O card.

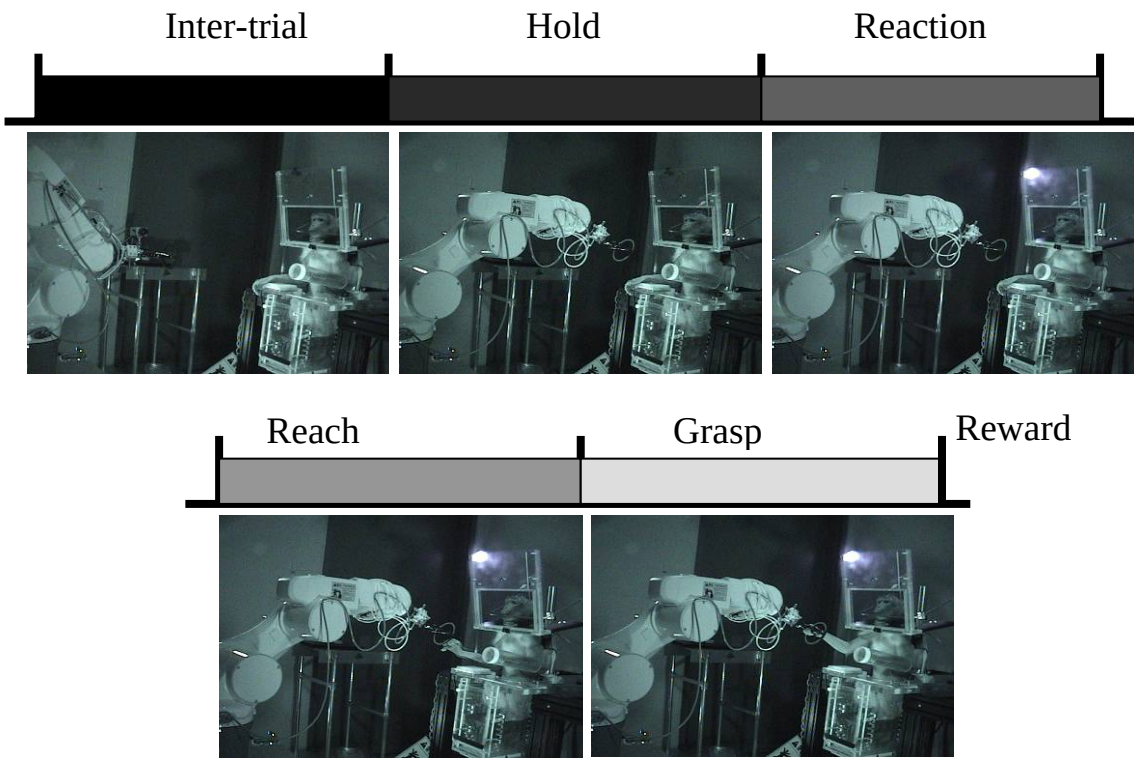

Figure 4. Progression of a reach-to-grasp trial.

Pictorial representation of a reach-to-grasp trial.

A trial started with a short inter-trial interval from the trial before (Figure 4). During this time the lights in the room were off, and the monkey placed its hand on a start pad situated in a rest position. With the queue of the hand on the start pad the robot presented the tool at a specified target position. If the hand lifted off the start button before the Hold A time (time that the monkey had hand on start pad) expired, the trial was a failure. If the hand stayed on the start pad for the entire Hold A period (between 400-1000ms) the lights in the room turned on. The Lights On cue was the go signal for the monkey. At the start of go was the first time the monkey visualized the target location and orientation. After the lights turned on there was a short reaction time (250ms) for the monkey to lift the hand off the start pad. If the reaction time was exceeded

the trial was a failure. However, if the monkey lifted its hand from the start pad before the reaction time expired, it had 750 ms to reach the object. If the monkey did not move fast enough the trial was a failure. The Hold B portion of the trial started when enough pressure was placed on all sensors to pass a predetermined force threshold. Hold B continued for a random time between 400-700ms. If the pressure applied to the sensors exceeded threshold for the entire Hold B period, the monkey received a liquid reward. If an unsuccessful trial occurred at any portion of the above sequence, the robot moved back to the home position. If the trial was successful the presentation was removed from a selection matrix; if unsuccessful the presentation was maintained.

Force Sensing Resistors (FSR's) were placed on the objects to detect grasping pressure. A FSR is a simple variable resistor that changes resistance as a function of pressure. Change in resistance was recorded as a change in voltage from zero to five volts using an analog input card. Zero volts indicated an applied pressure above the sensors maximum detection, and five volts indicated no pressure. The FSR signal was filtered using a 6Hz lowpass butterworth filter to remove high frequency noise produced from the robot motors. The FSR's were placed on multiple sides of the objects in order to maintain consistent grasps across days, and remove the monkey's ability to get rewarded for non-grasping behavior. For example, the small handle (Figure 20) had FSR's on two sides of the cylinder so the monkey had to squeeze the handle for a reward. Both force sensors had to register a voltage reading below a set threshold for the monkey to be rewarded.

The randomized Trial Selection Matrix included all target positions and orientations for a session (Table 2). A group of target positions for an object was called a block. A Set referred to a single presentation of all objects. The Set Matrix was equivalent to multiplying a set x 5, so we could sample each object presentation five times in a session. This matrix contained all the presentations for a single session, but in a non-randomized order. The matrix was randomized with a number of permutations. The number was generated from Matlab using the computer start time as a seed. This ensured that the monkey could not learn the object presentation order over days. During the course of the task if a trial was successful the target and presentations were removed from the Trial Selection Matrix; if unsuccessful it was maintained. This technique allowed for object randomization throughout a session and repetition of only the unsuccessful object orientations.

2.2 KINEMATIC DATA COLLECTION

Kinematic data was collected from the hand and wrist. The three wrist DoFs and 20 hand DoFs were tracked using a Vicon Mx® reflective motion tracking system. The small size of the hand (10cm by 5cm), and fast movements with the hand in many orientations, increased the difficulty of acquiring kinematic data. One limitation with passive motion tracking systems is the ability to uniquely identify each marker without each marker having a unique identity (i.e. differing light emitting frequencies in wired motion-tracking systems). The passive systems are plagued with non-contiguous segments of data.

Differentiating one marker from another and tracking non-contiguous markers has traditionally been difficult when using reflective based motion-tracking systems. When a marker goes out of view, the trajectory becomes broken, thus the marker cannot be labeled based on the prior frame, and the data is lost. In order to overcome this problem, we partnered with Vicon to develop a modeling system that utilized information about hand kinematics. Software of a kinematic model that mimicked the anatomy of the hand was created. This first estimation was a general model that described the relationship between markers, joints and segments (bony structures between joints). The general model was only specific for our marker placement, not unique per monkey, and could be scaled per subject. This anatomical description of markers was called an uncalibrated model. A calibration procedure was necessary to label 3-D data in real-time.

The calibration procedure started by collecting a ‘range of motion data file’ (2,000-3,000 frames) while the monkey grasped an object in a set number of orientations. After reconstructing the 3-D marker data and ensuring the data was contiguous, the experimenter applied labels to a single frame of the 3-D data. The user would visually progress the captured movements, making sure to correct any labeling errors. After a marker correction, the model was adjusted using proprietary algorithms to best fit the motion over the entire file. During this process, the centers of joint rotation, and model marker positions were adjusted. Upon completion of the calibration procedure, an updated model was created with accurate parameters corresponding to kinematics of the monkey hand.

Due to difficulty tracking small subjects with fast movements, these procedures were not enough to ensure accurate joint angle reconstruction. In a complete session the hand was continuously tracked over an hour. It was not realistic that the accuracy of the calibrated model would be the same just after calibration as it would be 45 minutes into the session. This was accentuated by the fact that the monkey glove worked more distally throughout the session. In light of this, we created a more accurate joint angle calculation procedure that allowed for slight changes to occur without decreasing joint angle accuracy (Section 2.3.3). To ensure accurate joint reconstruction a separate procedure was created to correct missing and mislabeled markers (Section 2.3.1).

2.3 ESTIMATING JOINT ANGLES

A common strategy for joint angle calculations is to estimate the angle from markers placed on segments, i.e. on the bony portion connecting two joints [72]. Using this method the markers are translated with an offset equal to the distance from the bone center. This measurement is prone to error due to difficulty in assessing boney centers without the assistance of an X-ray. In this study we have adopted a technique to calculate joint angles from joint centers that is less prone to marker-offset error. This algorithm consisted of correctly labeling marker data (2.3.1), joint center estimations (2.3.2), and joint angle calculations (2.3.3).

2.3.1 Model Labeling

After the kinematic model was calibrated (detailed in Section 2.2) the majority of markers were labeled correctly. However, during small portions of the task the model made labeling errors. Without correct model labeling, joint center estimates and joint angles are not accurate.

We produced many algorithms to automatically correct mislabeled markers. However, all algorithms failed at unpredictable points in the data set. Each algorithm relied on inflexible cutoffs to judge data quality. A high cutoff produced too many false negatives, and a low cutoff gave too many false positives. These automated correction algorithms did not produce reliable results with simple cutoff adjustments. Because of these difficulties, an algorithm was created to allow the experimenter to quickly visualize and manually edit the marker data (Grasp Viewer).

Kinematic data labeling was more reliable using a visual based marker label correction system compared to the automated algorithms. The 3-D marker data from the Vicon system was loaded into the Grasp Viewer. According to the Vicon system this data was supposed to be labeled correctly, however this was rarely the case. To ensure correct data labeling the viewer started at the beginning of the data set (Figure 5), and would play to the end. The progression could be stopped by the user if a model appeared mislabeled (Figure 6). The labeling was corrected by a mouse click on the markers through an appropriate labeling sequence defined by the marker set. If a particular model error continued to occur multiple times throughout a single session the algorithm would automatically apply previous corrections, and provide these as options to the user. This time intensive model correction method took advantage of the experimenter's knowledge of the hand model and guaranteed accurate labeling.

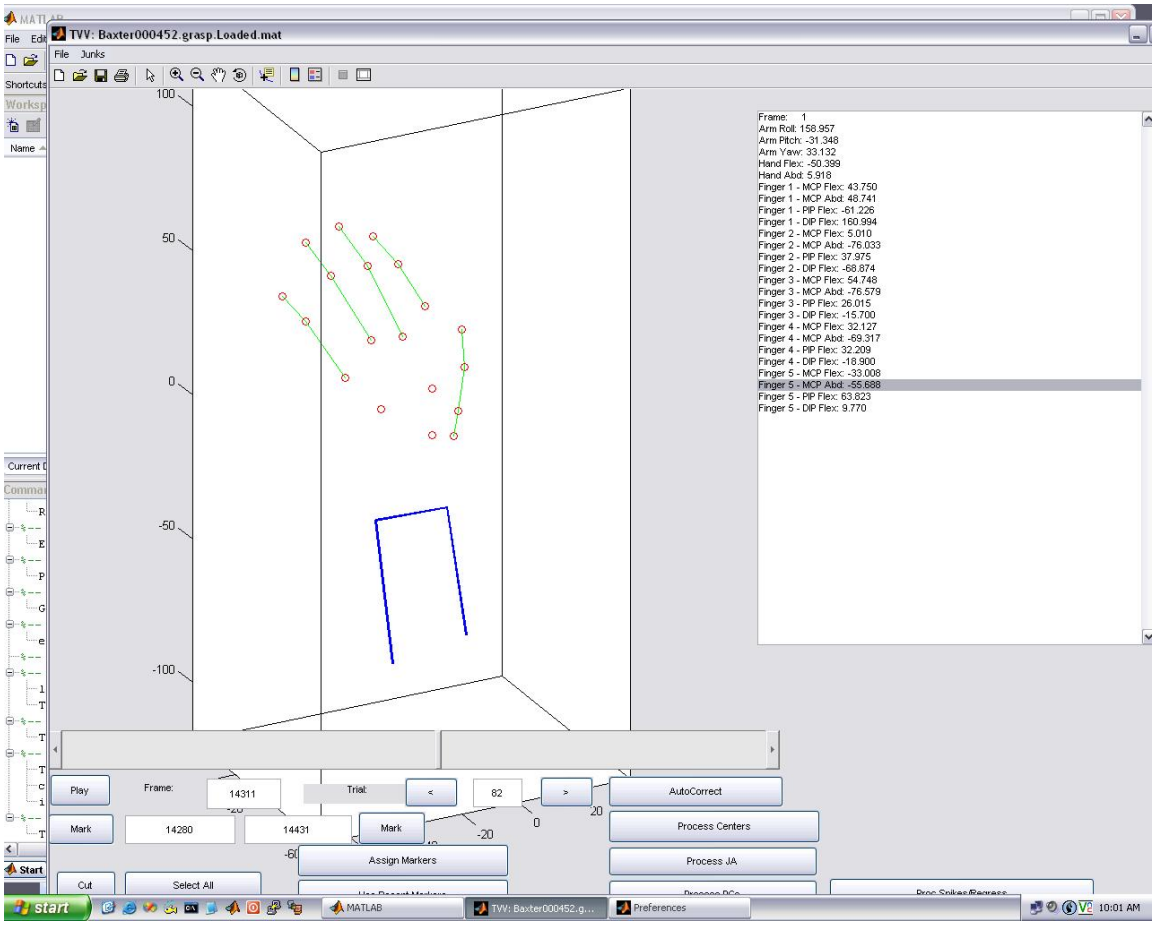

Figure 5. Marker data displayed in the grasp viewer.

This graphic shows a single frame of the left hand centered on a marker placed over the first metacarpal with the hand in a slightly pronated position. This orientation gave an optimal viewing angle to detect the most frequent labeling errors.

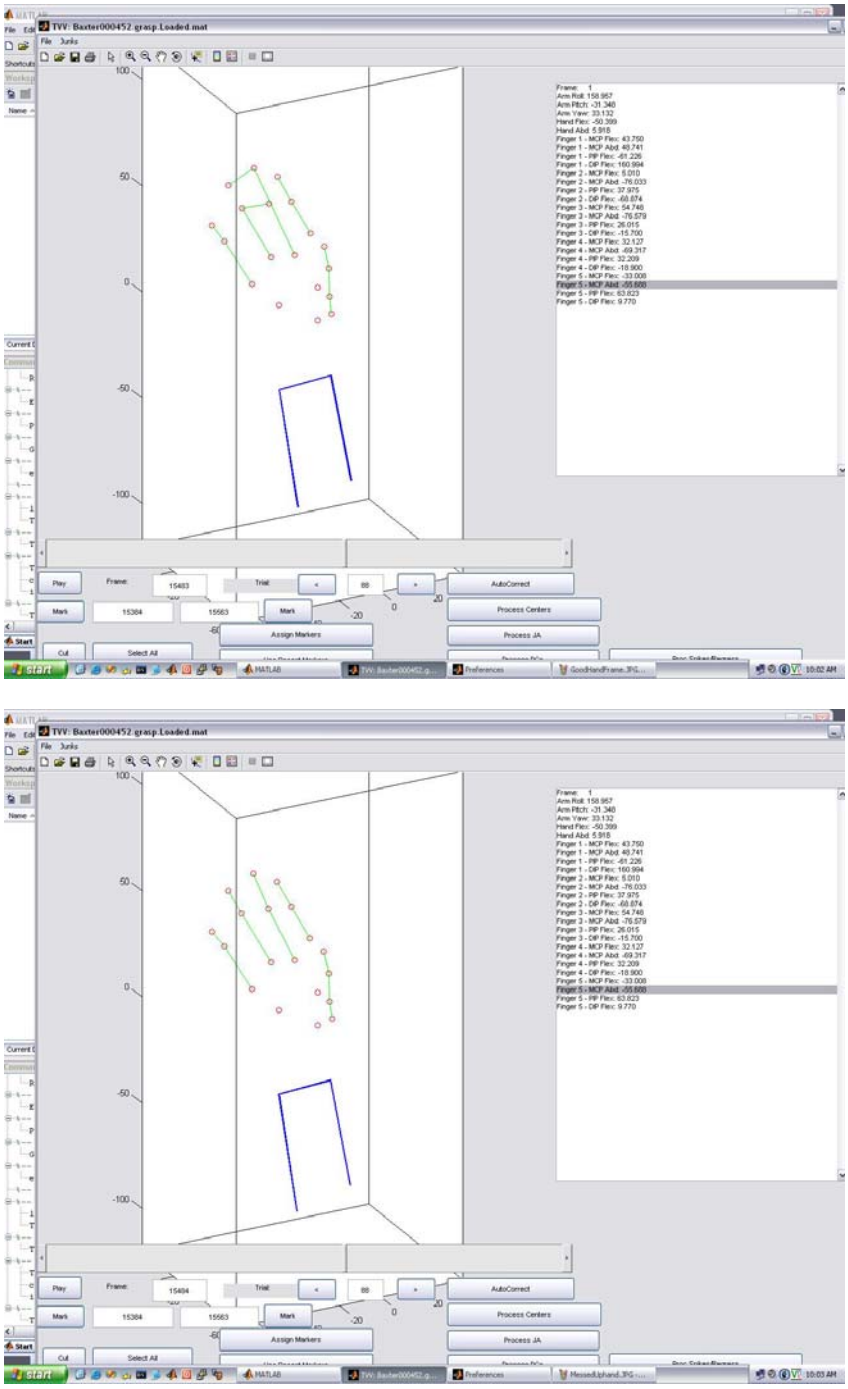

Figure 6. Marker data correction in Grasp Viewer.

The top panel displays a single frame detected as being mislabeled. The mislabeling error in this case is with the second interphalangeal marker and the third distal marker. This error creates a scenario that we referred to as a crossed finger. The lower panel shows the same frame as the top panel after correction of the labeling error using the marker-based clicking system.

2.3.2 Calculating Joint Angles

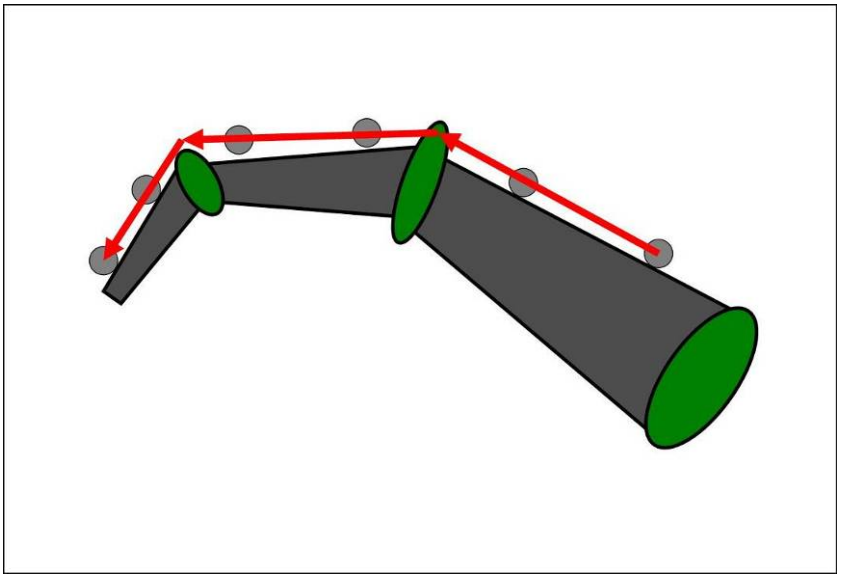

Figure 7. Segment marker placement.

The graphic represents ideal placement of markers for a single finger. There are two markers per segment. In this illustration the green ellipses represent the joints, the dark gray between the joints represents the segments, the small gray circles represent the markers, and the red lines indicate the vectors used to calculate joint angles.

Calculating joint angles is a straight-forward process, and can be done with a simple equation (Equation 1) if there are two markers per segment (Figure 7).

$$\Theta = \cos^{-1}\left(A \cdot B\right) \tag{1}$$

Equation 1 is the fundamental procedure we applied to our joint angle calculations, but many processing steps took place before we could calculate the correct **A** and **B** vectors. In the previous example (Figure 7) **A** and **B** are explicitly defined by the marker set because there are two markers per segment. However, in our experiment the vectors **A** and **B** cannot be directly

defined from markers. The monkey's finger segments were not large enough to accommodate more than one 3mm marker per segment. To overcome this obstacle a review of current joint angle calculation techniques was necessary, the results of which are detailed below.

There have been several methods used to calculate joint angles with two markers per segment [72]. One intuitive technique (Figure 7) tends to generate a poor estimate of absolute angle. This is a result of assuming the modeled segments are rectangular. The proximal half of the segment is larger than the distal. When the angle is calculated directly from the marker set, even with two markers per segment, there is an accumulating error correlated with the change in radius of the proximal to distal portions (Figure 8). Researchers have accounted for the change in segment radius by translating the calculations of vectors **A** and **B** (Figure 8) with a continuous offset [73].

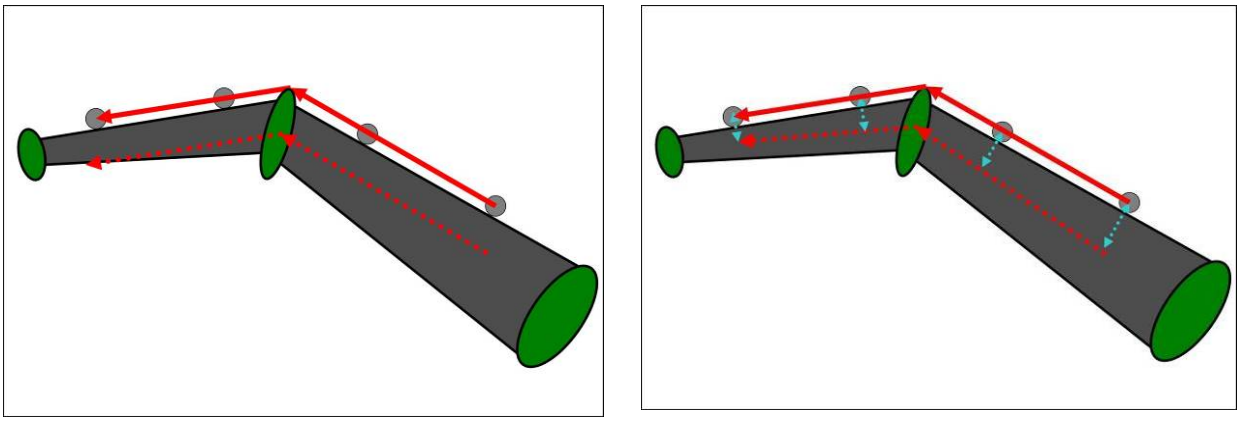

Figure 8. Joint angle calculations - two markers per segment.

The left panel illustrates how error propagates down the segment if the joint angle is calculated directly from the markers with no offset. The solid lines are vectors used directly from the marker set. The dotted lines show how this relates to joint centers. The right panel displays how this error can be corrected by applying an offset based on the changing segment radius.

In our marker set the distance between joints was so small that only one marker could be placed between each joint. If the markers are used to calculate vectors **A** and **B** in a one marker per segment situation, the joint angle calculation error is obvious (Figure 9). The calculated angles would have a complex relationship between multiple joints, with no clear correlation to joint angles.

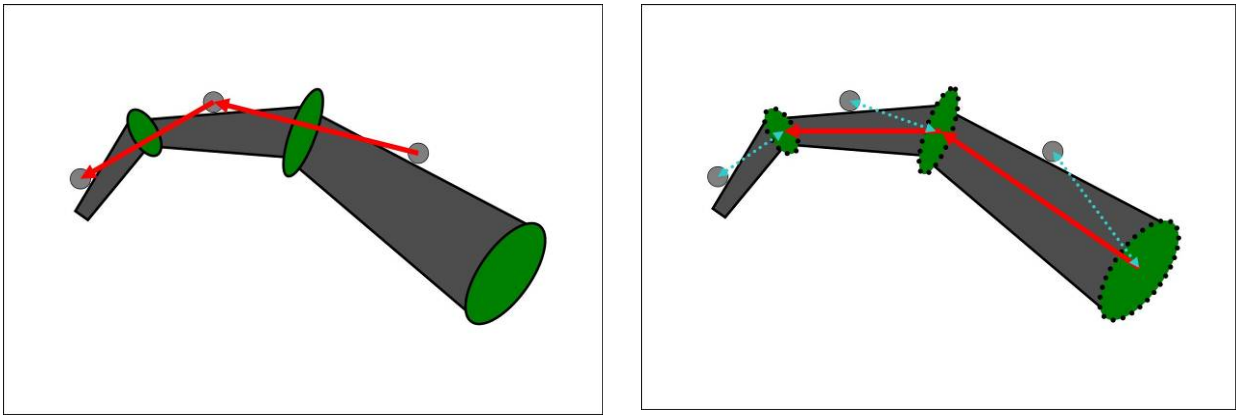

Figure 9. Joint angle calculations - one marker per segment.

The left panel shows what happens if vectors A and B are calculated directly from a single marker per segment data set. The right panel illustrates how we achieved accurate joint angle calculations. The blue dotted line shows the relationship between the center of the marker and the joint center. After this relationship is established the vectors A and B are calculated directly from joint centers, not markers.

To establish the proper **A** and **B** vectors, we used marker movement to estimate joint centers (discussed further in section 2.3.3). We used Equation 1 for joint angle estimations after vectors **A** and **B** were calculated from joint centers. This angle was not dependent on changes in

the radius of the segment, low frequency movement of the markers relative to the segment, and did not necessitate multiple markers per segment.

2.3.3 Joint Center Estimations

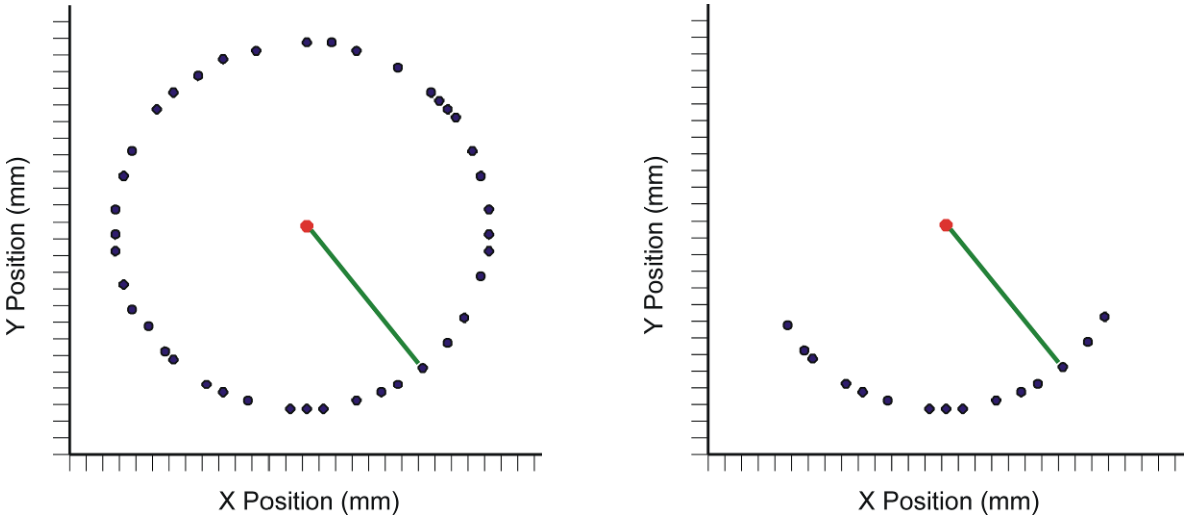

Figure 10. Simplified joint center estimation.

Both the left and right panels show examples of estimating a center of rotation based on the movement of a single marker. The left panel shows the data acquired from the movement of a point if 360 degrees of rotation occurred around a single axis. The right panel illustrates a more complicated problem of estimating a center when the data acquired is from a small portion of the arc. The right panel is a more accurate interpretation of our data set.

An algorithm that recursively estimated joint centers based on the most recent 5,000 frames of movement data was developed. The underlying principle behind this algorithm is similar to that of a two dimensional pendulum, where the only data is that of the pendulum endpoint and the desired variable is the attachment point of the pendulum (or the center). In the simplest case the pendulum swings 360 degrees around a circle. The data points could be averaged to produce a

fair estimation of the center of rotation (Figure 10). This basic example can be expanded to a pendulum that only moves through a small arc. If each data point of the pendulum is plotted, the arc forms only a portion of a circle. No simple mechanism exists to determine this center of rotation (Figure 10). If this example is expanded from two dimensions to three dimensions, the movement of the marker no longer forms a simple arc but moves over the surface of a sphere (Figure 11). In this example a unique position in 3-D exists such that the distance from the joint center and the marker are constant for all data points. The method we use to find this unique three-dimensional position was to minimize the variance of the radius estimation in a sliding window (5,000 frames). The least squared error approach was performed on marker data re-sampled to an even distribution of points on a sphere that covered the full range of original data (Figure 11). This re-sampling minimized the effects of erroneous marker positions, and provided a stable platform for joint center estimation.

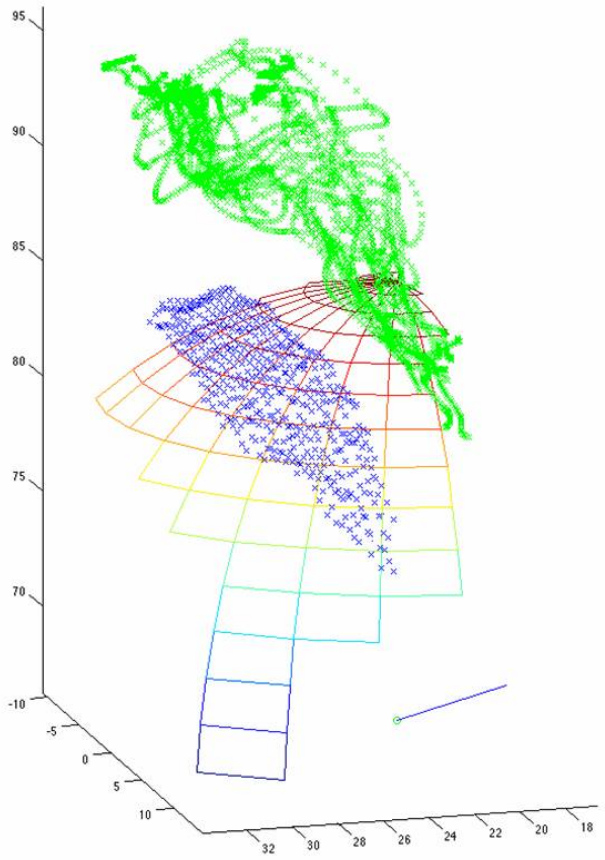

Figure 11. Re-sampled marker data used for joint center estimation.

The green data points illustrate actual marker locations in 3-D space. The blue x's indicate the positions of these data points after re-sampling. The sphere shows the data points projected onto the surface of a joint. The center of the sphere is the joint center used in joint angle calculations.

An additional feature of this technique is our ability to continually update the estimate of joint centers throughout the session. Glove movement changes the relationship between joint centers and marker positions. This causes a building error in joint angle calculations as a function of time. The iterative technique takes into account the possibility of marker shifts and adjusts joint center estimates to accurately fit data over the entire session.

2.4 SURGICAL PROCEDURE

The neural recording equipment was implanted in two phases. The first phase was the implantation of head holding posts and chamber surround. The chamber surround was a solid piece of titanium machined to the shape of an oval ring with ten feet extending from the base of ring (designed and manufactured by George Fraser). Each foot of the chamber surround had two countersunk screw holes giving a total of 20 skull fixation points (Figure 12). The feet were surgically form fitted to the skull, and the surround was a clamping ring for the recording chamber (Figure 12). The feet became overgrown by bone over many months after implantation. For stability purposes, the initial post and chamber surround implant surgery typically occurred early in the monkey-training phase.

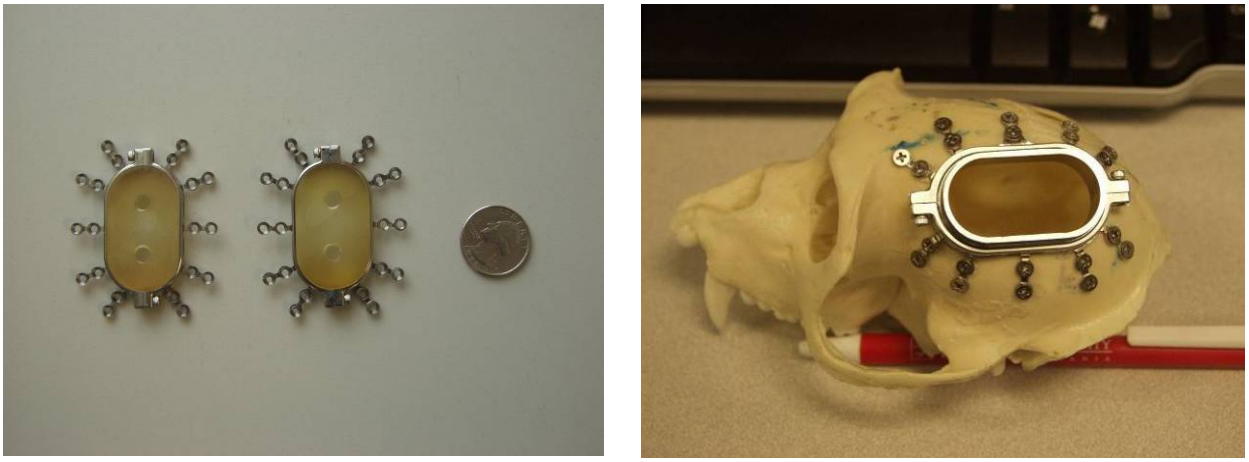

Figure 12. Chamber surround.

Left panel shows a picture of two chamber surrounds with plastic inserts (a quarter is shown to the right of the chamber surround for size reference). The right panel shows the chamber surround fixated to a plastic Rhesus skull. The ten stabilizing feet are anchored to the skull with stainless steel screws. On the chamber surround there are two protrusions on the long axis of the ellipse. These two protrusions contain set screws that clamp the surround circumferentially around the recording chamber.

Prior to surgery the monkey was given intra-muscular injections of Ketamine, Diazepam, and Cefazolin. The rhesus monkeys' in this experiment were typically 6-10kg males between five and eight years old. The head and dorsal portion of the neck were shaved, and the collar removed before entering the surgical suite. After endotracheal intubation the animal was connected to a ventilator and respirated with gas anesthetic (Isoflorane). The ventilator settings were adjusted to maintain a SpO_2 of 95%. An intravenous catheter was placed in the saphenous or popliteal veins to continuously administer saline and to act as access in case of an emergency. A rectal thermometer monitored the temperature throughout the procedure. A bear hugger was adjusted based on the temperature reading from the rectal probe. The animal was placed in a five-point stereotaxic frame mounted to a surgical table. A pulse-oximeter was placed on the lip,

finger or ear of the animal. The animal's head was prepared with betadine scrub and alcohol for sterility prior to incision. The surgical field was covered in sterile drapes. Sterile technique was used throughout the entire procedure.

The first portion of this procedure was to implant the head post base. Three separate small incisions were made. The first was midline just above the brow, the second and third were symmetrically located just medial and posterior to the auricles. The fascia and temporalis muscle were stripped from the skull. The posts were implanted using self-tapping titanium KLS-Martin bone screws. The skin was closed over the head post base with 4-0 prolene. The three bases formed a triangle with the apex toward the nose of the monkey. After completion of the head post base installation one large u-shaped incision was made to create an opening for two chamber surrounds. This u-shaped incision created a skin flap with intact posterior and posterior-lateral blood supply. The flap was later closed, covering the chamber surround. This minimized early infection, protected the bone screws, and provided time for the bone to grow over the feet and screws.

The fascia and temporalis muscles were separated from the skull and the feet of the chamber surrounds were manipulated to approximate the curvature of the skull. The exact positioning of the chamber surround (centered over hand area of motor cortex) was measured using stereotaxic coordinates calculated from an MRI. Each foot was secured to the skull with stainless-steel bone screws. A temporary insert was placed in the chamber surround (Figure 13).

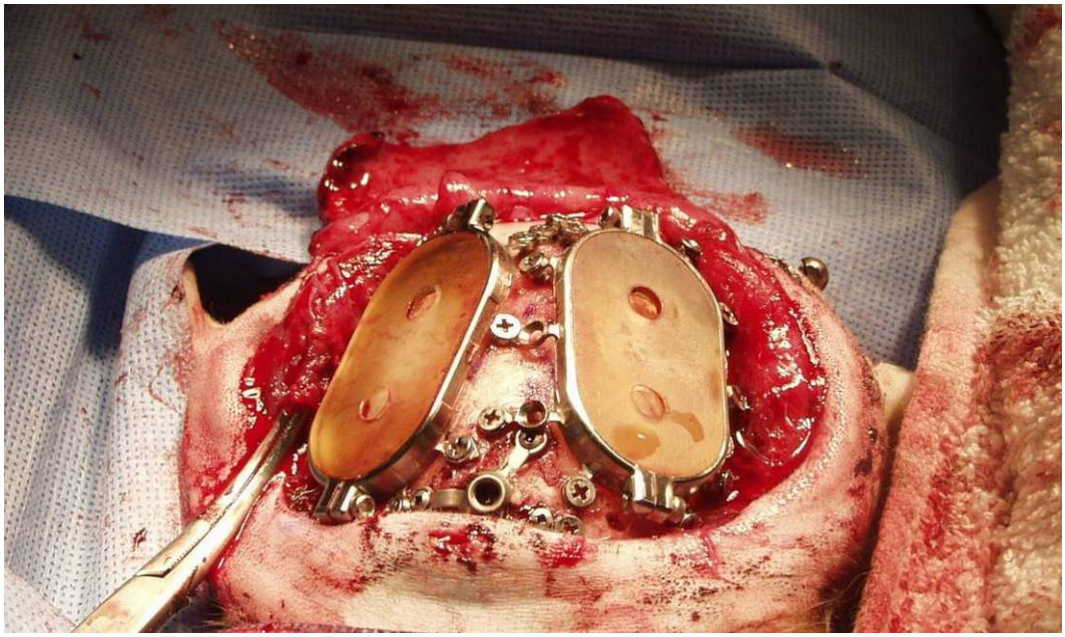

Figure 13. Implantation of chamber surrounds and head posts.

Picture from surgery of bilateral chamber surround and head post installation. Notice the proximity of the chamber surrounds to midline, and how the feet were adjusted to accommodate the posts of the contralateral hemisphere chamber surround. The photo was taken at the front of the animal. The posterior skin flap, seen reflected onto the blue drape, was composed of skin and fascia.

Before the incisions were closed, the temporary inserts were removed and silicon rubber was injected into the recording chamber space. After the silicon rubber set the mold was removed and the inserts were replaced. The silicon rubber served as a template for the curvature of the skull relative to the chamber surround. The mold was analyzed with a micromanipulator to determine the skull curvature. The relationship between the chamber surround and skull was incorporated into manufacturing of the recording chamber to minimize cerebrospinal fluid leakage.

In the second surgical procedure we implanted the recording chamber inside the surround. During this procedure the animal was prepared in the same manner as the first. A single incision was made over the chamber surround and the skin was reflected. A craniotomy was performed leaving a 2 mm ridge of bone around the inside of the chamber surround. An o-ring was placed on the bone ridge, and the recording chamber was placed on top of the o-ring. Pressure was applied to the recording chamber as the clamping screws were tightened. The combination of the custom profiled chamber, o-ring, and chamber surround provided a secure, water-tight fit to the skull. The procedure was completed with a 4.0 prolene purse string closure to secure the skin to the recording assembly. All procedures were performed in accordance with the guidelines set forth by the Institutional Animal Care and Use Committee of the University of Pittsburgh.

2.5 NEURAL DATA PROCESSING

2.5.1 Neural Recording

The electrodes used in these experiments were fabricated within our laboratory (Laurel K. Sinko and Ingrid Albrect). The raw materials were purchased from Thomas Recording and assembled throughout the course of the experiment. The electrodes were made of tungsten wire with glass insulation. The end of the electrode was beveled to a sharp tip to allow for dural penetration. The impedance of the electrodes was between 0.75 MΩ-1.5 MΩ. They were loaded into a five-channel Thomas Recording Mini-Matrix system. The Mini-Matrix had a motor per electrode with separate electrode guide tubes that protruded from the housing. The electrodes were bonded

to a 15 mm piece of silicon tubing that was clamped to a monofilament. The monofilament was wrapped around the motor head. A push button controller, or software system, located outside the recording room, controlled the motors. As the motors turned, the silicon tubing relaxed, producing a continuous predictable electrode driving force. After clamping the drive to the chamber, the electrodes were lowered through the dura at 4μm per second. After dural penetration, electrode advancement was halted and was left to stabilize for one hour. All recordings (Table 1) were made from the contra-lateral motor cortex of arm movement at depths between 3,000-12,000 microns. An illustration of electrode penetrations is shown in Figure 14.

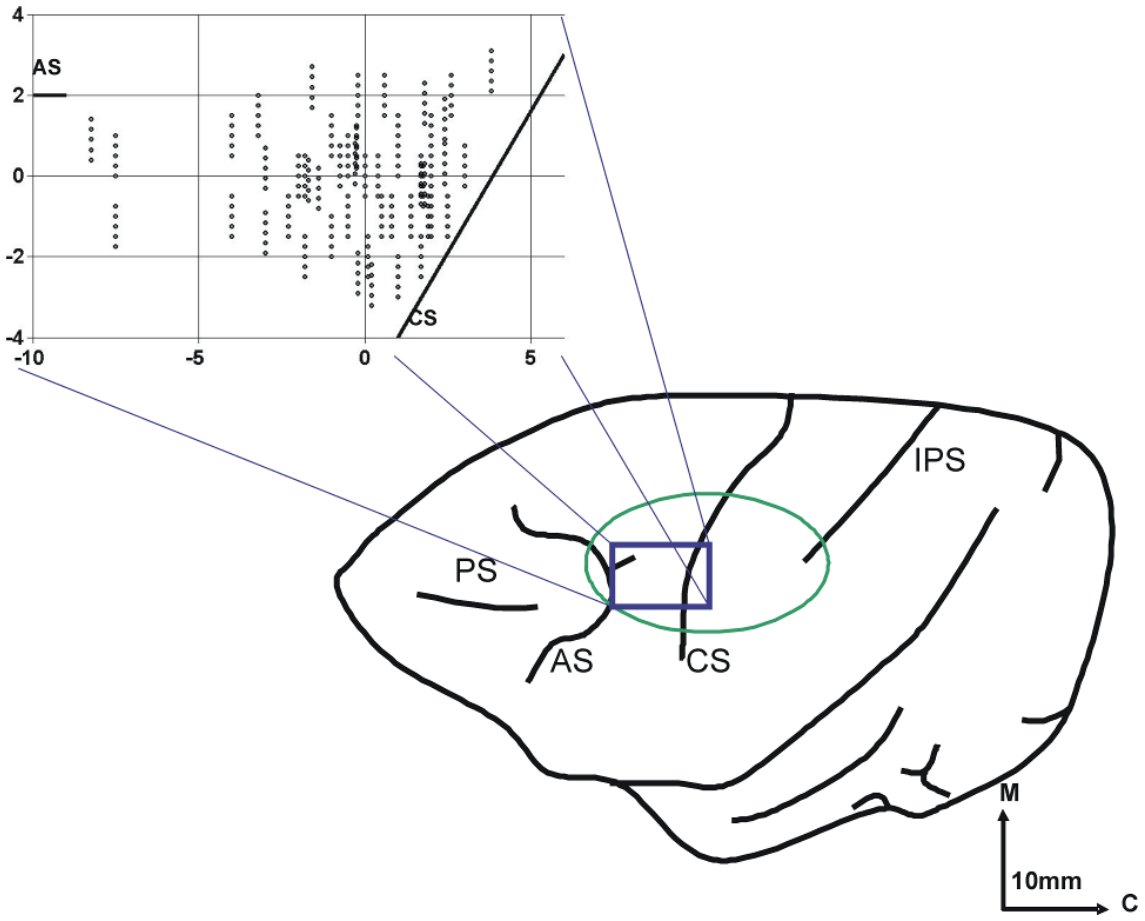

Figure 14. Penetration sites in relation to central sulcus.

Graphical representation of electrode penetration sites in relation to the central sulcus over 11 months of neural recording. Recording sites from three hemispheres and two monkeys have been projected onto the left

hemisphere. The green oval represents the recording chamber, and the blue rectangle shows the area of focused neural recording. The expanded Figure shows the electrode penetration sites, each dot represents a single electrode. PS = principal sulcus, AS = Arcuate sulcus, CS = Central Sulcus, IPS = intraparietal sulcus.

A 16-channel Tucker Davis Technologies (TDT) Pentusa recording system was used to digitize and display spike waveforms, timestamp neural data, and synchronize the kinematic data. The waveform data was sorted in real-time, and the waveform snippet data was stored for offline analysis. The timestamp data was buffered by a program written to interact with the behavioral paradigm. The TDT program received a “start buffer” message from the behavioral computer at the beginning of the Hold A (section 2.1) and a “stop buffer” message when a reward was given, or a trial failed. In the first hemisphere the retrieval movement data was not collected. This was later modified so the “stop buffer” message was sent when the Hold A start time occurred. Thus, the reach and retrieval data from the second two hemispheres were available for analysis.

Table 1. Sample of the files and number of cells recorded.

Table showing 89 different recording sessions that correlate with 438 cells, of which 327 were used in analysis. Only the cells that were both recorded for the entire session, and correlated with grasping kinematics are shown.

Filename	Number of Cells	Filename	Number of Cells
Baxter000445	4	Vinny000480	5
Baxter000447	8	Vinny000481	6
Baxter000450	4	Vinny000483	11
Baxter000452	7	Vinny000484	11
Baxter000453	8	Vinny000485	7
Baxter000455	6	Vinny000487	7
Baxter000456	6	Vinny000488	8
Baxter000458	4	Vinny000489	5
Baxter000465	4	Vinny000491	4
Baxter000467	7	Vinny000493	5
Baxter000474	3	Vinny000494	4
Baxter000475	3	Vinny000496	3
Baxter000477	4	Vinny000500	3
Baxter000478	4	Vinny000504	3
Baxter000481	5	Vinny000637	5
Baxter000501	3	Vinny000639	5
Vinny000413	1	Vinny000641	5
Vinny000417	1	Vinny000643	8
Vinny000418	1	Vinny000646	7
Vinny000420	1	Vinny000651	7
Vinny000422	1	Vinny000652	7
Vinny000425	1	Vinny000654	5
Vinny000430	2	Vinny000655	5
Vinny000433	4	Vinny000656	4
Vinny000439	6	Vinny000658	6
Vinny000442	5	Vinny000661	8
Vinny000447	7	Vinny000663	6
Vinny000449	5	Vinny000665	7
Vinny000453	2	Vinny000667	6
Vinny000456	7	Vinny000669	4
Vinny000457	9	Vinny000673	4
Vinny000459	6	Vinny000675	2
Vinny000460	6	Vinny000676	1
Vinny000462	1	Vinny000678	4
Vinny000465	4	Vinny000680	3
Vinny000466	5	Vinny000682	4
Vinny000468	8	Vinny000683	4
Vinny000471	5	Vinny000684	6
Vinny000472	6	Vinny000687	1
Vinny000474	7	Vinny000690	5
Vinny000475	6	Vinny000691	5
Vinny000477	6	Vinny000693	5
Vinny000479	6	Vinny000694	5
		Vinny000695	3

2.5.2 Fractional-interval firing rates

The analysis of motor cortical activity was approached with a rate code model. The classical approach to calculating firing rates is to first determine a bin size. The bin is a window of time over which the spiking activity will be considered one unit. As the bin size increases so does the probability of spiking activity to occur in that bin, the contrary is also true. There is an offset in time between motor cortical spiking activity and movement, i.e. lag. The average lag for all cells in this experiment was calculated by determining the max correlation between spiking and joint position for nine different time offsets (300, 250, 200, 150, 100, 50, -100, -200,-300). Those that had a peak correlation with a negative lag were considered to be sensory and were discarded in analysis. The best average time lag for all the cells recorded was 150ms. This average lag was applied to all cells early in data processing.

In the current experiment we analyzed firing rate activity as a function of dynamic processes. The dynamics of reach-to-grasp occur in 500ms, on average. For a pyramidal cell in the motor cortex, a high spiking rate is considered to be 100-150 Hz. Based on this, we would expect to record 50-75 spikes in a single reach-to-grasp for a cell with a high firing rate. When the bin size is decreased to 30ms, to better analyze the cells correlation to task epochs, the average expected rate decreases to three to four spikes per bin. In order to obtain a less sparse representation of firing rate per bin we utilized a fractional inter-spike interval (ISI) method to calculate firing rates.

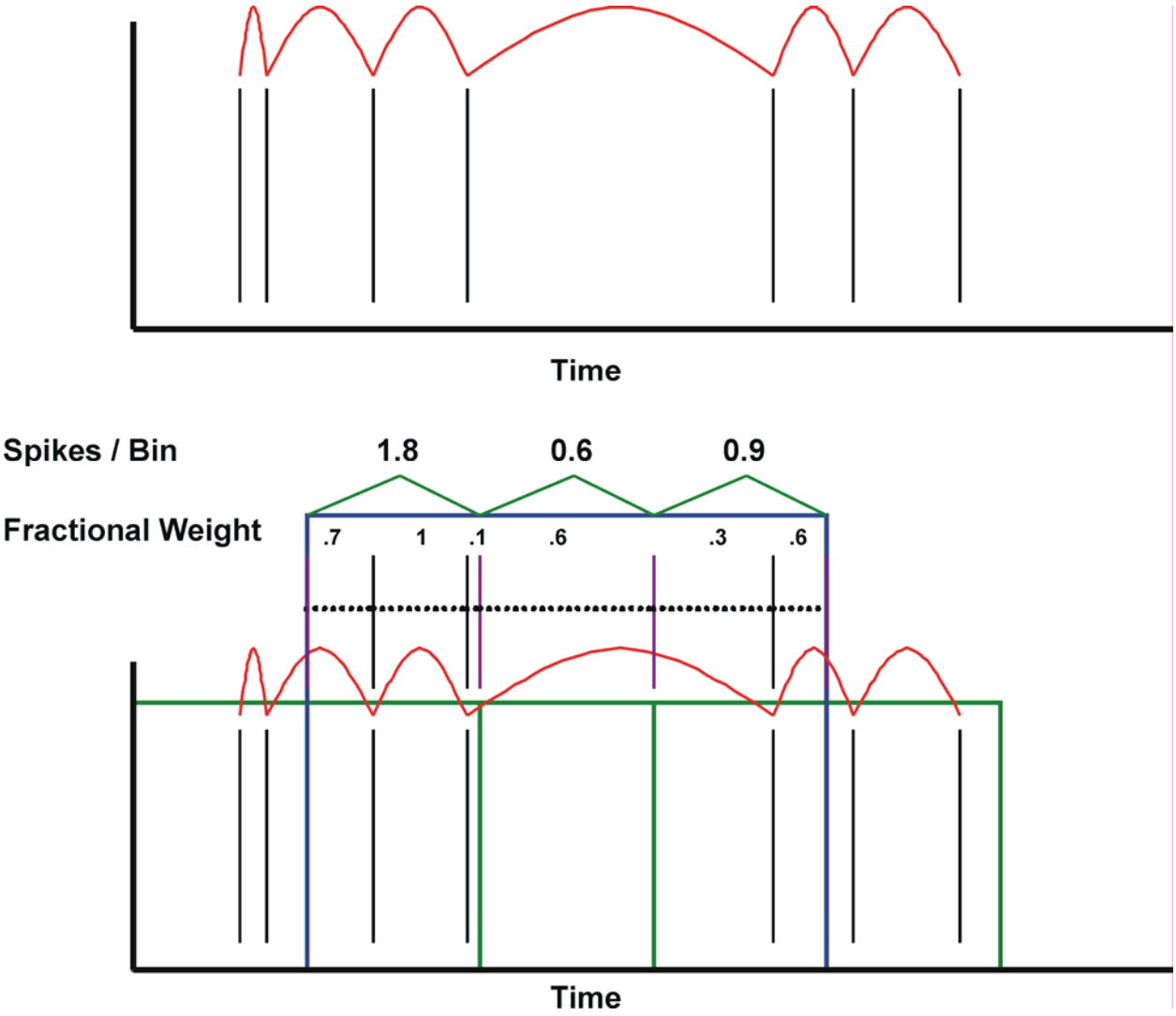

Figure 15. Fractional interval spike rates.

Top panel shows an example cell that spikes seven times during an epoch. The black vertical lines show the digital representation of an action potential. The red curves highlight the inter-spike interval (ISI). The lower panel shows how fractional intervals are used to calculate a firing rate. The green rectangles represent time bins. The blue portion of the spike train is used for example calculation of firing rate. The fraction of the ISI that occurs in a bin is labeled fractional weight. The fractional spikes occurring in a single bin are calculated by adding the fractional weights in that bin.

Figure 15 shows an illustration of fractional interval spike rates for an example cell over three bins. The inter-spike interval (ISI) is calculated. The fraction of ISI that occurs within a bin

is called a fractional weight. The number of spikes per bin is calculated by adding these fractional weights. The spikes per bin divided by the bin size gives the firing rate. If not otherwise specified, it is the fractional-interval rate calculated over 30ms bins used throughout all the analysis.

2.5.3 Kinematic and Neural data processing

Processing of the kinematic and neural data in preparation for neural predictions focused on kinematic alignment and binning data across many days. A session of reach-to-grasp data consisted of 23 DoFs of joint angle data, and at most 11 individual motor cortical cells. The collection of neural data continued over 11 months with a 5-channel Mini Matrix system. This recording method made it relatively easy to isolate individual motor neurons; however it was impossible to collect firing rates from large simultaneously recorded populations of cells.

The first step in the alignment procedure was to separate neural and kinematic data as a function of object presentation. This created 64 groups, one per unique object presentation. This decreased the overall variability in kinematic data per day, but combining data over many days still produced a large variability per joint (Figure 16). In this figure each tracing represents a single velocity trajectory for a joint, and zero (vertical green line) represents the start of the movement. The raw trajectories all have a different number of samples.

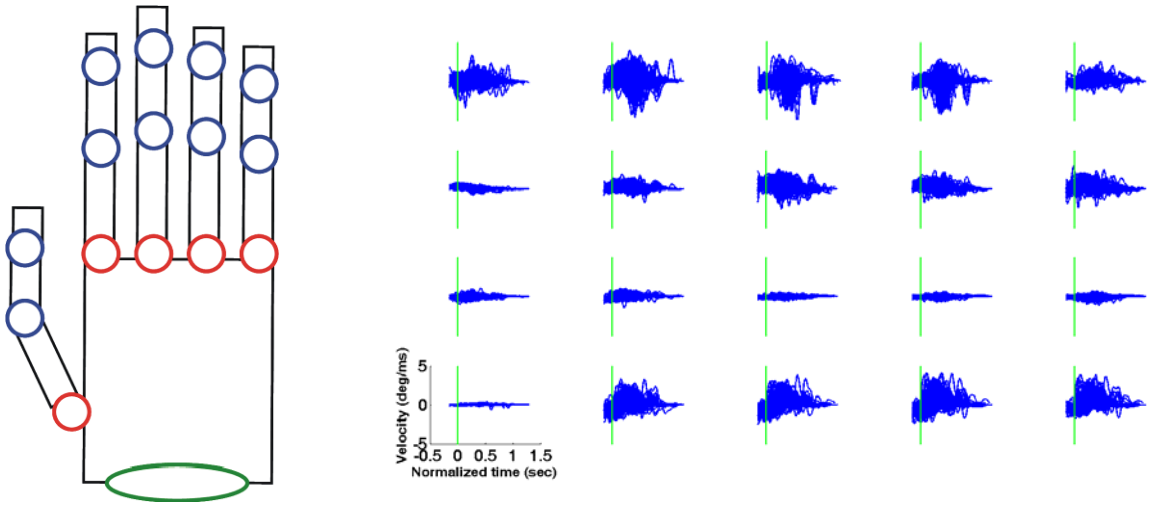

Figure 16. Trajectories across days

Each plot in the right figure represents a different DoF. An illustration of the hand is shown in the left panel for comparison. The blue joints are 1-DoF flexion joints, the red are 2-DoF flexion/abduction joints. All of the blue trajectories were combined over many days when the animals grasped the small handle in the horizontal presentation. The first column shows the angles for the joints of the thumb. Columns 2 through 5 correspond to the 1st, 2nd, 3rd, and 4th fingers respectively. The bottom row shows the flexion MCP joints of the fingers. Moving up the rows: the abduction angles of the fingers, the PIP angles, and the DIP angles. The figure of the hand on the left can be overlaid onto the trajectory plots for easy interpretation.

Combining just those trajectories for a single object presentation across days would produce a kinematic data set with such a large standard deviation that the mean would not be an accurate characterization of the data. We have separated a single joint from the population to better understand the normalization procedure (Figure 17).

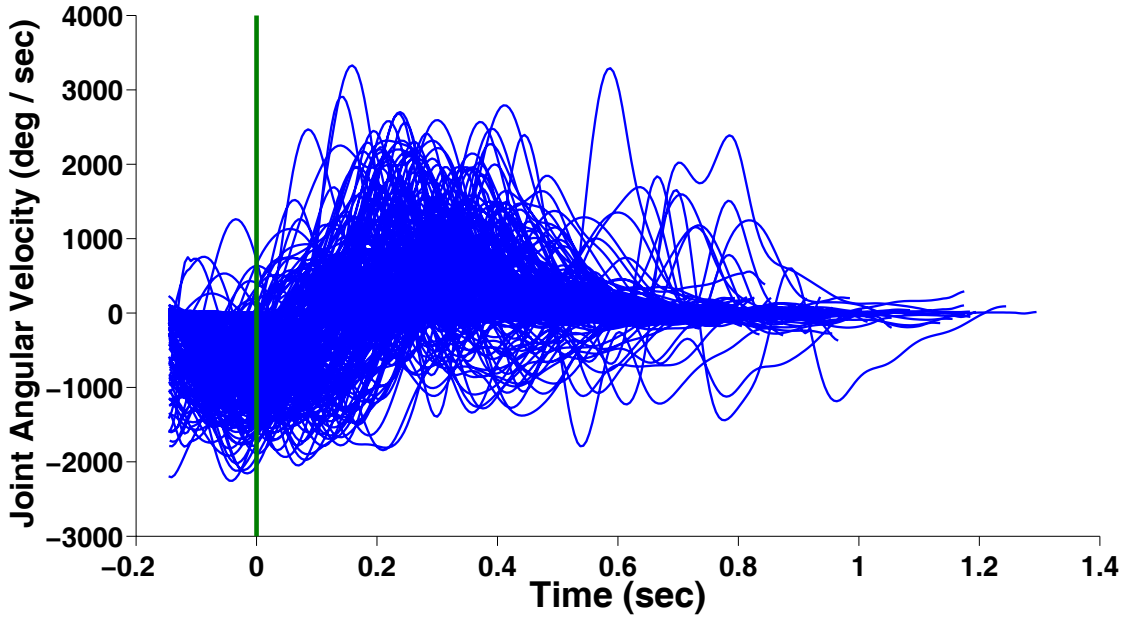

Figure 17. MCP1 flexion over many days

Each blue trace in this figure represents the movements from the beginning to the end of each trial. The zero time corresponds to the start of movement recorded by the behavioral computer.

We normalized the temporal variability by re-sampling each trajectory to only have 100 data points (Figure 18 A).

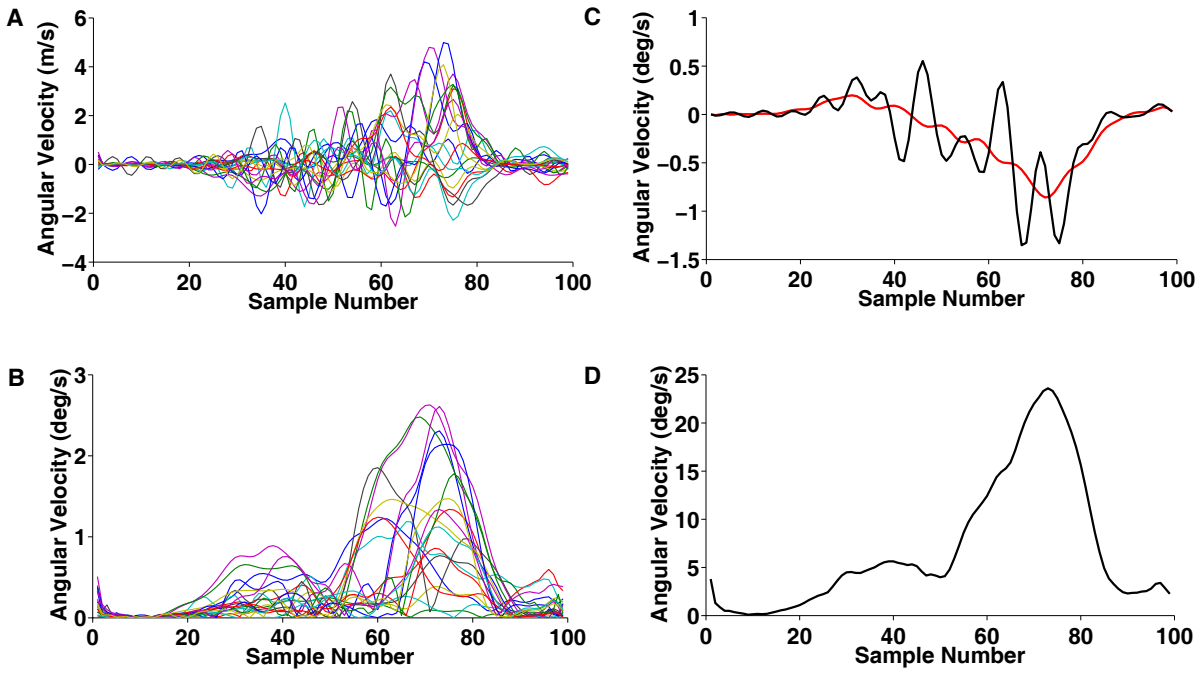

Figure 18. Hand angle and velocity

Figure A shows a 100 point joint angular velocity trajectory for all 20 DoFs. Each colored trajectory represents a different joint. Figure C shows a joint angular velocity smoothed trajectory. The black trajectory is the raw velocity data calculated for the first finger DIP joint. The red line, the smoothed trajectory, was created using a 10 sample box filter. The absolute value of velocity tracings of 20 different joints in a single trial is shown in Figure B. Figure D is the sum of the curves in Figure B. This is the sum hand velocity over a trial.

The initial alignment procedure was to normalize both the joint angle and joint angular velocity trajectories to 100 samples. The angular velocity was calculated from the instantaneous difference between measurements. Figure 19 shows twenty joint tracings over a single trial normalized to 100 samples. The zero sample number in this data corresponds to the end of hold A, and the end sample represents 150 ms before object touch was detected. The joint angular velocity trajectories were smoothed using a 10 sample box filter (Figure 18C). The absolute value of the joint angular velocity trajectories for the 20 DoFs (Figure 18B), were summed to

produce a single curve corresponding to the total finger velocity for a trial. This method decreased the complexity of hand shaping to a single velocity curve. The peak of the velocity curve (Figure 18D) was called the maximum hand shape velocity, only used to define epochs of the reach. Ten percent of the maximum was used as a cutoff to analyze the start and stop of hand shaping.

In this step each grasp is still a unique entity, and no combining over days has occurred. A goal of combining this data over many days was to select a summation method that would produce a set of trajectories with minimal variability. In this way the mean will be an accurate representation of the data set. The trials for each object presentation (see section 4.1) were separated under premise that the variability is less for one object presentation than the variability across presentations.

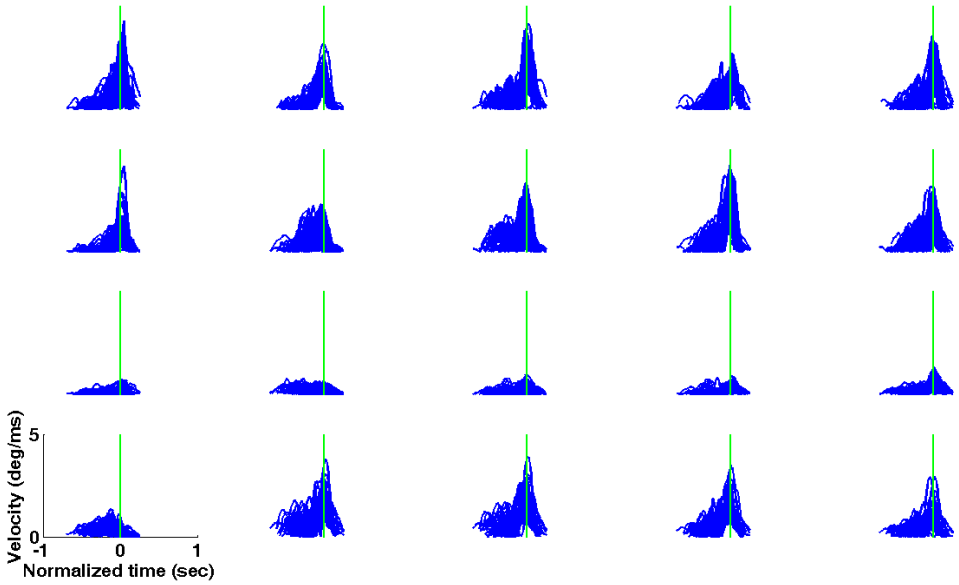

Figure 19. Aligned joint velocity tracings

Each plot represents a different DoF. All of the trajectories are combined across days when the animals grasped the small handle in the horizontal presentation position. The first column shows the angles for the joints of the thumb. Columns 2 through 5 correspond to the 1st, 2nd, 3rd, and 4th fingers respectively. The bottom row shows the flexion joints of the fingers and thumb. Moving up the rows: the abduction angles of the fingers and thumb, the PIP angles, and the DIP angles.

All the trajectories corresponding to a specific object presentation were combined by aligning the peak hand shaping velocities. This created 64 different data sets, one per object presentation. The number of trials that correspond to a single object presentation in each data set varied between 267 and 445, this variability was secondary to difficulty tracking the hand when certain objects were presented (especially monkey B). A perfectly recorded object grasp could have 445 trajectories in this analysis (89*5). The recording was completed over 89 recording sessions. 327 cells were used from all the sessions.

The neural data went through the same alignment procedure. The corresponding bin size necessary to normalize the kinematic trajectories was used to calculate a 100 bin firing rate vector for each movement. The lag between firing and movement was maintained at 150ms average for all cells. The neural data across bins corresponding to a presentation were averaged. In this way each neuron was represented by an average 100 bin firing rate vector per presentation. The number of data samples fit with linear regressions was on the magnitude of 2,500-5,000 data points.

2.6 EXPERIMENTAL DETAILS

The goal of this work was to correlate orientation and hand shape kinematics with single unit motor cortical activity. A single object was presented at seven orientations (horizontal/straight, -60 degrees roll, 60 degrees roll, -60 degrees pitch, 60 degrees pitch, -60 degrees yaw, 60 degrees yaw) to test wrist orientation. Ideally these targets would have also been presented in a four target (up left, up right, down left, down right) center out task, to analyze arm velocity. The Denso robot and tool changers used in this study only have a 12 object capacity. If all of these features were to be studied per cell, it would constitute 12 objects * 4 locations * 7 orientations * 5 repetitions = 1,680 trials. This would allow for analysis of all interactions between wrist orientation, hand shape and arm translation to be explored.

Due to time constraints of acquiring neural recordings from individual motor cortical cells 1,680 trials per session was not realistic. With the limited number of trials per session, we focused on hand shape and wrist orientation. Thus all objects and seven orientations were

presented at the center of the monkey's work space. This allowed for all second order interactions between orientation and hand shape to be explored. The number of objects used during this study was based on results from the kinematic data (see section 3.1). The final object set comprised of ten objects depicted in Figure 20.

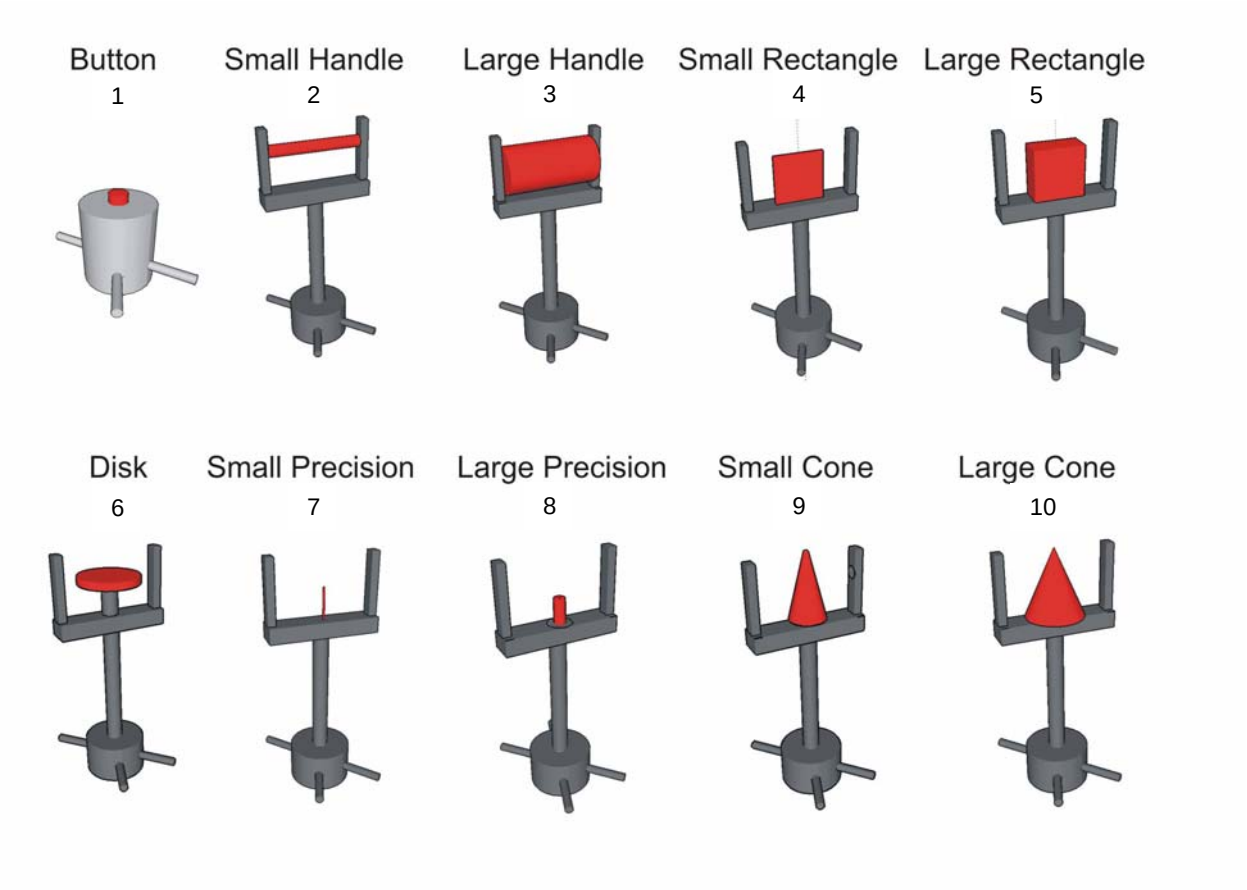

Figure 20. Graphical representation of objects.

This illustration shows the ten objects used in the reach-to-grasp experiment. The number listed below the name of the object is used as a reference throughout the remainder of the text. The portion of the object that the monkey interacted with is shown in red. The lower portion of each object, the circular portion with prongs extending from the interior, is the tool changer attachment.

3.0 KINEMATIC ANALYSIS AND GRASP SYNERGIES

The primate hand is a complex system containing 27 bones, 18 joints, and 39 intrinsic and extrinsic muscles [74, 75] with a potential for over 20 degrees-of-freedom for hand shaping [37]. Movement of the fingers requires a coordinated interplay of both extrinsic and intrinsic muscles [3, 4, and 5]. In this section, the kinematics of reach-to-grasp movement will be analyzed using dimensionality reduction techniques for two reasons. The first is the possibility that the brain takes advantage of finger correlations to build a lower-dimensional controller to simplify the neural grasp controller. Secondly, from a prosthetics standpoint, attempting to control a robot with 23 independent DoFs with a neural signal could be incredibly difficult and completely unnecessary for accurate and anthropomorphic hand movements. In light of this, we will to explore lower dimensional models to come up with a better grasp control scheme for prosthetics.

There are numerous methods that one can utilize to simplify grasping movements. Two general approaches used are bottom-up and top-down. The bottom-up approach elucidated individual components to construct models that encompass the entire hand. Other researchers have adopted a top-down approach to study the hand as a unit. These studies focused on establishing a set of principles that describe the variability in hand grasping shape with few variables [1, 35, and 76]. In these experiments, humans were presented with objects of various shapes and joint parameters were recorded while the hand was grasping. A few problems were

highlighted in these early studies. The first was the need to acquire data from many simultaneously moving, closely-spaced DoF. The second was the necessity to elicit many different hand shapes so the entirety of grasping space was well represented in the data set (both are further discussed in section 3.1.1 and 3.1.2). In the past, these issues have constrained the collected data. In the current work, we have meticulously addressed these problems with the intent of collecting copious, accurate data.

Researchers have used various methods to acquire real-time movement parameters from their subjects. Some of these methods include magnetic coils, potentiometers across joints, active light emitting diodes and passive reflective markers. Many systems have been commercially created from these technologies for specific experimental designs (Gait, Eye tracking, Data Gloves). However, no such system exists for studying grasping movements of monkeys. In many of the previously mentioned grasping experiments, the limitations of the data collected were secondary to technological constraints that caused researchers to sacrifice the number of DoFs measured simultaneously from the hand during grasping [1, 35, and 76]. In the present study, we implemented a passive recording system capable of streaming real-time three-dimensional marker data from multiple sources and developed our own algorithms for processing these data (Figure 21).

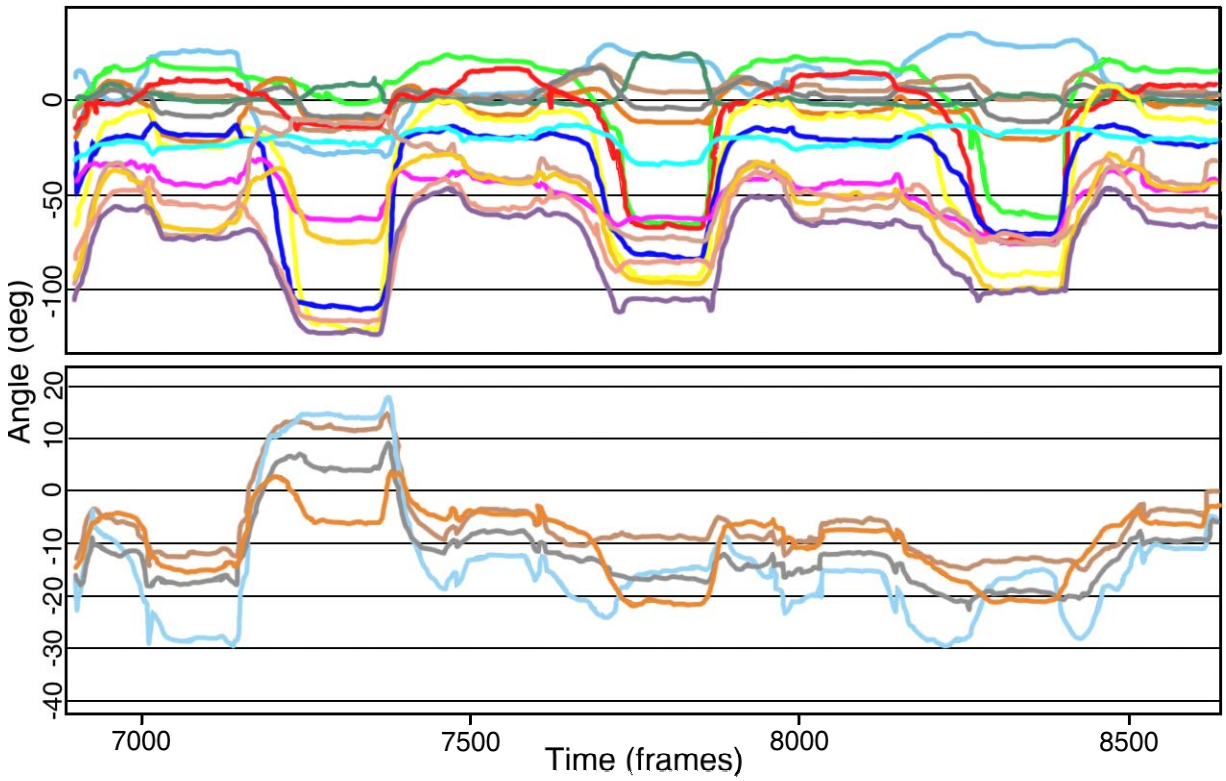

Figure 21. Continuous real-time joint angle data

This plot shows continuous measurements collected from 20 DoFs recorded during the reach-to-grasp task. The y-axis indicates an angle automatically calculated by the system, the x-axis indicates the frame number. In this section a frame number is a 5ms increment of time in which the motion tracking system samples data from all hand markers.

As mentioned above, measuring high resolution joint angles of the hand has been a challenging problem (Highlighted in section 2.3.2). One study used a large data glove with imbedded strain gauges to estimate joint angles [35], but this cannot be used in the small frame of a rhesus monkey hand. Other researchers have used systems similar to ours but with differences in marker placement and less sophisticated angle calculation algorithms [1]. We have found that details such as the marker placement relative to a joint/segment are an important factor contributing to joint angle estimation error (Section 3.1).

3.1 OBJECT SELECTION

To generalize our findings, we chose a set of objects that elicited a wide range of grasps. Two factors constrained the number of objects we could use. First, the robot that presented the objects only had space for a limited number of objects. Second, the time allotted per session was limited by our ability to maintain isolation of the recorded unit. These two factors made object selection a critical design factor. In our case, the object set must elicit a wide variety of grasp shapes with a minimal number of different objects.

The objects in this study were chosen through an iterative process. Object selection was governed by the desire to elicit the largest excursion for each joint using the fewest number of objects. A literature review was performed to identify common hand shapes and common object features that elicited these shapes. We concluded this analysis by constructing a list of 24 objects. These objects were machined from acrylic and presented to the monkey while its hand was being tracked with a Vicon® motion capture system. The object presentations were consistently and systematically put forth with an industrial robotic arm.

The notion of how a certain object feature alters monkey hand configuration is a difficult variable to quantify. In light of this, we created a metric to determine the importance of each object in the data set; cost of removal (Figure 22). This cost is defined as the percentage of unique angles lost when an object is removed from the set. With high percentages a large portion of unique joint angles in the data set will be lost. In the first iteration of object selection, each object was presented to the monkey. The “unique joint angles” were calculated for each object. Unique angles are defined as those that are specific to a single object presentation (Figure 22).

For instance, the joint angles recorded for an object that is very different from all other objects will produce a high number of unique angles. This number of unique angles is then divided by the total number of angles. This fraction is transformed into a percentage and labeled as the cost variable. An example of this process can be seen in joint DIP2. All of the joint angles measured during object 4 presentation are unique compared to other objects. This is displayed in Figure 22 as the diamond for object 4 that is separate from the others for that joint. This object has a high cost of removal for the DIP2 joint. The two objects (3-blue and 4-orange) with the highest overall cost have been highlighted with large numbers.

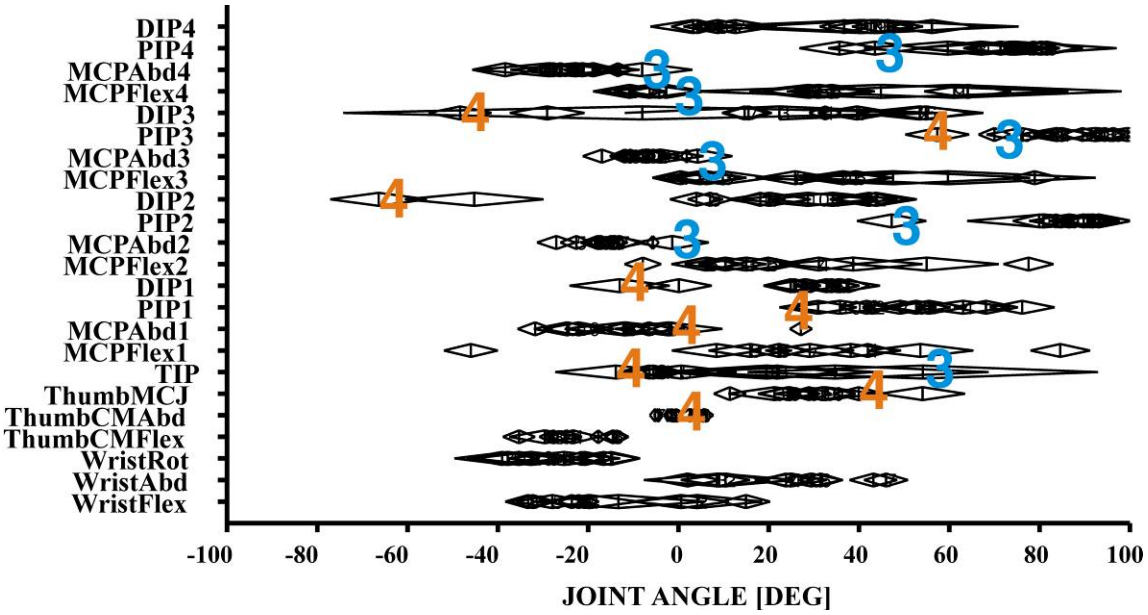

Figure 22. Joint angle excursion as a function of object.

Each of the DoFs was labeled on the y-axis. The x-axis represents the joint angles measure. Each diamond corresponds with a different object. When a diamond is separated from all other diamonds, this indicates an object has a high cost. The line through each diamond is the mean joint angle. The apices of the diamonds show the min and max angles measured for the numbered object. Objects three and four have been labeled to show the two objects with the highest cost.

After the first iteration of this process was completed, 11 objects, all with costs less than 4%, were removed from the original 24 object list.

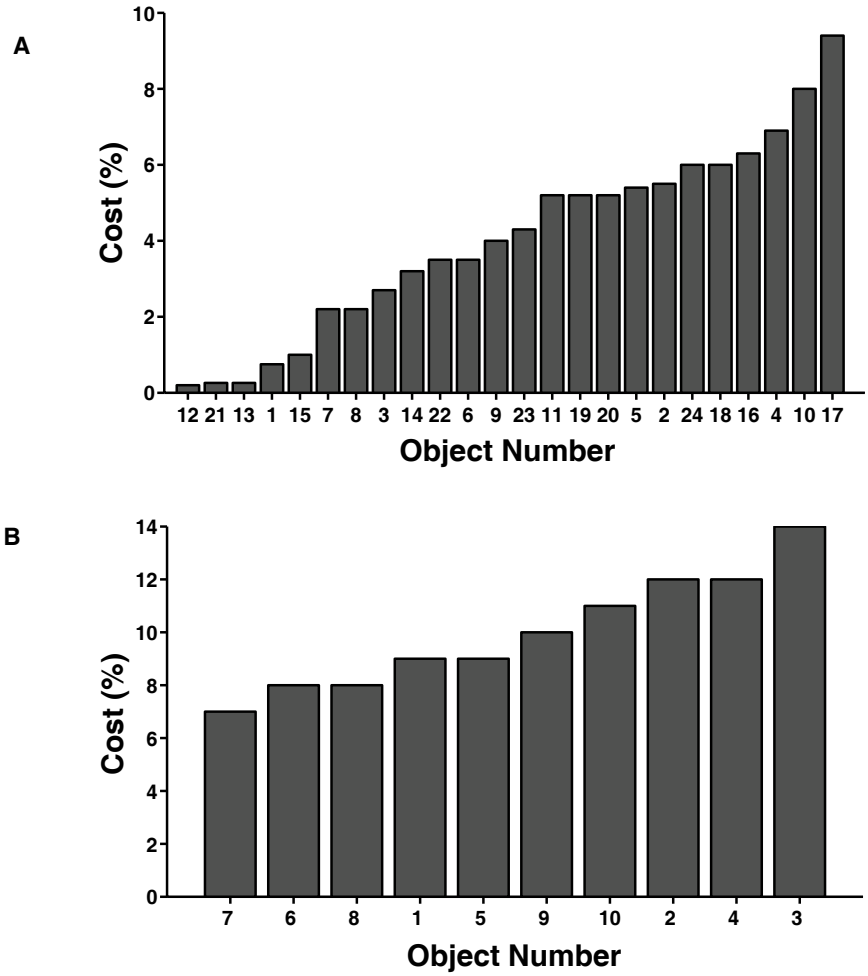

Figure 23. Cost analysis for original and final object set.

Figure A shows the cost values calculated for the original 24 objects. An arbitrary cutoff value of 4% cost was used to determine which objects would be continued to the next iteration. In this graph the x axis is the object number and the y axis is the cost in percentage of unique angles that would be lost from the data set if this object were removed. Figure B shows a similar plot for the final ten objects used in the reach-to-grasp task.

This process was continued through several iterations. With each iteration fewer objects were removed from the data set and the remaining objects were slightly reconfigured to correct for problems encountered in the previous iteration. The final set of ten objects was chosen through four iterations of this process (Figure 23). Objects were not removed in all iterations because the objects were slightly reconfigured to produce larger joint excursions. The final set of objects (Figure 20) was not merely ten objects from the original object set. The final objects consisted of those that had the largest number unique joint excursions, or the largest cost, associated with them.

3.2 JOINT ANGLE ACCURACY

Marker placement can be a process that is both mundane and challenging. The small monkey hand makes marker confusion by the reconstruction algorithm more common than with large segments, and placement more critical for accurate joint angle reconstruction. If a segment is large enough to accommodate multiple markers (a.k.a. Femur), the placement process is rather simple because multiple markers can be located on each segment. For accurate joint angle reconstruction the markers should span the entire length of the segment. For example, with a long segment like the femur, many markers can be placed along its axis with at least one near the knee and another near the hip. This will minimize marker clustering and maximize the measured span of the segment. Most of the bones in a monkey hand, however, are too small to accommodate multiple markers that can be tracked individually by the cameras.

Some researchers have solved this problem by placing a single marker over the joint in question [1]. In this work, the researchers used the absolute marker positions to calculate joint angles. Others, applying a similar technique, used an offset to estimate joint centers [73]. In these studies the researchers used a simple offset to estimate the joint center from the absolute marker location. In the current study, we used a single marker placed in the middle of the segment and a sophisticated algorithm to calculate joint centers from marker positions. Each of these techniques has its unique benefits and problems.

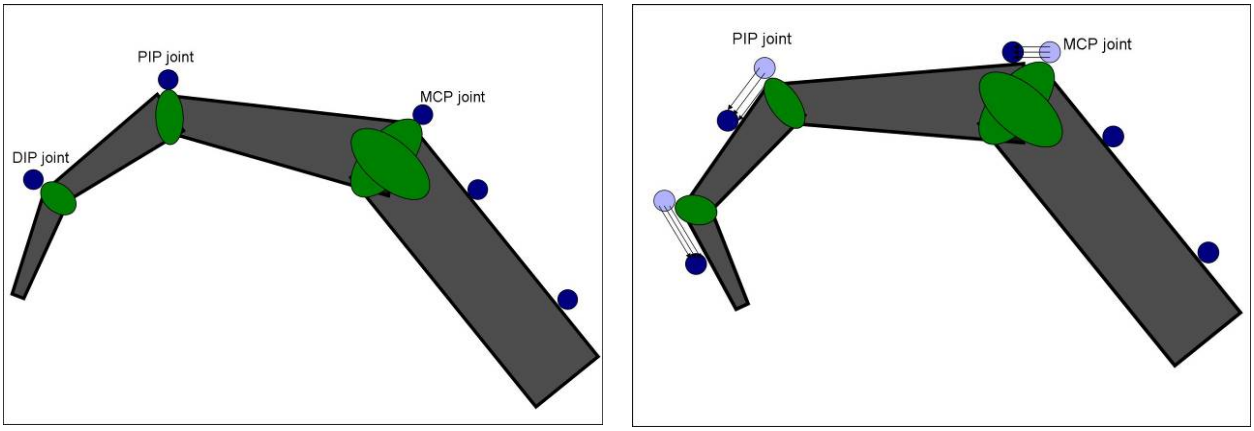

Figure 24. Marker movement with markers placed directly above a joint.

In both illustrations the green ellipses are joints, the dark gray portions between the ellipses are bony segments and the blue circles above the joints are markers. The number of green ellipses per joint corresponds to the number of DoFs for that joint. In this graphic the markers are placed directly on top of the joint in some default posture. The left panel shows a finger in the default position. The right panel shows the same graphic when the finger is in a flexed position. Based on the degree of flexion the marker moves in a non-linear way around the joint (shown as the light blue circles relative to the dark blue circles). This non-linear marker movement creates joint angle estimation error that is difficult to account for. We estimated using a human model and a goniometer that when using this technique to calculate joint angles create 15-20 degrees of joint angle error.

One strategy utilized to measure joint kinematics of the hand in the past has been to place the markers directly over the joint of interest [1] (Figure 24 and 25). When this marker placement was utilized the joint angle calculations were done in two ways.

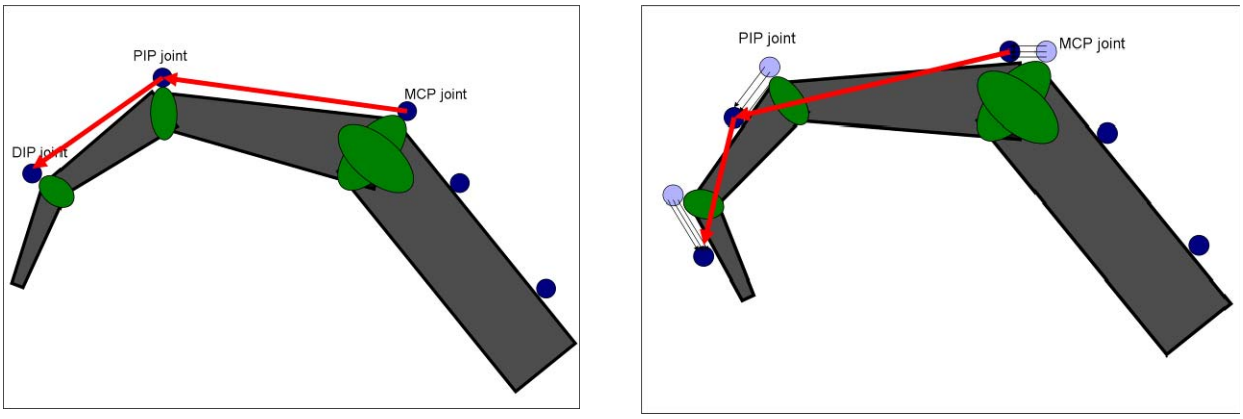

Figure 25. Joint angle calculation and graphic of joint angle error estimation.

The same color scheme has been used as the previous Figure. The red arrow indicates the vectors calculated between each marker. These graphics show the simple vectors used for joint angle calculation. The right panel shows how the marker movement and vectors used from the marker data can give a poor estimation of joint angle.

In one method, vectors are drawn between three adjacent markers (middle marker over joint center) and the joint angle is the angle between these adjacent vectors. This is the simplest, but most error-prone method for single marker segments. Unfortunately, locating the markers precisely over the joint centers is very difficult and leads to error in the angle calculation. The primary component of marker position error is that skin over the joints move nonlinearly as a function of joint angle. Furthermore, the relative position of the skin over a particular joint depends on the position of the other joints in series. For example, flexing the MCP joint will

tighten and shift the skin over both the PIP and DIP joints. Because the marker position error exhibits complicated interactions across joints, it can be difficult to compensate in reconstruction algorithms. Using a goniometer, we estimated that the shifting skin can cause 15-20 degrees of error in joint angle measurements, when the markers are located on top of the joints in human subjects. Although it is easy to implement, this approach is prone to large errors in joint angle estimation.

An attempt to address this problem was made by applying a continuous offset function to the marker data. This function accounts for the changing proximal to distal segment profiles but does not address the error caused by the second and third issues above. This method uses a relatively simple measurement of proximal to distal segment width and applies this as a continuous offset function. Another benefit of this method is that joint angle calculations are determined from joint centers rather than marker positions. Unfortunately this also adds unnecessary error to the joint angle calculation by placing the markers directly over the joints.

In order to make more accurate joint angle calculations, we placed our markers in the center of each segment. The skin, and therefore the markers, moves much less in this location (Figure 26). This center segment marker placement approach is less non-linear, but makes it more difficult to calculate joint angles from individual markers. Before the current work, single-center segment marker placement had not been used to calculate joint angles from joint center positions. We developed an algorithm to estimate joint centers which were then utilized to establish an accurate estimate of joint angles (for details see section 2.3.3).

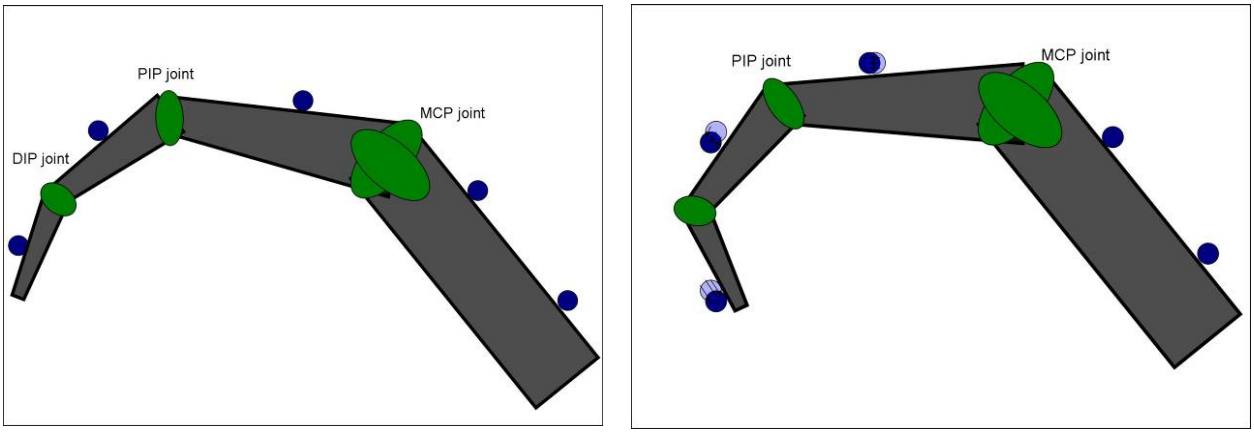

Figure 26. Marker movement with inter-segmental marker placement.

The left panel shows initial marker placement used in our experiment. There are two markers on the most proximal segment. This bone was the only segment large enough for two markers and was used as an anchor to establish the planes of movement for each finger. The more distal segments correspond to the proximal phalange, interphalangeal bone, and the distal phalange. The right panel shows the relative motion of the markers during joint flexion. Using a goniometer method we estimated that this sub-millimeter movement contributed to an error of one to five degrees in joint angle accuracy (as compared to 15-20 degrees in the previous example).

A clear advantage of this joint center estimation is that it increases the accuracy of joint angle values. The inter-segmental marker placement produces less error from non-linear marker translation during movement. Directly calculating angles from joint centers without the necessity of a continuous offset function also increases joint angle accuracy. The joint centers were estimated over the course of a recording session in an iterative fashion using the most recent 5,000 frames. This iterative process allowed us to account for small marker translations down the shaft of the finger that would occur during the course of the recording session. This was important for accuracy over the entire recording session.

In the current study monkeys wore kinematic tracking gloves. During the course of a single session, the glove had a tendency to slowly migrate down the monkey's hand (1-3mm). The recursive nature of the center estimation procedure (detailed in Section 2.3.3) compensated for the marker drift. This algorithm allowed us to test the accuracy of the system and optimally adjust our algorithms.

3.3 DIMENSIONALITY REDUCTION

Recent advances in computing and data collection have generated an information overload in fields such as astronomy, biology, engineering and neuroscience. With high-dimensional datasets, it is often found that subsets of variables are unimportant for understanding the underlying phenomena of interest. While certain computationally expensive novel methods [77] can construct predictive models with great accuracy from high-dimensional data, it is still of interest in many applications to reduce the dimension of the original data prior to modeling of the data.

3.3.1 Intuitive Kinematic Analysis

Figure 27 shows a detailed view of the MCP1 joint during different reach-to-grasp movements.

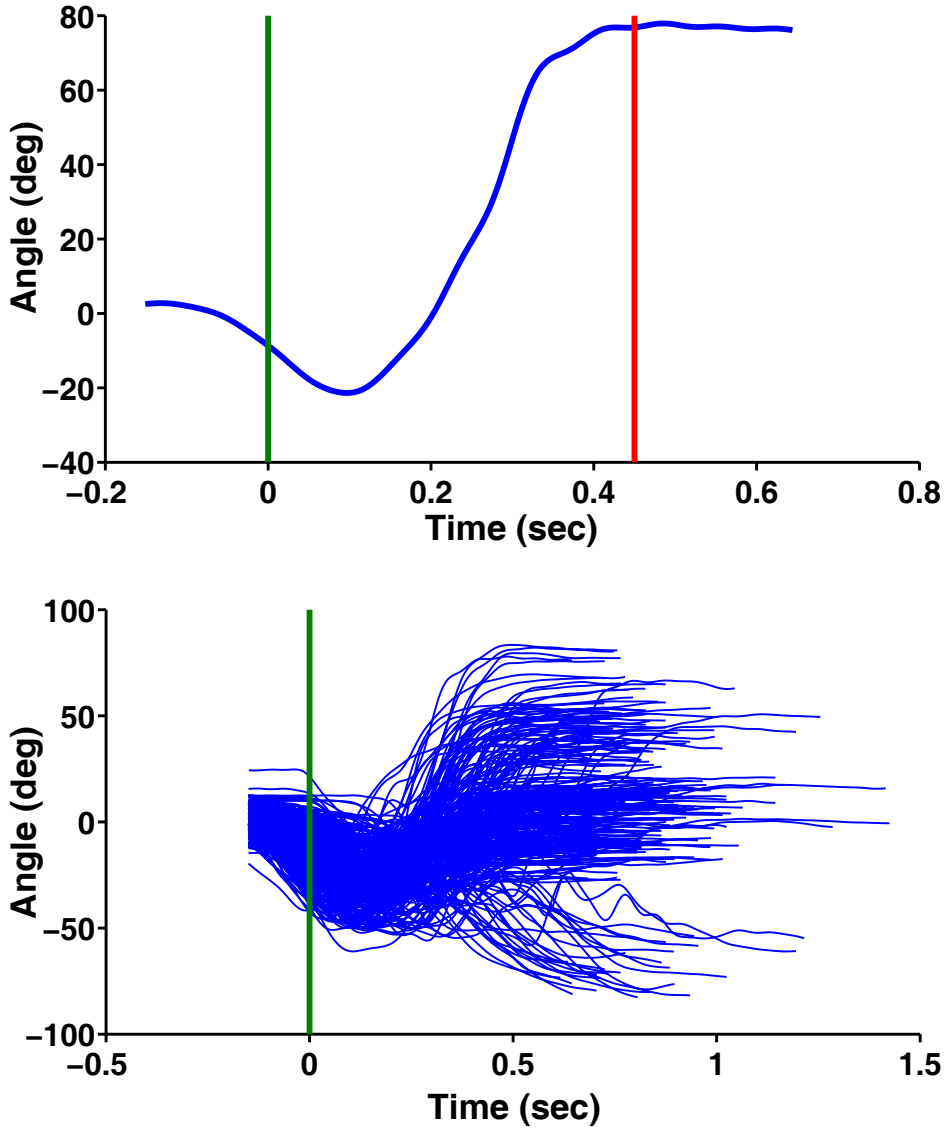

Figure 27. MCP1 joint movements.

The top panel shows an individual trial showing the MCP1 flexion/extension joint angle during a movement to the small handle. The vertical green line at time zero indicates the detection of button release. The vertical red line is the beginning of the Hold B period. The lower Figure shows the same MCP1 joint for all (both successful and non-successful) trials in a single session. Once again, the vertical green line indicates the go signal. A general trend toward extension is seen in the early phase of movement across objects in the lower Figure. This extension trend can be generalized to a characteristic in the early opening phase of reach.

These joint movements illustrate a key component of preshaping. This joint shows movement throughout the reach (between the green and red vertical lines) in a smooth fashion and plateaus at a final joint position as the hand nears the object. Another component of preshaping can be seen in the lower plot. All of the movements from a session contain many different objects in many different orientations. The monkey shows a common “default” opening posture throughout all objects grasped. This can be seen in the lower plot as a general trend in the negative direction (first finger extension) early in the movement followed by a more individualized modification of flexion extension. Essentially, the animal starts with a characteristic opening phase that is fairly constant across objects with later modification depending on the specifics of the required grasp. These Figures show that monkey movements have similar preshaping characteristics to those described previously in humans [41, 44, and 45].

In the current study it was found that the monkey moves all DoFs simultaneously during any single reach to grasp movement, the movement was smooth, and the joint angles were correlated throughout the reach. The movements plotted in Figure 28 are from six presentations of a single object at different orientations and show a high degree of covariance between joint angles. The joint angle data output show that the metacarpal phalangeal (MCP) flexion, MCP abduction, and interphalangeal joints tend to covary (Figure 28-B, C, D, E, F). These are the same joints that move together when opening and closing the fist.

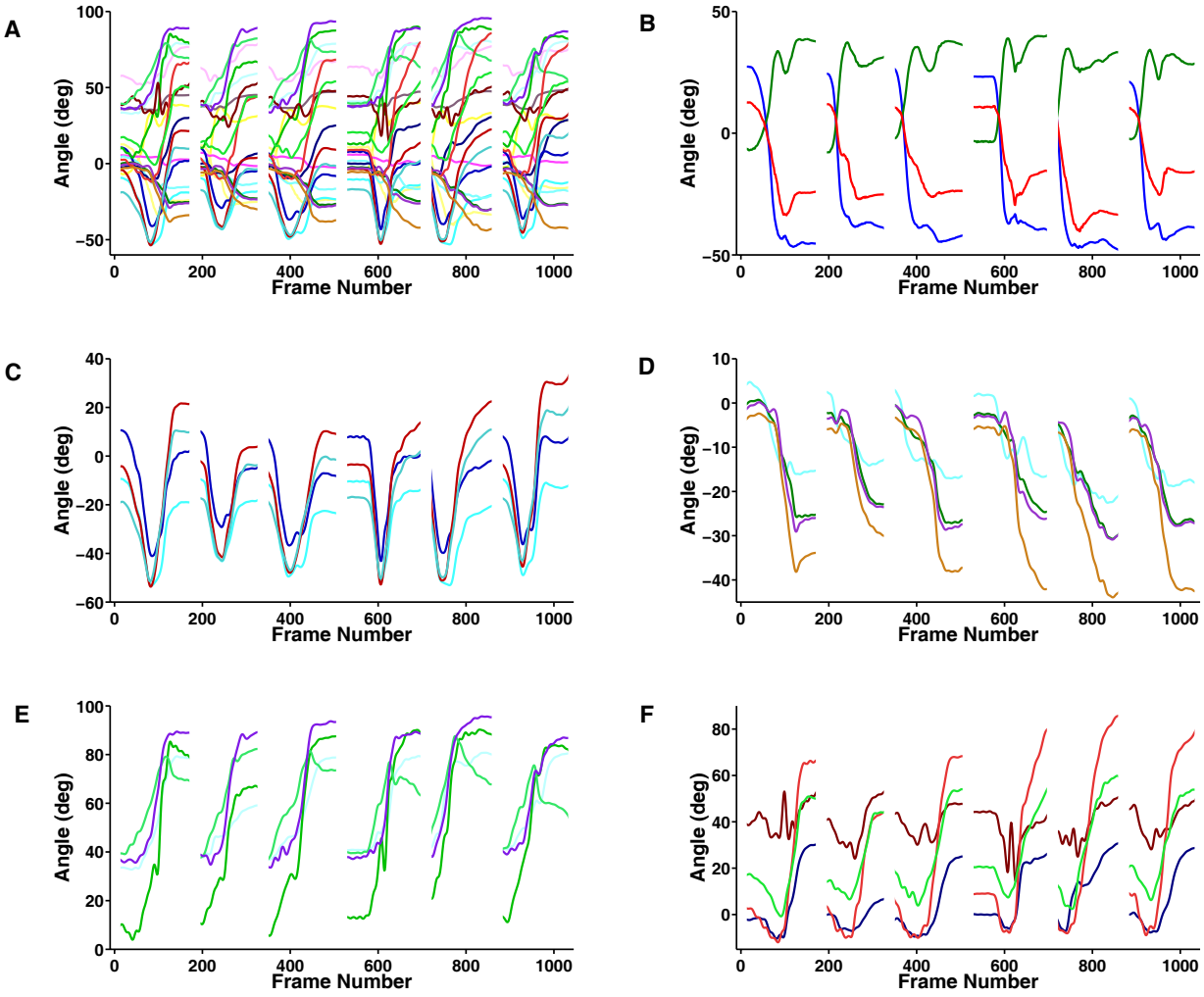

Figure 28. Correlated grasping movement.

Joint angles for multiple joints over six consecutive trials. A group of six trials was selected from the data set for illustration. The data in panel A shows all the DoFs of motion tracked simultaneously throughout the reach-to-grasp movement. Panel B shows the wrist DoFs isolated for the same six movements. This data has been separated by joints that have similar function across different fingers. C, D, E, and F illustrate the grouping of MCP flexion, MCP Abduction, DIP and PIP joints (respectively). These groupings show a basic correlation among these functionally similar joints.

Joint correlations were tabulated in a color-coded correlation coefficient matrix (Figure 29). The coefficients were grouped by the joint type. For instance, all the MCP flexion/extension

DoFs have been plotted next to each other. This is also true for the MCP abduction/adduction, proximal interphalangeal (PIP) joints, distal interphalangeal (DIP) joints, the wrist, and thumb DoFs. A high correlation is illustrated by a white square, a low correlation is shown as an orange square, and an anti-correlation is shown as a black square. The autocorrelation line can be seen as a white diagonal traveling from upper left to lower right across the figure. The clustering of correlation in this plot has been highlighted by a black outline around similar joints. The large white and yellow area in this plot indicates that the joints with similar physiologic action across many different fingers are correlated to one another. In other words, the fingers and individual joints across the fingers move together in a coordinated fashion. This Figure also shows how little correlation exists between the individual DoFs of the wrist and the rest of the fingers. This may be a natural physiologic feature or may merely be a function of the experimental design. The presentations of objects were selected to isolate different final wrist angles with similar hand postures.

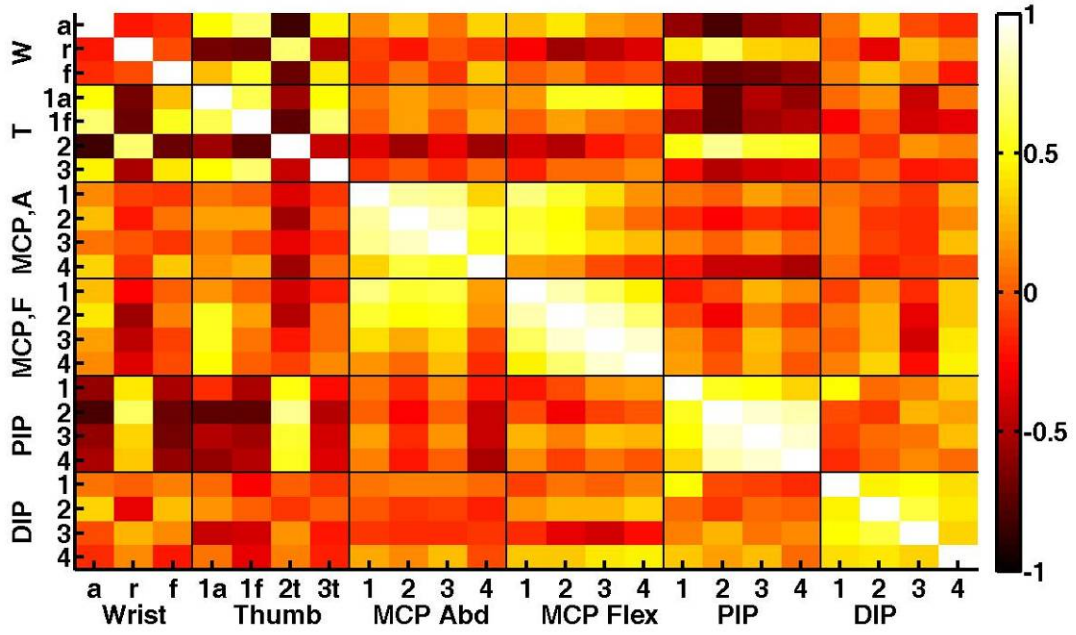

Figure 29. Joint angle correlation matrix.

Each box is a representation of the correlation coefficient calculated for a joint pair. The data used for this Figure was from the first 30 sessions of kinematic data from monkey V. The color map to the right indicates that a white square is a joint pair with a correlation of 1, a black square is a joint pair with a correlation of -1, and an orange square indicates joints that show little correlation. The joints have been arranged so those with a similar physiologic function across fingers are grouped together into a block of 3 or 4 (depending on the joint). The white diagonal in this Figure represents an autocorrelation line, and the black vertical and horizontal lines help separate the functional groupings. The left of the Figure shows a list of the types of joint groupings.

The correlation matrix is a helpful way to visualize how joints with a similar function, on different fingers, are highly correlated. Figures 28 and 29 allow for some intuition that principal component analysis will work well in reducing the dimensionality of the grasping data. However, these Figures do not show what the eigenvectors are likely to be. The covariance matrix has been plotted (Figure 30) to give some intuition as to the likely coordinated joint displacement vectors from this analysis. The covariance matrix was organized in the same way

as the correlation matrix, but the clustering that occurs is different. Flexion of the PIP and MCP joints tend to have high covariance values across fingers. This would suggest that large weights will be placed on these joints in dimensionality reduction.

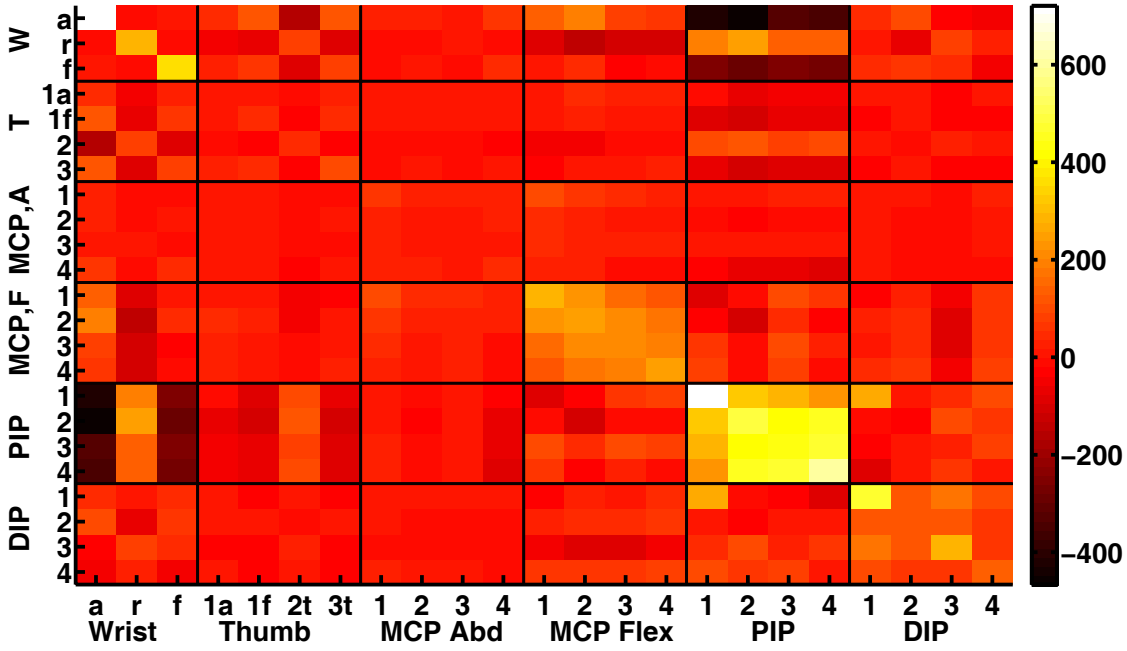

Figure 30. Joint angle covariance matrix.

Each box represents the covariance of joint pairs. The joints have been arranged in a similar way as the previous Figure. It is evident that this highest positive covariance is within the PIP and the MCP flexion joints. This covariance matrix indicates that the first two eigenvectors from this data set should account for much of the variance in the PIP and MCP flexion joints.

3.3.2 Basics of Dimensionality Reduction

This study will investigate the application of linear dimensionality reduction techniques to the grasping dataset. The basis of any linear dimensionality reduction technique is that each of the resulting components of the new variable is a linear combination of the original variables. We will apply principal component analysis (PCA). Which are also known as singular value decomposition (SVD), the Karhunen-Loeve (KL) transform, the Hotelling transform, and the empirical orthogonal function (EOF) method [78]. The application of PCA will reduce the dimension of the data by finding orthogonal linear combinations (eigenvectors) and rank them by the explained amount of variance in the original variables. A simple example of this is shown in Figure 31 illustrating how PCA can simplify this two dimensional data set.

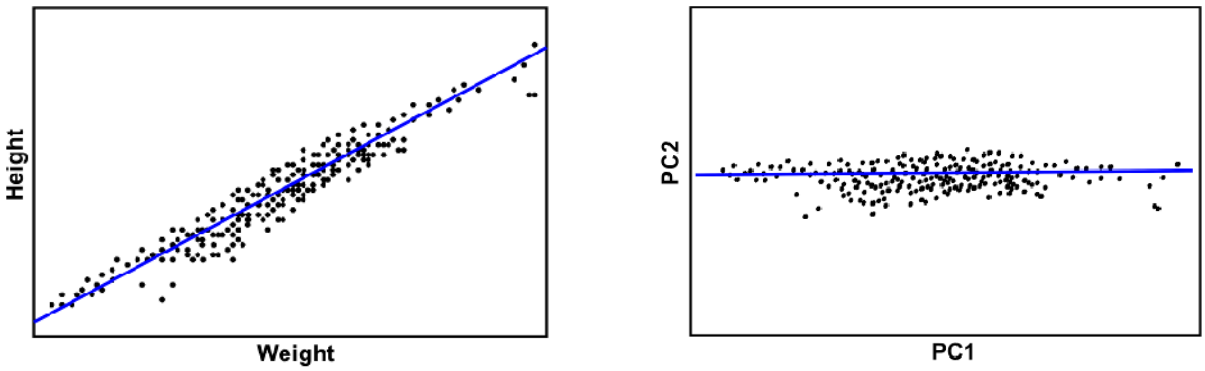

Figure 31. Dimensionality reduction example.

Simplified example of how a two-dimensional data set that is highly correlated can be accurately represented by fewer variables using PCA. The left plot is 100 heights and weights plotted on a Figure. The blue line is the first eigenvector plotted in this two-dimensional space. Each of the variables in this plot has a large distribution of data points in both dimensions. The plot on the right is the same data set displayed in eigenvector

space. In this plot the majority of the variability in this data is captured along the first eigenvector axis. Therefore a large source in the variability in this two-dimensional data set can be represented by a single variable.

3.3.3 Application of PCA to Grasping Data

For illustration and ease of understanding, the following section will only refer to the static phase of grasping measured 50ms before the beginning of the 'Hold B' (detection of object contact). For each trial performed in this experiment, there is a single static hand shape that was dependent on the object and its orientation. Both are considered a single presentation, giving a total of 64 unique presentations per session. Each presentation is repeated five times, producing a total of 320 trials per session. Each presentation consists of 23 (20 hand + 3 wrist) joint angles, one for each degree of freedom. In this example, we will assume that the monkey successfully reaches all presentations five times. This example will be performed only with data acquired in a single session. Only the joints that produce hand shape are analyzed with principal component analysis, and those joints giving rise to orientation (wrist DoFs) are treated separately. This gives a matrix of joint angles that is 20 by 320…

$$A = \begin{bmatrix} J_1T_1,\ J_1T_2,...,...,...,...,\ J_1T_{320} \\ J_2T_1,\ J_2T_2,...,...,...,...,\ J_2T_{320} \\ ...,...,...,...,...,...,...,...,...,... \\ J_{20}T_1,\ J_{20}T_2,...,...,...,\ J_{20}T_{320} \end{bmatrix} \quad (2)$$

where ***A*** is a joint angle matrix with J_1 representing the first joint, and T_1 the first trial. So J_1T_1 is the joint angle measured for joint one on the first trial. The data is normalized by subtracting the mean of that joint …

$$D = A - M \tag{3}$$

where …

$$M = \begin{bmatrix} \bar{J}_1, \bar{J}_1, ..., ..., ..., ..., \bar{J}_1 \\ \bar{J}_2, \bar{J}_2, ..., ..., ..., ..., \bar{J}_2 \\ ..., ..., ..., ..., ..., ... \\ \bar{J}_{20}, \bar{J}_{20}, ..., ..., ..., ..., \bar{J}_{20} \end{bmatrix} = [20 \text{ x } 320] \tag{4}$$

This normalization produces a data set with a mean of zero for each joint. Intuitively this means that the joints with larger changes in angle during grasping will have more influence on dimensionality reduction, i.e. account for more variance across all joints. The next step in PCA is to calculate the covariance matrix from the normalized data (*D)*. This matrix looks like…

$$C = \begin{bmatrix} \text{cov}(J_1, J_1), \ \text{cov}(J_1, J_2), \text{cov}(J_1, J_3), ..., ...\text{cov}(J_1, J_{20}) \\ \text{cov}(J_2, J_1), \text{cov}(J_2, J_2), \text{cov}(J_2, J_3), ..., ...\text{cov}(J_2, J_{20}) \\ ..., ..., ..., ..., ...,

Since the data of interest has 20 dimensions the covariance matrix ($\boldsymbol{C}$) is a 20x20 matrix. It is the eigenanalysis of this covariance matrix that is the basis for PCA, and gives matrices Z and E.

$$Z = E \cdot A \tag{6}$$

Z is the matrix of scores (i.e. projection of eigenvectors). E is the rank ordered matrix of eigenvectors. The E matrix contains 20 orthogonal linear combinations of the original variables. The rank of the eigenvector is determined by the eigenvalues, or variance accounted for.

At this step, there is no data lost, and therefore no dimensionality reduction, but the original data is represented in eigenvector space rather than joint angle space. The dimensionality reduction occurs when a few of these eigenvectors are chosen to represent the original data. In this example, we have chosen the number of eigenvectors that account for at least 85% of the variance in the original joint angle data. In the static hand shape analysis, the first seven eigenvectors accounted for 87% of the variance in joint angles of the hand. Thus, in the remaining portion of this analysis we will utilize seven eigenvectors for reconstruction.

One of the benefits of using a linear dimensionality reduction technique like PCA is the ability to reconstruct the data from a reduced set of descriptors. In this context, a reduced number of eigenvectors can be used to approximate the original joint angles. This allows the user to both visualize how the reduced dimensional space perturbs the original data set and gives intuition of how the hand moves through a reduced dimensional control space. This process is illustrated in the following set of equations.

If there is no dimensionality reduction….

$$\left[A - M\right] = Z * E^{T} \tag{7}$$

where A is equal to the original joint angle matrix [20x320], Z is matrix of scores [20x320], and E is the rank order matrix of eigenvectors [20x20].

If only subsets of eigenvectors are used to describe the original joint angle data the above does not hold true.

$$R = Z_r * E_r^{T} \tag{8}$$

where E_r is a matrix [7x20] composed of the first seven eigenvectors, Z_r is a matrix [320x7] of scores and R is a matrix [320x20] of reconstructed joint angles. The matrix R does not have the proper mean, so…

$$A_r = R + M \tag{9}$$

The A_r matrix contains reconstructed values of joint angles. In this process, if all eigenvectors are used, A_r equals A (the original joint angle matrix) because no dimensionality reduction has taken place. However, if only subsets of eigenvectors are used the A_r matrix represents the hand postures through a reduced dimensional control space. With this data, the hand angles can be projected onto individual or a combination of eigenvectors. The max (+1) and min (-1) postures of the hand can be viewed in this projected eigenvector space (Figure 32). This

operation allows the researcher to visualize hand postures when the hand angles are created from only a few eigenvectors.

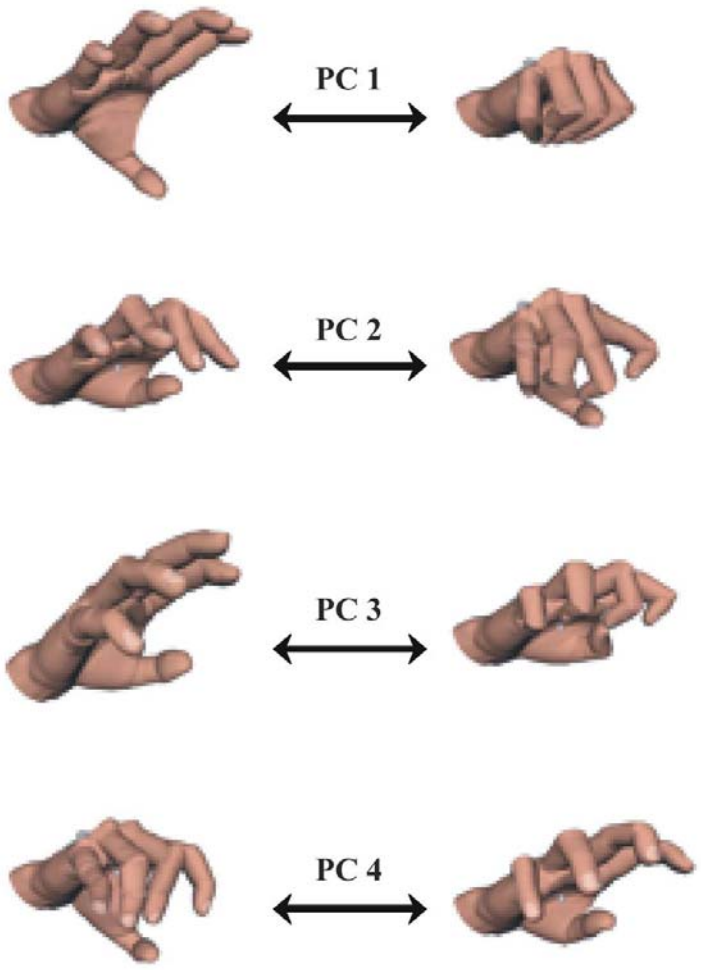

Figure 32 Hand shape projections onto the first four eigenvectors.

Visual interpretation of how the hand would move through isolated eigenvectors. Each pane represents a different eigenvector. For example the first eigenvector pane represents all 20 DoFs of the hand projected through the first eigenvector. From top to bottom these eigenvectors account for a decreasing amount of the variance in hand shape.

3.4 STATIC GRASPING SYNERGIES IN JOINT ANGLE SPACE

Something interesting happens when a person reaches to grasp an object. The hand starts to close and shape to the object in a smooth continuous manner as the hand approaches the desired object. This natural characteristic of grasping has been termed “preshaping” [38]. Another feature of human grasping is that the fingers, and individual joints, move together [38, 39, 40, 41, and 42]. These stereotypical relationships are called postural synergies and have been well characterized in previous human studies [1, 35, and 76]. A fundamental question in the current work is whether monkeys display postural synergies during grasping movements; and if so, whether these synergies are similar to those of humans. Some of the differences between the aforementioned work and ours are that this study tests fewer objects, and we have more simultaneously recorded DoFs. This change in the measured DoFs is expected to impact the “functional” DoFs found in our postural synergies, compared to those seen in humans. The term “functional” is used here to describe the number of eigenvectors necessary to account for 85% of the variance.

Are the monkey’s fingers coordinated during a reach-to-grasp task in a way that is similar to previous human psychophysics studies? Ours is the first detailed kinematic study of a monkey’s hand during this behavior. In contrast to human grasping, a monkey may show a prolonged transport phase followed by a separate shaping phase. We will characterize the coordinated action of the hand during grasping using PCA and compare these results to those from human studies.

3.4.1 What data points, and how many descriptors for PCA

Two fundamental issues in dimensionality reduction are: Which data are included in the analysis- continuous vs. non-continuous, and how many dimensions are needed to describe the variance of the original data set? The following section describes two separate methods to answer both of these questions.

The data selected for the analysis can have a profound impact on the eigenvectors. Previous work has focused on just the shape of the hand while the subject was grasping an object, and thus only used the data during that time point from each trial [35]. Others have been more interested in grasping synergies that encompass the entire reach-to-grasp movement [1, 46, and 47]. In this work, the researchers used all the consecutive data points collected as the input to PCA. This approach has two main problems, relative to our work. The first is that it is computationally very expensive to use all the consecutive data. A second, and more concerning point, is that an underlying assumption of principal components analysis is that each observation is independent. The time between data samples in this work is 5ms, and thus can hardly be considered to be independent. The challenge is then to determine the minimal number of data points that can be used in PCA that will fulfill its basic assumptions and still produce a lower dimensional space that generalizes well to the entire data set.

Equation 9 shows how joint angle data can be approximated using only a subset of the eigenvectors. This allows us to calculate the joint angles of the hand by projecting it through eigenvector space to compare it to the actual hand shape at any moment in time.

We created a method to determine which portions of data were necessary to accurately characterize hand shape. By using all of the data points recorded during an overall reach-to-grasp movement for PCA we assumed that we would get the best approximation. This data group was labeled “All” (Figure 33). However, there may be a single phase of the movement that accounted for the majority of the variance; this may be as powerful as all of the data points. These other subsets are different time points in the trial, beginning (B), middle (M), end (E) and have the maximum separation in time. The beginning point (B) was taken to be at the end of Hold A. The middle point (M) was at the moment of maximum aperture, and the end point (E) was 50 ms before the animal grasped the object (Hold B). PCA was performed on each. Utilizing Equation 9, the joint angle data were calculated as a projection through the eigenvectors for each data set. This projected hand shape data was then compared to the actual hand shape. The number of eigenvectors necessary to reconstruct the actual hand shape with 85% accuracy was plotted in Figure 33.

The data for this analysis was collected over 317 sessions from data pooled using two different monkeys. A reconstruction accuracy of 85% was obtained using the **All** data set with 7 eigenvectors. The other data subsets are then compared to the **All** group by calculating the number of eigenvectors required to reconstruct the hand shape with 85% accuracy. The groupings in this Figure show that if the beginning (**B**) or middle (**M**) of movement is combined with the end (**E**) of movement, the resulting subsets of data produce eigenvectors that can reconstruct the actual hand shape with an equal amount of accuracy as using the continuous (**All**) data. This indicates that only a portion of motion variance is captured by any single phase. The combinations of multiple phases are needed to characterize the entire data set. The variability of

joint angles in a normal trial, consisting of approximately 150 data points, can accurately be described by choosing two or three particular data points from a trial.

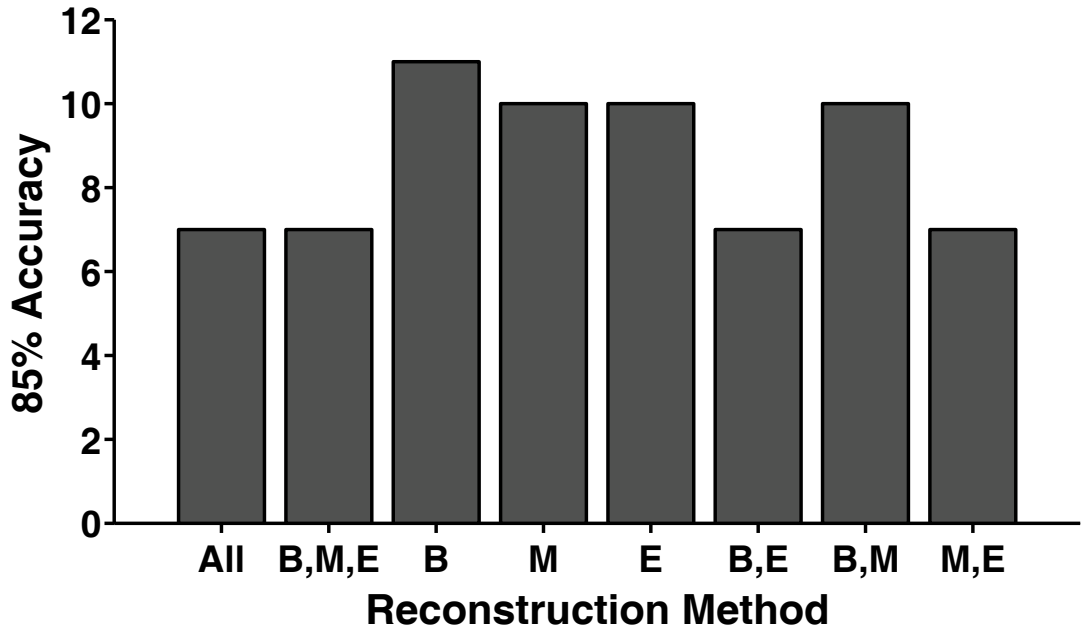

Figure 33. Data points used in PCA – reconstruction comparison.

The All data set is a set using all of the continuous data points throughout the entire reach-to-grasp movement. B = beginning of movement / Hold A, M = maximum aperture of movement, E = end of grasp / Hold B. The x-axis shows the different data sets. The y-axis shows how many eigenvectors were used to reconstruct the actual hand shape with 85% accuracy. The All group required 7 eigenvectors, along with the groups that contained the END and any of the other data points (M or B).

Another way of testing the resolution of reconstruction is by matching hand shape to object. If the objects differ from each other and the joint angles are well measured there should be a unique correspondence between measured hand shape and the different objects. The more accurate the reconstruction, the greater the number of objects identified by hand shape. We used a support vector machine (SVM) to help decide how many eigenvectors were "necessary" to

identify specific objects. This type of algorithm is used with complex data to make choices from many categories [79]. For example, in this data set we created an SVM to classify which object the monkey was grasping using joint angle data constructed from various numbers of eigenvectors (Figures 34 and 35).

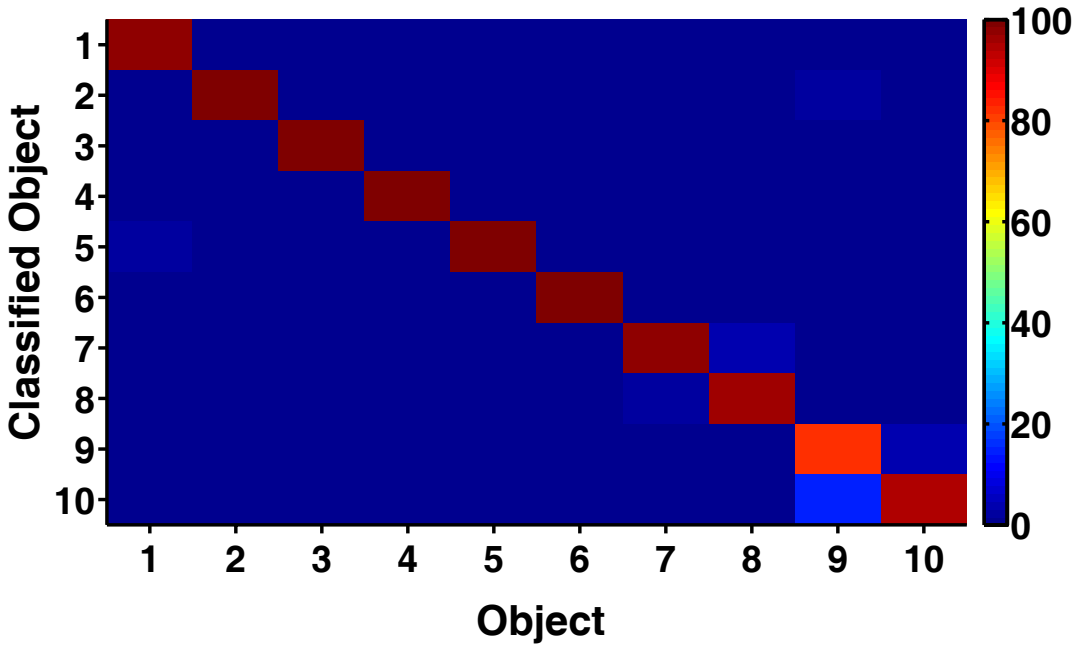

Figure 34. SVM object classification using the complete joint angle data set.

The above plot illustrates objects the SVM classified as a function of the actual object based on using all 20 eigenvectors. The 20 DoFs used in this analysis excluded the wrist DoFs. The color bar on the right of the Figure shows how successful the classifier was as a color-coded percentage. The line of unity from upper left to lower right in the plot indicates that the classifier most often chose the correct object based on joint angles used from 20 eigenvectors. The accuracy obtained from this data set was 98%. Showing that the measured joint angles and object variability were adequate for specific matching.

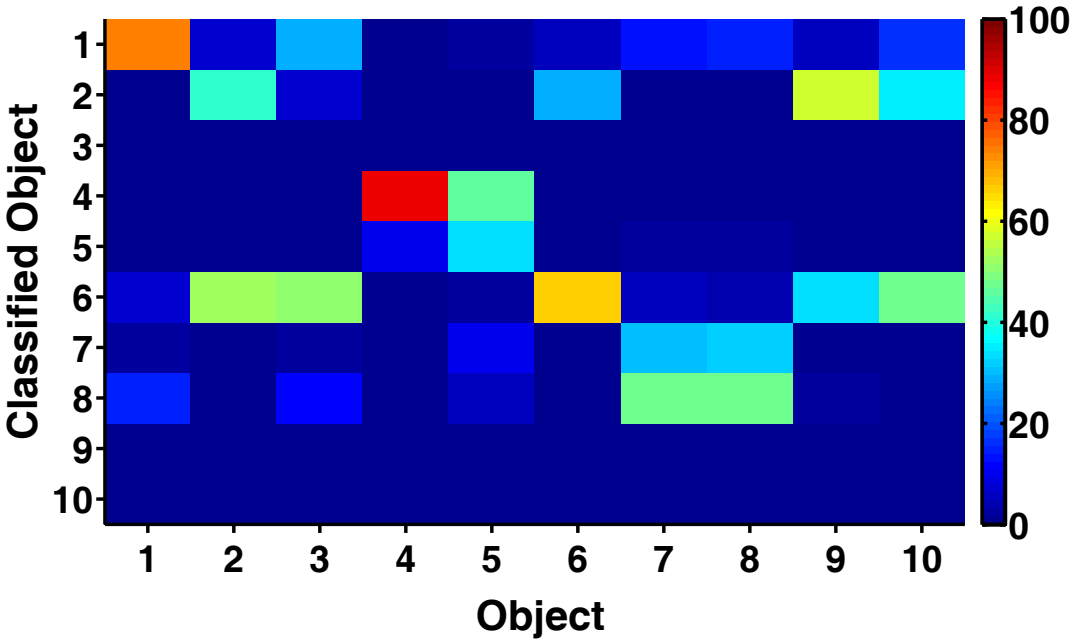

Figure 35. SVM Classification based on the first eigenvector.

The data used by the classifier was based on the joint angles reconstructed with the first eigenvector. The accuracy obtained was only 45% compared to 98% in the Figure 34.

As expected, accuracy of classification using all 20 eigenvectors by the SVM was 98% (Figure 34). Since there was no data reduction in this technique, this is merely a validation of the classifier and the methods used to produce the joint angle data sets. A similar method can be used to look at the accuracy of classification from all 20 DoFs projected through the first eigenvector (Figure 35). The accuracy of this method was 45%. A comparison of classification accuracy as a function of number of eigenvectors used can be seen in Figure 36. In this Figure two components have been combined. Object classification was completed using different data subsets as well as differing numbers of eigenvectors. It can be seen that the best classification was obtained using data taken from just before the object was touched (green), and that this curve plateaus after just five eigenvectors.

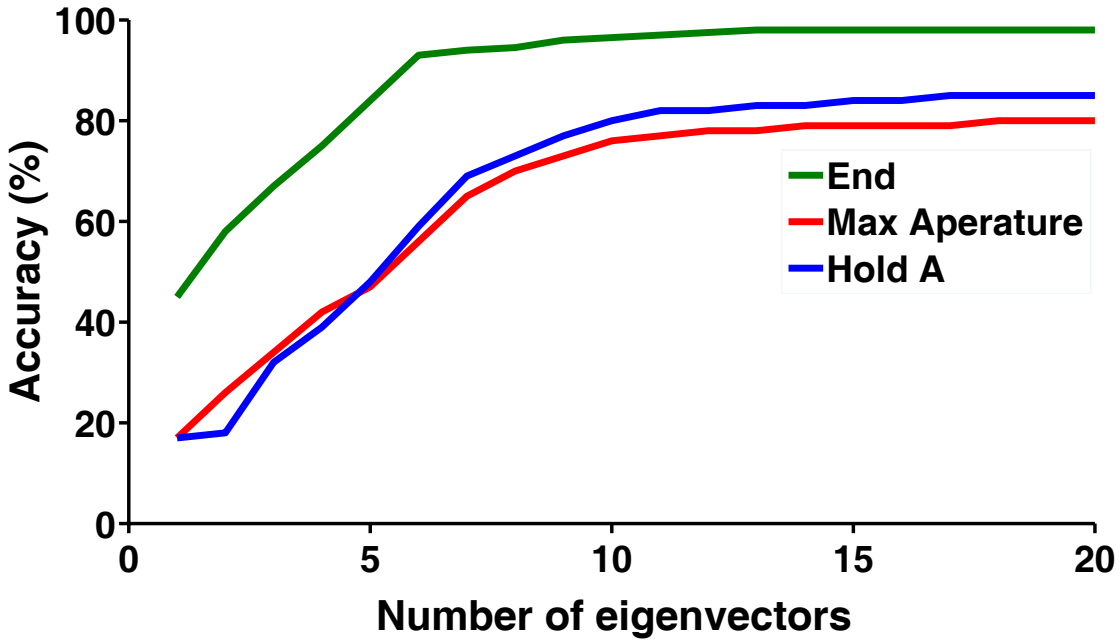

Figure 36. Object classification from eigenvectors.

On the y-axis is the percent accuracy from the SVM for classifying which object was being grasped based on joint angle data. The x – axis shows the number of eigenvectors used to create the joint angle data for object classification. The green line shows data used from only the end of movement, the blue line shows data used from only the beginning of movement, and the red line shows joint angle data from only the middle (Max Aperture) portion of the movement.

The two topics highlighted in this section detail the data selection, and the "necessary" number of eigenvectors required to accurately describe the variance in the original data set. Interestingly, two different results were obtained concerning the number of eigenvectors used. The results obtained from object classification showed that the first five eigenvectors were required to accurately classify the object grasped. The generalization of data subsets analysis showed that seven eigenvectors are necessary to describe 85% of the variance in the original joint angle data. Even though previous researchers have used SVM to justify the number of reduced dimensions necessary [79] we have adopted seven eigenvectors for the current work.

The cut off of 85% of the variance captured was criteria used by previous researchers [35, 46, 47], and the variance of joint angle data explained is more critical to the current work than object classification.

3.4.2 Postural Synergies

In the previous section data were presented showing correlation between joint angles during grasping (Figures 28 – 30). The results suggest that the "functional DoFs" are fewer than those determined anatomically. PCA was used to investigate the dimensionality reduction, and determine the DoFs necessary to describe the majority of movement variation in this reach-to-grasp task.

The data used in PCA were the joint angle data calculated at three different time points in each trial based on the results presented in section 3.3.2. Figure 37 illustrates these time points for a single joint (MCP 2 Flexion Joint) during all trials recorded from that joint in a single session across all objects. The three sections of the trial are the start, max aperture, and end grasp phases. In this way each trial contributed three observations for each joint. There was no further averaging of observation by target presentation in this analysis. This type of data structure provides a large data set that generalizes well to the entire movement.

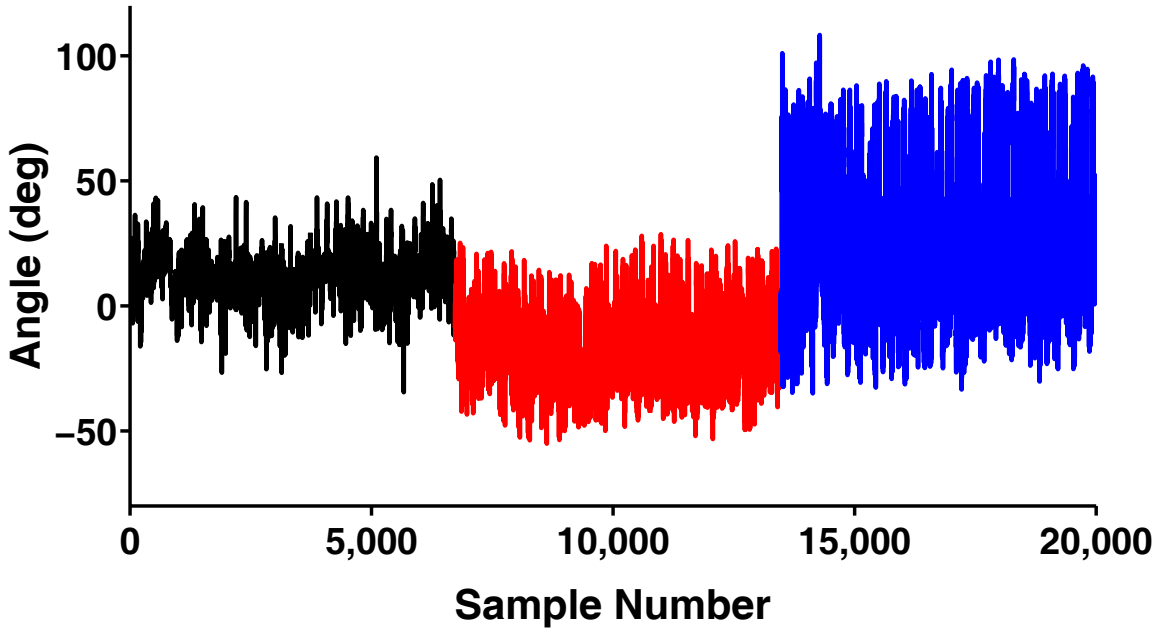

Figure 37. Angle data used in PCA.

Data from a single session used in PCA for the MCP2 Flexion/Extension degree of freedom. The y-axis shows the joint angle, and the x-axis is the sample number. The black portion of the graph is joint angle data taken from the beginning (End of Hold A) of the trial, the red portion of data is from the middle (Maximum Aperture) portion of the move, and the blue data points are from the end (Start of Hold B) portion of the trial. These represent non-contiguous data points throughout many different trials across all objects.

An identical data vector (as shown in Figure 37) was made for each joint. This expanded data vector was created from 317 sessions and included 96,685 trials. Principal component analysis was performed, for both monkey V and monkey B, on this joint angle data matrix (for details on applying PCA to grasping data see section 3.2.1). Figure 38 shows the percentage of joint angle variance explained by each eigenvector.

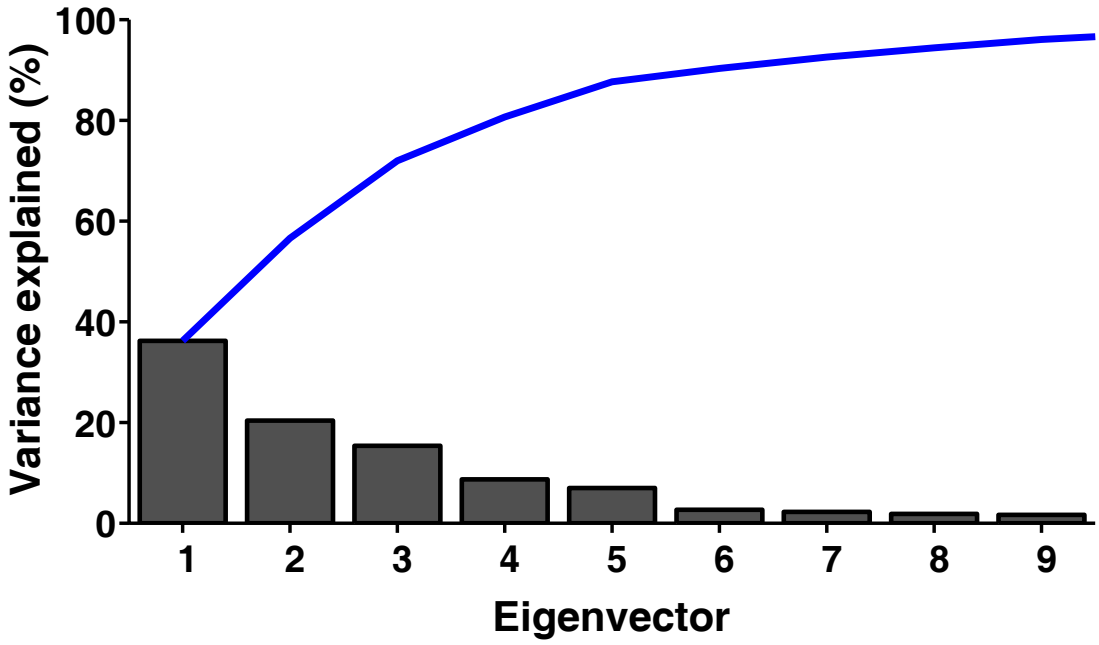

Figure 38. Joint angle variance explained from first 9 eigenvectors.

The y-axis is the percent of joint angle variance explained and the x-axis shows the number of eigenvectors added. The smooth blue curve in the plot represents the cumulative sum of the variance explained throughout the addition of orthogonal eigenvectors. The 85% variance explained threshold is crossed by adding the 7th eigenvector. Therefore at least seven eigenvectors are necessary to describe greater than 85% of the variance in joint angle data.

For both subjects it was necessary to include the first seven eigenvectors to account for at least 85% of the variance in the data. This high number of eigenvectors is in stark contrast to the two eigenvectors used to account for a similar amount of variance as in the Santello study [35]. This contrast can be accounted for by design differences between the two studies. One reason could be that wider ranges of grasping postures were used than those in the earlier psychophysics studies. Another is that the trial-to-trial variability in this data set is much higher than in the previous work. The number of DoFs measured in the current study is much higher (23) than in the previous work (15). The different DoFs between the two studies are the abduction / adduction movements of the fingers.

In order to visualize hand shape features corresponding to higher order eigenvectors, a correlation analysis was performed between actual and reconstructed angle data grouped by joint across fingers (Figure 39). The overall hand reconstruction correlation is shown as an average, the purple dashed curve. This line shows that in order to obtain a correlation coefficient of 0.85 seven eigenvectors are necessary, similar to the earlier analysis. The other curves in Figure 39 represent the grouped joint correlations.

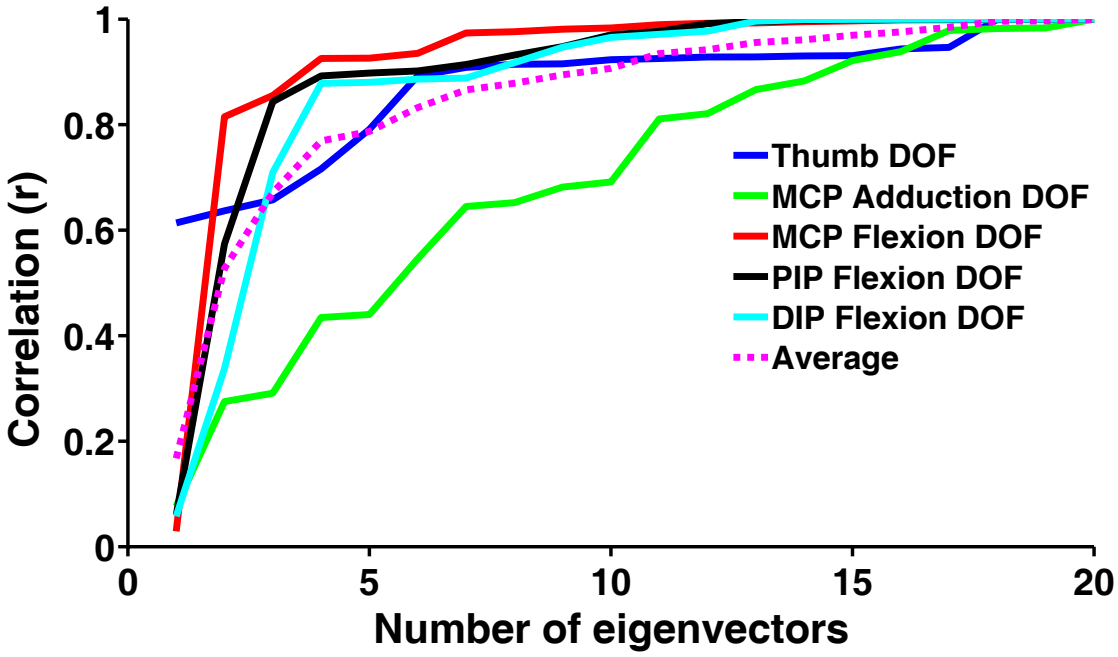

Figure 39. Correlation between actual and reconstructed joint angle data.

The y-axis is the correlation coefficients between actual and eigenvector reconstructed joint angle data. The x-axis shows the number of eigenvectors used during the projection. There are six different curves on this plot. All of which converge at an r-value of 1 when using 20 eigenvectors. The dashed line is the overall correlation using all joints for comparison, and all joints for projection. The blue curve is the correlation data obtained from using only the Thumb DoFs for projection and comparison. The green is the MCP abduction/adduction DoFs, red is the MCP flexion/extension DoFs, black is the PIP DoFs, and the light blue is the DIP DoFs. This separated correlation plot shows that the variability accounted for by adding eigenvectors beyond two or three is mainly capturing the variability of the MCP abduction/adduction DoFs.

The plot of reconstruction correlation against the number of eigenvectors shows which features of the grouped data are captured by the different eigenvectors. The only joint group that can be predicted by the 1st eigenvector corresponds to the thumb, as it gives a reconstruction match of 64%. Similarly the correlation for MCP Flexion and PIP is governed by the 2nd eigenvector, while DIP flexion requires 2nd and 3rd eigenvectors.

In contrast to the groups of joints well represented in the early eigenvectors, dimensionality reduction does not apply well to finger adduction. This feature does not correlate with the other features of hand shape in a consistent manner. This might be expected for the kind of precision expected in the “least automatic” movements of the hand indicative of the flexibility needed for adapting the hand to fine features of object shape. Finger adduction is characteristic of the human hand and is a feature of hand cupping thought to be essential in human evolution toward tool use [16].

Using the first three eigenvectors for reconstruction the correlation for the thumb DoFs is 0.64, the MCP Flexion DoFs are 0.83, the PIP DoFs are 0.82, the DIP DoFs are 0.7, and the MCP Abduction DoFs are 0.29. This analysis shows that a major difference between the number of eigenvectors necessary to describe a large portion of the variance in hand grasping data between the current and previous studies can be accounted for by a difference in the recorded DoFs. These DoFs appear to be specifically the abduction/adduction joints of the fingers. Suggesting that if a control system is to be created for a hand that does not have abduction/adduction finger DoFs, or the experimenter does not regard these DoFs as important,

accurate hand reconstruction may be accomplished using the first three to four eigenvectors instead of the first seven.

3.5 DISCUSSION

Monkeys' move their hand in a coordinated fashion throughout a reach-to-grasp behavior that closely approximates that of humans. These complex hand shapes were investigated by creating an object set, optimized by a cost function that sampled a wide range of the possible joint angle space. In order to investigate the complex coordination of many joints we performed a linear dimensionality reduction technique (PCA) to the hand shape kinematics. This technique produced a reduced set of grasping patterns (synergies / eigenvectors) that accounted for much of the variability in the kinematic data. The 1st eigenvector corresponded to a general opening and closing of the hand, which included much of the thumb variability. Movement along the 2nd and 3rd and 4th eigenvectors were a complex relationship between the DIP, PIP and MCP abduction joints of the fingers.

Many methods exist to validate the number of eigenvectors required to adequately describe a data set. One such method is to plot the sum of the variance accounted for against an accumulating number of eigenvectors (Figure 38) and simply pick the asymptote on the curve. As was true with similar data sets [1, 35, 46, 47], this variance explained curve had no definable asymptote. In light of this, we adopted three different approaches to determine the appropriate number of synergies.

With similar data sets researchers have chosen the number of eigenvectors required to explain 85% of the variance in the data. In our study we required seven eigenvectors to describe 85% of the variance in hand shape. A second method was to apply a linear classifier (support vector machine (SVM)) to pick which object was grasped based on a set of reconstructed joint angles using a differing number of eigenvectors. This analysis showed that eight eigenvectors are necessary to predict the objects 85% of the time from joint angles, and also showed that a considerable amount of information that allows for object differentiation is present very early in the reach.

A third analysis looked at what was gained by adding each additional eigenvector, in terms of hand shape reconstruction accuracy. In this investigation we separated the joints based on physiologic groupings. For instance, all the thumb joints were relegated to one group, while another group consisted of the MCP flexion joints of the fingers, a third included the PIP joints, a fourth the DIP joints, and the final grouping contained the MCP abduction joints of the fingers. This analysis showed that only a few synergies (~4) are necessary to capture the variability of many joints, and the majority of variability accounted for by higher-order eigenvectors occurs about the MCP abduction joints of the fingers.

4.0 CORRELATION BETWEEN SPIKING ACTIVITY IN MOTOR CORTEX AND WRIST DOFS

The correlation between motor cortical spiking activity and wrist movement is important in both science and medicine. Neural controlled motor restorative devices are rapidly growing in popularity, and becoming increasingly useful for patients with every successful new application. A limitation of the current technology is the number of simultaneously controlled degrees DoFs. The most advanced neural controlled robotic arm utilizes four simultaneously guided DoFs; x, y, z of the endpoint of the wrist, and 1-D gripper signal [71]. Ability to control the three dimensions of wrist orientation with a neural signal would be a major advancement.

In this chapter we present the relationship between motor cortical firing and wrist orientation. We start with a section on wrist kinematics and show that the relationship among wrist DoFs change as a subject learns the reach-to-grasp task. This section is followed by an analysis of the relationship between motor cortical firing and individual, and then multiple, wrist DoFs. The last section in this chapter highlights a prediction equation that uses firing rates from populations of motor cortical cells to simultaneously predict the three DoFs of wrist orientation.

4.1 WRISTDATA OVERVIEW

Joint angles corresponding to the wrist have been separated from the finger data based on the initial findings from the correlation analysis across joints. Figure 24 shows little correlation amongst wrist DoFs. As mentioned in earlier chapters, this may be a phenomenon based on physiology or merely a result of the experimental design.

The wrist DoFs were isolated in the design of this experiment by presenting the same object at the same x, y, z end-point with multiple orientations. For ease of notation, we call a particular object/orientation combination a *presentation*. The orientation positions (shown in Table 2) were chosen to elicit different wrist postures from the monkey while maintaining a consistent grasp. Because some objects have rotational symmetry, not all objects were presented at each orientation: in particular, Presentations 1 and 3 from Table 2 were not performed for the Button, Small and Large Cones. A session constituted five successful completions of each presentation, yielding a total of 320 successful reach-to-grasp trials per session.

Table 2. Object names and orientations.

The seven presentations listed in the right column were used for Objects 2, 3, 4, 5, 7, 8. Objects 1,9,10 are rotationally symmetric, so we did not combine them with orientations 1 and 3.

List of objects and presentations used in the task

Objects	Presentations
1.) Button	1.) -45 Degrees Rotation
2.) Small Handle	2.) Horizontal Rotation
3.) Large Hande	3.) 45 Degrees Rotation
4.) Small Rectangle	4.) 45 Degrees Flexion
5.) Large Rectangle	5.) 45 Degrees Extension
6.) Disk	6.) 45 Degrees Abduction
7.) Small Precision	7.) 45 Degrees Adduction
8.) Large Precision	
9.) Small Cone	
10.) Large Cone	

The presentations listed in Table 2 are represented graphically in Figure 40, which shows the “small handle” object from the monkey perspective. The object is highlighted by red.

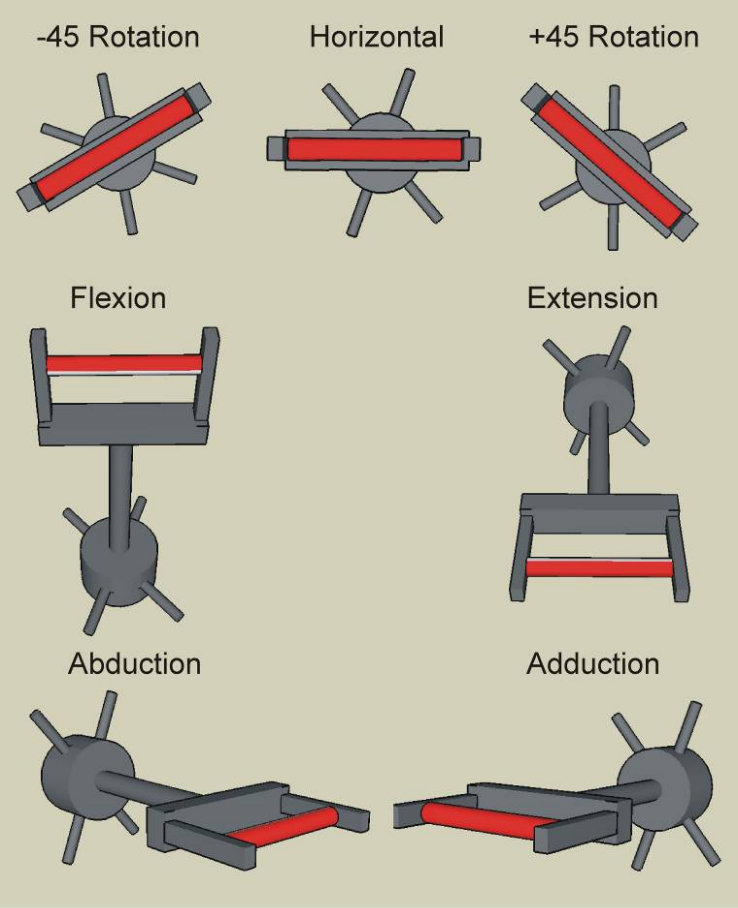

Figure 40. Object orientations.

This is an illustration of the object orientations listed in Table 2 using the small handle for demonstration. The orientations are named with respect to the intended monkey wrist movement. For example the flexion orientation is extension of the object by the robot that requires wrist flexion for a reward.

The different object orientations force the subject to use nearly the entire physiologic range of wrist motion. We measured the physiologic range of the wrist DoFs with a goniometer. This experiment entailed two researchers collecting goniometer data from a monkey. The goniometer data was recorded at the maximum and minimum of each wrist DoF. These data were compared to joint angle data collected from multiple sessions using the 3-D motion tracking system (Figure 41). This analysis shows that orientations selected cause the monkey to

use almost the entire range of wrist joint movement. The one DoF that does not come close to the joint maximum is the rotation. The extreme of supination is when the palm is pointing up. We could not track markers in these reverse postures.

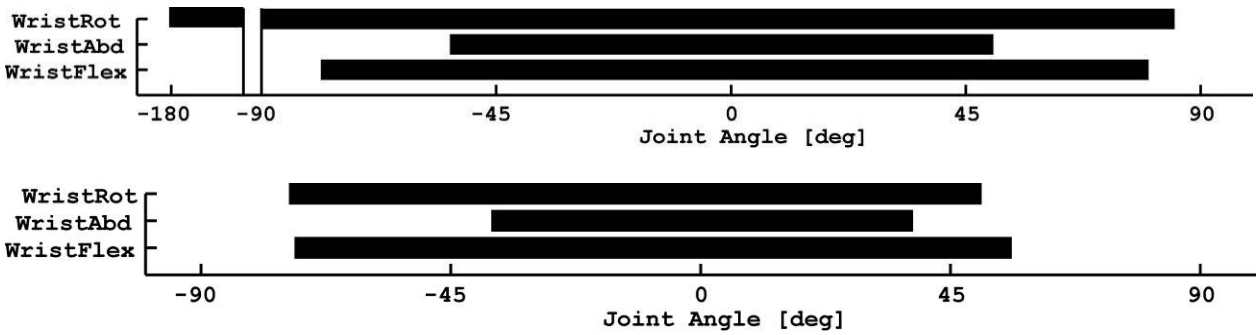

Figure 41. Possible wrist DoFs range and actual.

Top row shows the three wrist DoFs against the physiologic range of that joint. The joint range was elicited from the monkey using passive movement and a goniometer for measurement. The bottom row shows the active ranges of joint angle data for the wrist DoFs across all object presentations.

4.1.1 Wrist Kinematics – Isolated Degrees of Freedom

In earlier chapters the finger kinematic data were detailed with a focus on dimensionality reduction. Wrist kinematics are separated from the dimensionality reduction of finger kinematics for two reasons. First, the wrist has few DoFs. There is likely little gained by describing these DoFs with fewer dimensions. In this study the wrist is considered to have three DoFs: yaw, pitch and role, corresponding to abduction, flexion, and rotation, respectively. While the physiologic location of the rotational DoF is at the elbow, the end effect is rotation of the wrist/hand; for this reason, we have considered this a wrist DoF. The second reason for separating the wrist from

hand DoFs is that the analysis of hand kinematics focuses on hand shape, which is not necessarily changed with wrist movement.

A critical feature to the concept of preshaping is that the hand is continuously guided in a smooth fashion from a beginning to an end posture. This smooth movement occurs throughout a reach that progresses to a final posture that closely approximates the desired object [36, 38, and 39]. It is possible that the monkey shows continuously progressive movements of the fingers that match the desired object, but make sharp transitions with regards to wrist movement. It can be seen from Figures 42 and 43 that the wrist DoFs show similar characteristics already highlighted in the finger kinematics section.

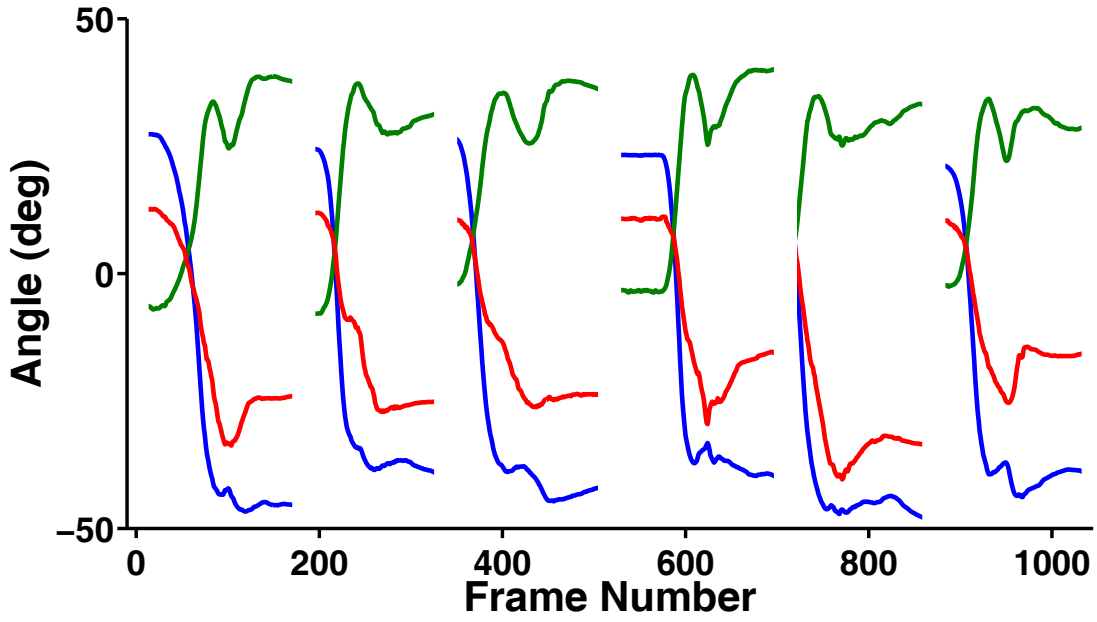

Figure 42. Wrist angles over consecutive trials.

The Angle tracings show three wrist DoFs recorded simultaneously over six presentations of the small handle in the same orientation. The frame number refers to a kinematic data sample. Each frame number is separated by 5 ms. The six trials have been spliced together with the end of one trial and the beginning of another separated by a blank space.

The wrist angle tracings shown in Figure 42 illustrate the wrist DoFs over six consecutive trials. Over many movements the monkeys display certain angle and velocity characteristics. The monkey has a starting posture that is slightly flexed, adducted and generally has a neutral rotational component. The wrist progresses from this starting posture to a final posture through a section that shows a rapid change in angle. It can also be seen from these joint angle plots that the variance in wrist orientation is not uniform across different regions of the movement. The largest amount of variance in both wrist angle and hand shape, shown earlier, occurs during the grasping phase of the task.

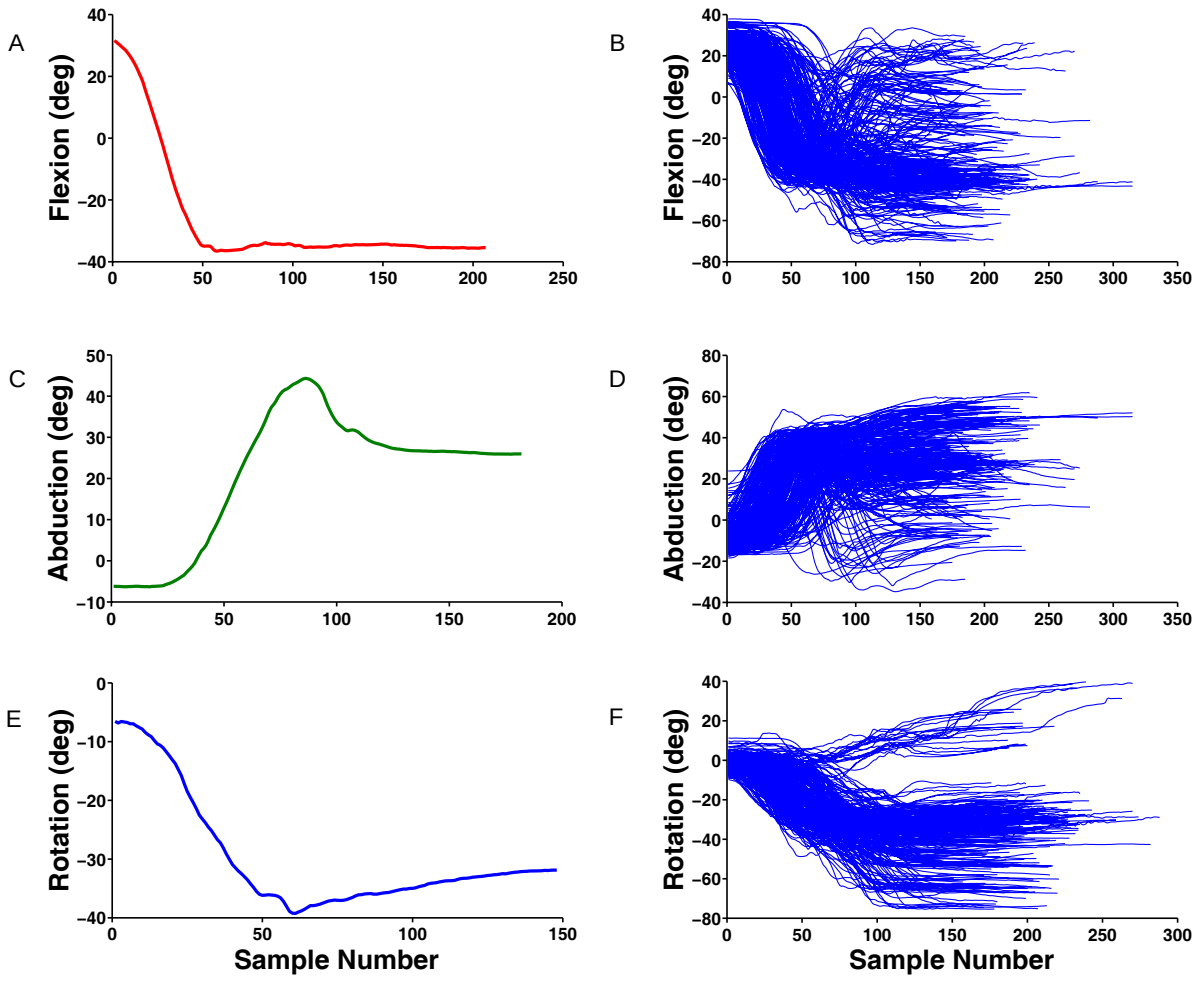

Figure 43. Wrist DoFs - single and multiple presentations.

Three rows starting from the top represent flexion, adduction and rotation DoFs of the wrist. The left column of Figures shows individual presentations, and the right column shows the corresponding wrist DoFs for all the trials in a session. The plots are aligned at the end of Hold A.

The monkeys display characteristic joint angular velocity profiles. In Figure 44, many joint angular velocity tracings from 100 sessions, across all objects, have been overlaid onto the same plot. All trials were reconfigured to have a uniform length of 100 samples. The average length of the trajectories was 203 samples ± 42 (mean ± SD). The trials have been aligned on the

maximum or minimum velocity for best alignment. The trials were made uniform before the alignment procedure to preserve the maximum or minimum velocity relationship to the start and end of the trials. Positive velocities for flexion and abduction occur when the joint travels in the named direction. For example, a negative wrist flexion velocity occurs when the monkey extends the wrist. Wrist rotation has been defined so that positive denotes pronation and negative denotes supination. The aligned joint angular velocity profiles show that the wrist DoFs have a characteristic joint angular velocity profile across all objects. As shown in the joint angle analysis (Figure 44), the majority of wrist angular velocity variability occurs in the second phase of the reach when the hand is close to the object.

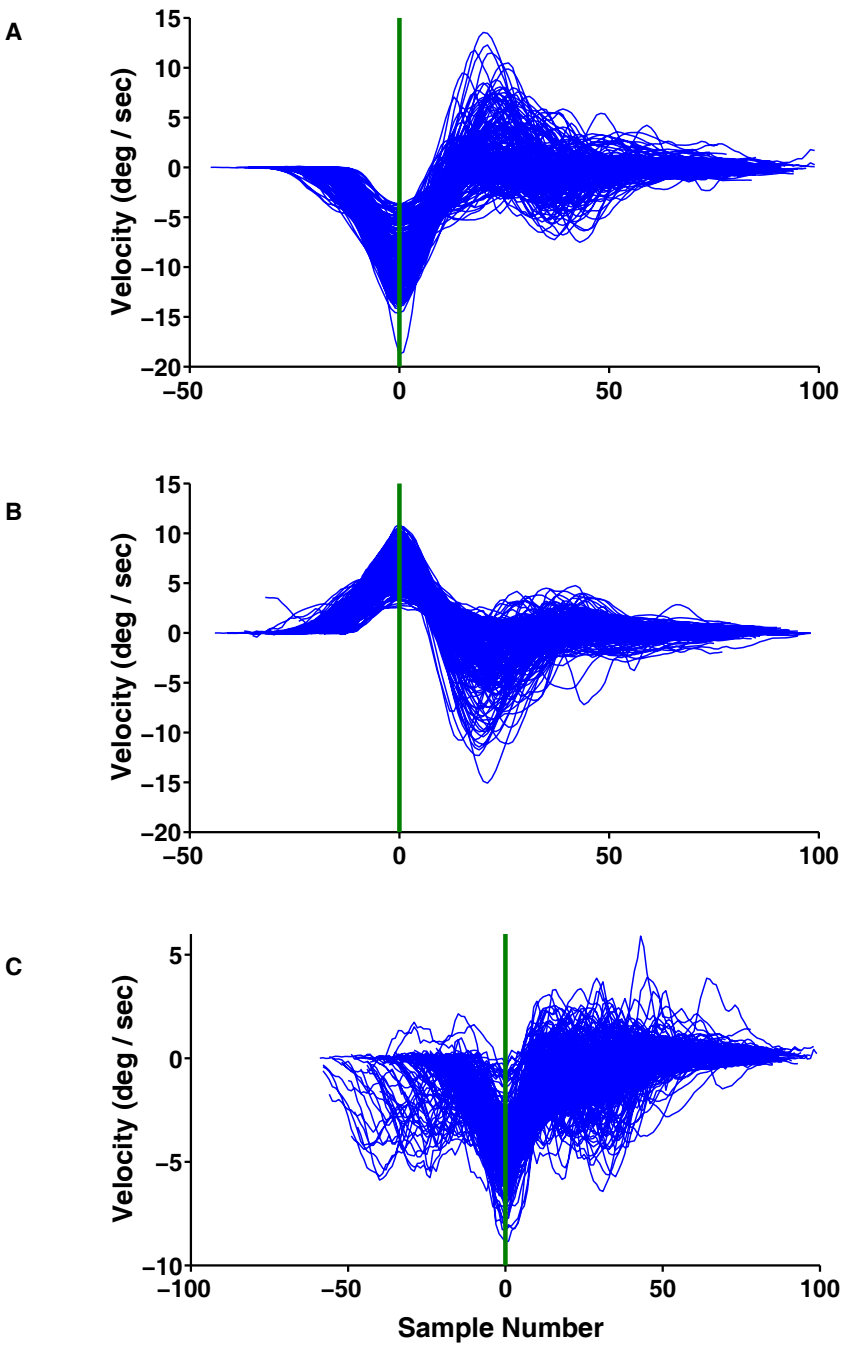

Figure 44. Aligned wrist angular velocities over many trials.

The Figures A, B, and C show wrist angular velocity plots for the flexion, abduction and rotational DoFs, respectively. The flexion and rotational DoFs plots are aligned by the min (most negative) angular velocity. The abduction DoFs plot is aligned by the max velocity.

The interaction of wrist joint angular velocity and joint angle is shown in Figure 45. The generalized diamond shape in this Figure shows that maximum velocity is achieved in the middle of the joint range.

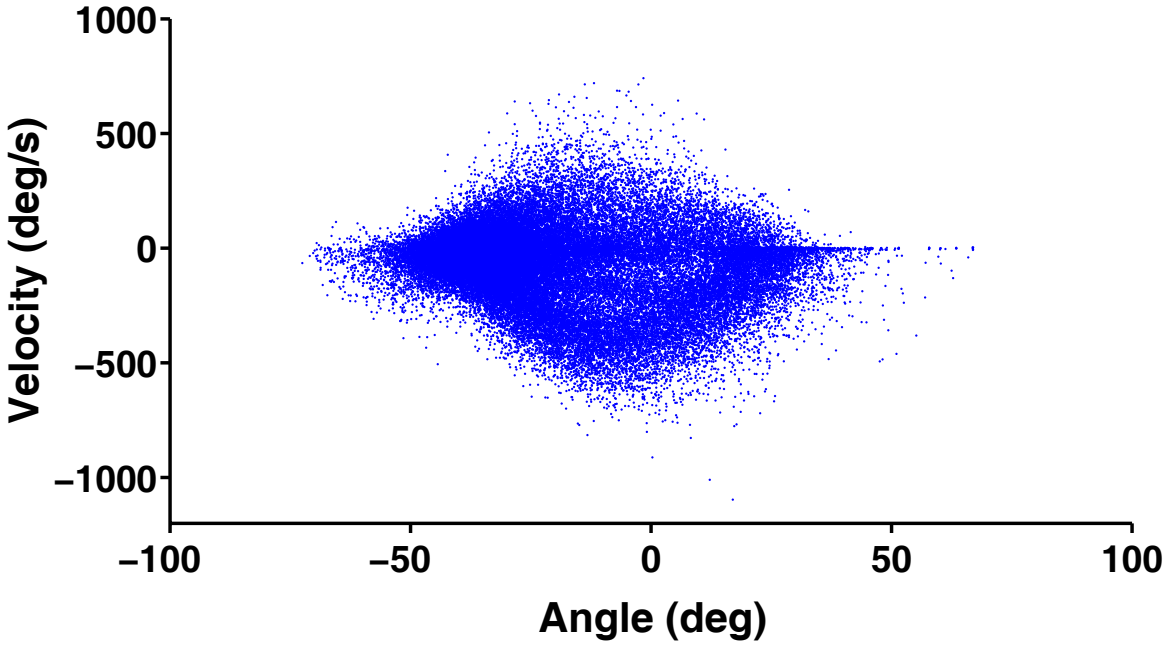

Figure 45. Wrist flexion joint angular velocity vs. joint angle.

This Figure shows the wrist joint angle plotted against the wrist joint angular velocity.

4.1.2 Wrist Kinematics – Joint Correlations

The previous section focused on the wrist DoFs as isolated entities. This section will explore the correlations amongst the wrist DoFs.

The correlation analysis in Figure 29, section 3.3.1 shows that the wrist DoFs are not highly correlated with one another. The data used in this analysis was taken from the early training sessions for both monkeys, before neural data was recorded. We repeated this analysis for data taken in conjunction with neural data, when the monkeys are considered to be over-trained on the task. A three-dimensional plot was generated to show the wrist DoFs over these two periods of training (Figure 46). The early data is the first 30 days of training. The late training data was from the last 50 days of recording. Figures A and B show the post-training data in two different orientations: an orientation corresponding to the maximum distribution of data points (Figure A), and an orientation rotated 150 degrees around the upright axis of the plot, highlighting the minimal distribution of data points (Figure B). The combination of these Figures shows that a plane exists which describes a majority of the variance in wrist angle data. Similar plots (Figures D and C) have been generated for the early-training data, viewed from the same orientations. There are clear qualitative differences in the distributions of points in the two plots, indicating that training had a major effect on wrist DoFs correlations.

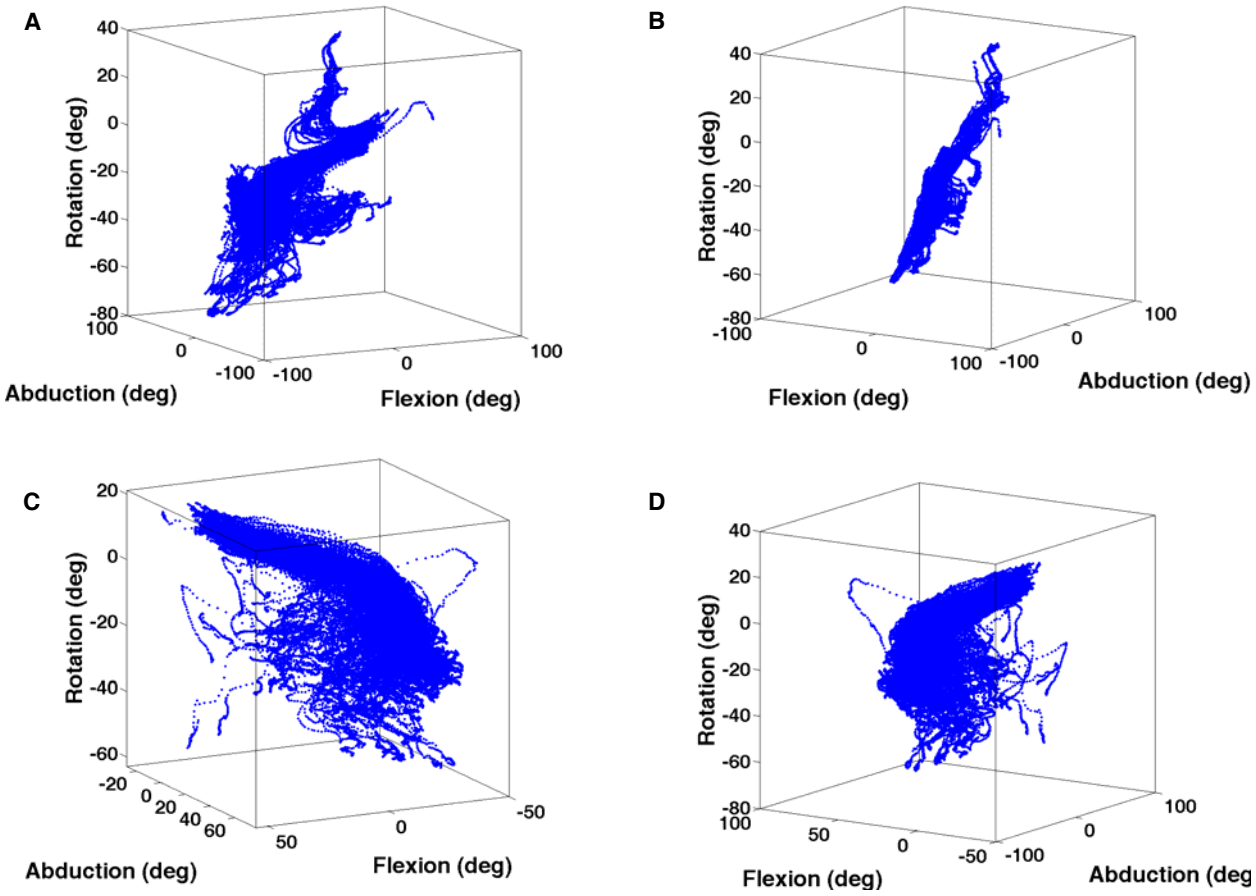

Figure 46. Wrist angle correlations as a function of training.

Plot a, b, c, and d show the three DoFs of wrist orientation plotted against one another in a 3 dimensional plot. Figure A and B show the maximum and minimum distribution for the data during the neural recording portion of the experiment. Figure B is 150-degree rotation around the upright axis. Figures C and D are similar to Figures A and B, except this data was taken from the first 30 days of training.

A joint-pair matrix was created for the wrist DoFs to calculate joint correlations. The wrist joint pairs are as follows: Flexion-Abduction, Flexion-Rotation, and Abduction-Rotation. For illustration purposes the joint-pair matrices for post-training data have been plotted in Figure 47. This Figure shows a strong negative correlation between the flexion and abduction DoFs, a

strong positive correlation between flexion and rotation DoFs, and a weak correlation between the abduction and rotation DoFs. These correlations are calculated across all presentations of all objects. The joint pair correlations (r) for the early and late training data have been displayed in Table 3. The early training trials are from the first 30 sessions of kinematic data recorded from monkey V and B. The Late Trials are data from the last 50 sessions from monkeys V and B. Between these two sets of data the monkeys had 212 training sessions (monkey V), and 134 training sessions (monkey B).

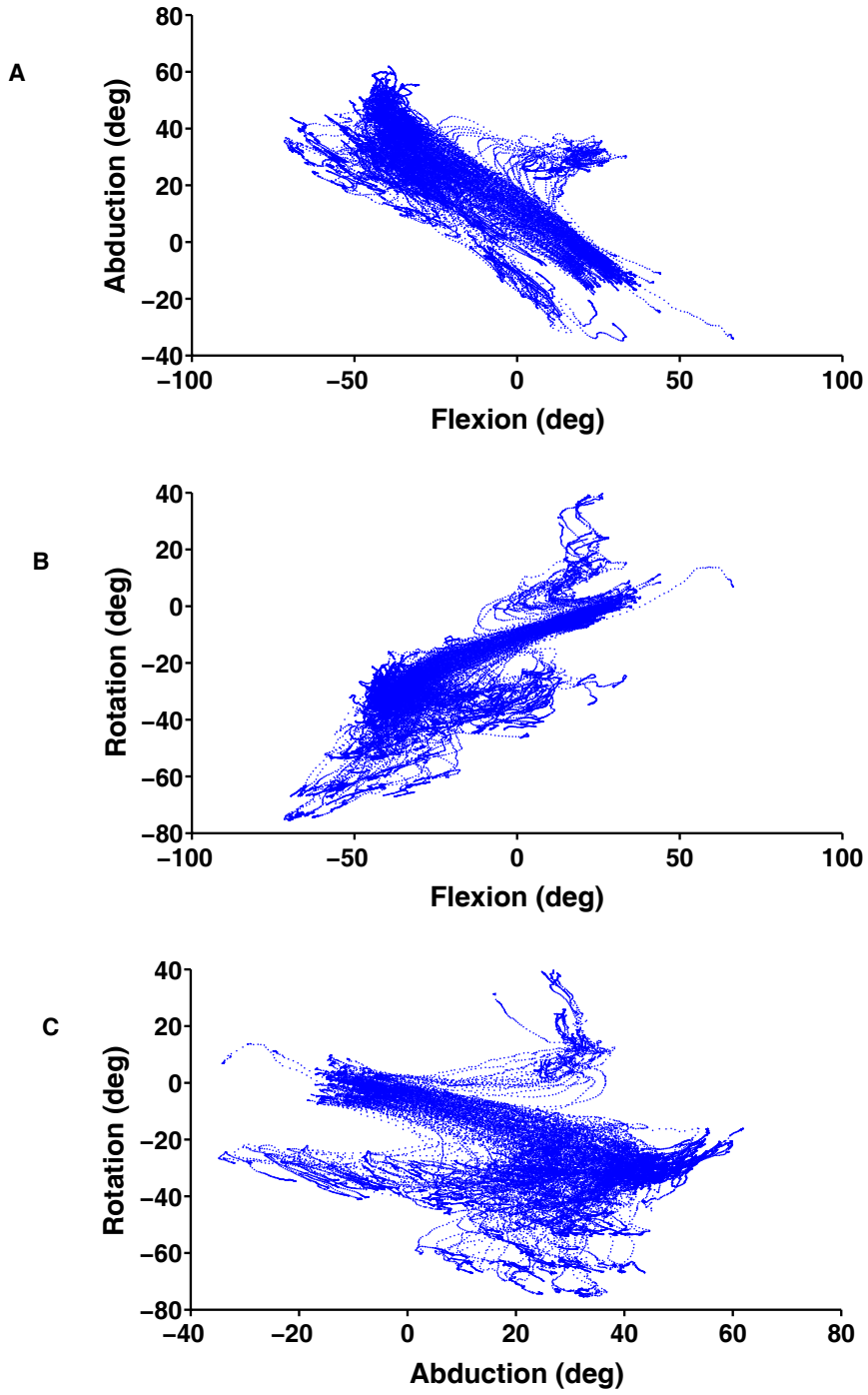

Figure 47. Wrist DoFs paired correlation.

Figure A shows Flexion vs. Abduction, B shows Flexion vs. Rotation and C shows Abduction vs. Rotation. The Figure panes are a visual representation to the joint pair correlations shown in Table 3.

Table 3. Wrist DoFs paired correlation. Early versus late training.

The early training trials show a correlation with similar orientation to the late trials; however the magnitudes are much less.

Paired DoFs	Early Training Trials	Late Trials
Flexion – Abduction	**- 0.42**	**- 0.78**
Flexion – Rotation	**0.36**	**0.80**
Abduction – Rotation	**-0.27**	**-0.34**

The progression of change in correlation across training days can be seen in Figure 48. This progression of correlation between wrist DoFs is consistent amongst the two monkeys studied. The correlation change is not associated with a similar change in success rate, movement time or total trial time, as all three of these variables were consistent throughout early and late training. For monkey V the placement of force sensors changed early in training, however the force sensor placement was consistent for monkey B. The only task related variable that appears related to the correlation change is the number of completed trials (Figure 49). This may be a strategy that the monkey adopted to reduce the overall energy expenditure per reward, allowing the animal to complete more trials without fatigue.

This data also suggests that the wrist DoFs are not naturally correlated: the correlation seen in the post-training plots is induced by the training. This is another reason to separate the wrist DoFs from the finger kinematic data; we are more interested in studying natural kinematic correlations than training-induced correlations.

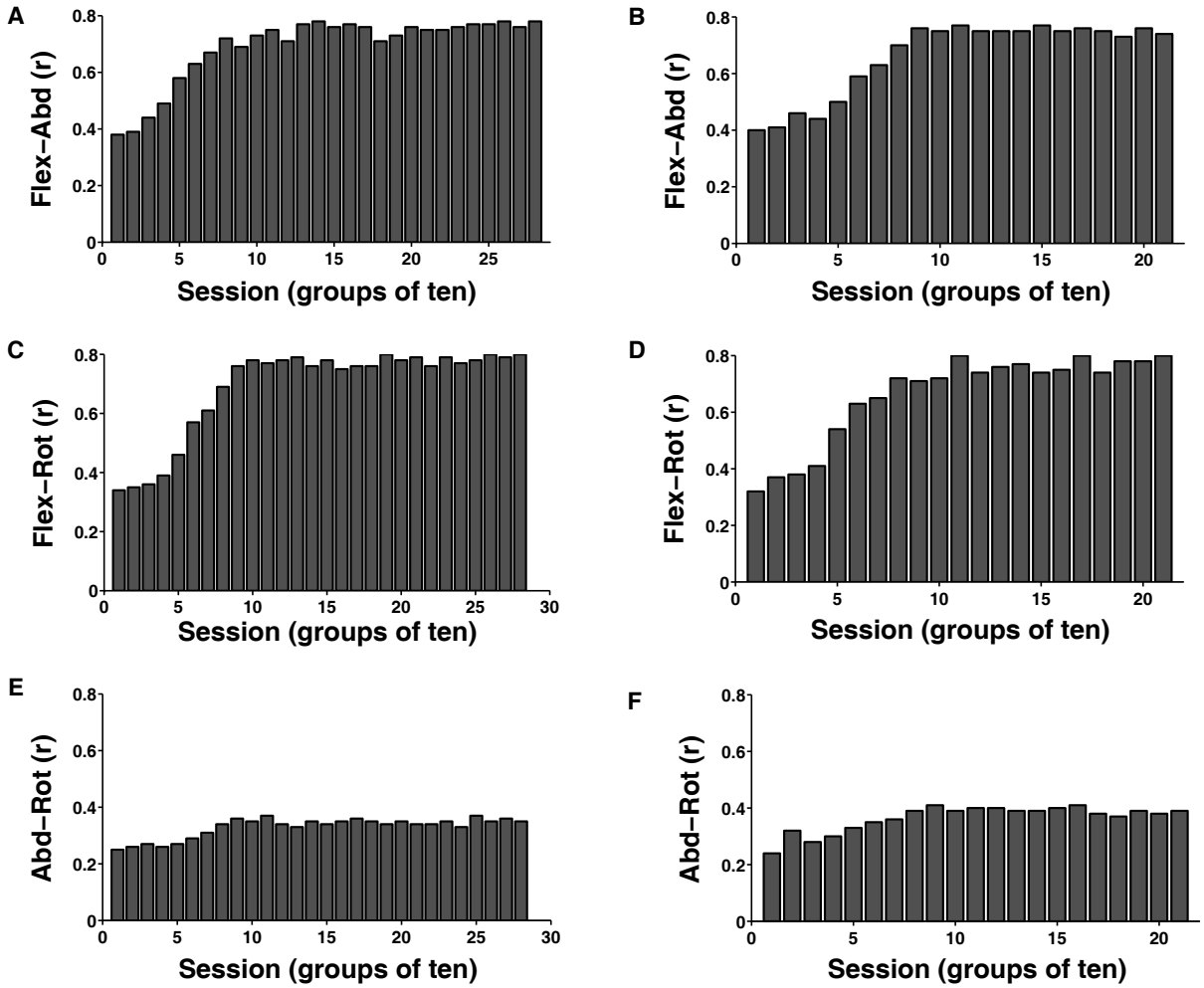

Figure 48. Wrist DoFs correlation over training sessions.

Plots A, C, and E are from monkey V. Plots B, D, and F are from monkey B data. Both monkeys show similar correlation throughout the early and late training. Note for consistency the r-values are reversed in A, B, E, and F.

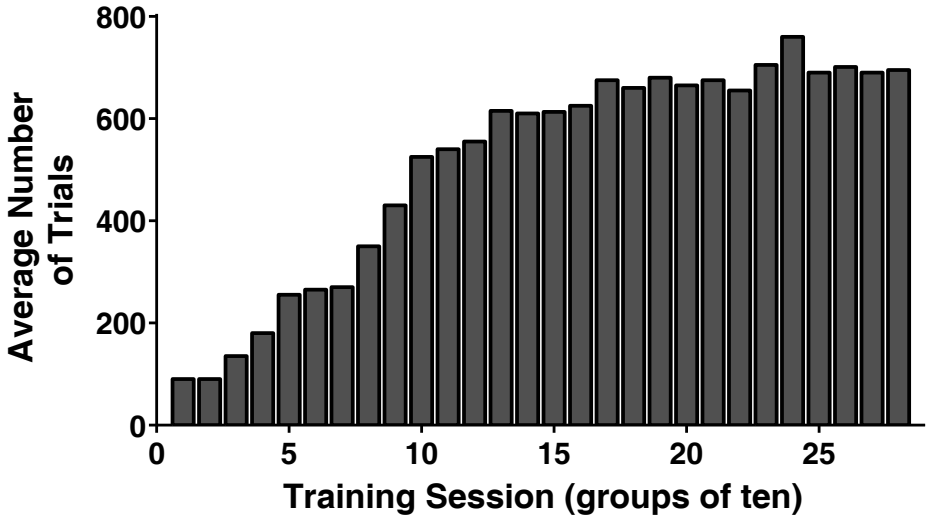

Figure 49. Number of trials completed per day.

This bar plot shows the average number of trials completed for monkeys V and B over the course of the experiment. Each training session on the x-axis corresponds to the average of ten sessions. monkey V had more training sessions than monkey B. The last seven values in this plot are averages from monkey V.

4.2 INDIVIDUAL DEGREE OF FREEDOM TUNING

The firing of a motor cortical cell has been shown to be correlated with many movement variables. In an early study, Evarts trained a monkey to flex its wrist against a load until the device hit a mechanical stop. He found that motor cortical cell firing was correlated with force, the change in force, and displacement of the wrist [80]. Humphrey later modified this paradigm and found that motor cortical cell activity was related to force, velocity, position and the change in force [81]. Later, Georgopoulos trained a monkey to move a manipulandum between a center target and eight peripheral targets (the center-out task). These studies showed that a population of motor cortical neurons was highly correlated to arm translational velocity [54, 55].

The relationship between motor cortical firing and wrist movements has been studied by a number of investigators [82]. Kakei et al. investigated if the primary cortex encoded low-level parameters like muscle force, or more abstract parameters like hand path. They found that both “muscles” and “movements” are strongly represented in M1. In a later study, authored by Wang et al., the researchers studied the motor cortical representation of both hand translation and rotation. In this study, single-unit activity was recorded from monkeys while they performed a "center-out with rotation" task. When reaching for a target, subjects had to match four separate kinematic parameters: three-dimensional location and one-dimensional orientation of the target. This study demonstrated that both hand translation and rotation could be decoded simultaneously from a population of motor cortical neurons [83].

In the following section we will explore the possibility that the firing rates of motor cortical cells are linearly correlated with individual, and multiple wrist DoFs during natural reach-to-grasping movements. It is of interest in this study to determine which wrist kinematic variables are best correlated to motor cortical firing so an efficient decoding algorithm may be constructed from natural neurophysiogical phenomena.

The cells selected for this analysis were those with an R^2 greater than 0.1 in a multivariate linear regression between averaged firing rate data over an entire trial and average wrist angles over an entire trial. These are the cells used in the decoding section (4.4). However, in order to conserve the dynamic relationship between firing and joint variables, the individual cell analysis is based on binned data.

4.2.1 Motor cortical spiking correlation between position and velocity variables

The position variable in this experiment is joint angle. An example of how a motor cortical cell varies with wrist angle is shown in Figure 50. Fractional interval rate calculation (detailed in Section 2.5.2) over 30ms bins were used to calculate the firing rate of a cell. This Figure shows a cell that increases firing with wrist extension and decreases firing with wrist flexion. A linear regression using this data returns an R^2 of 0.3.

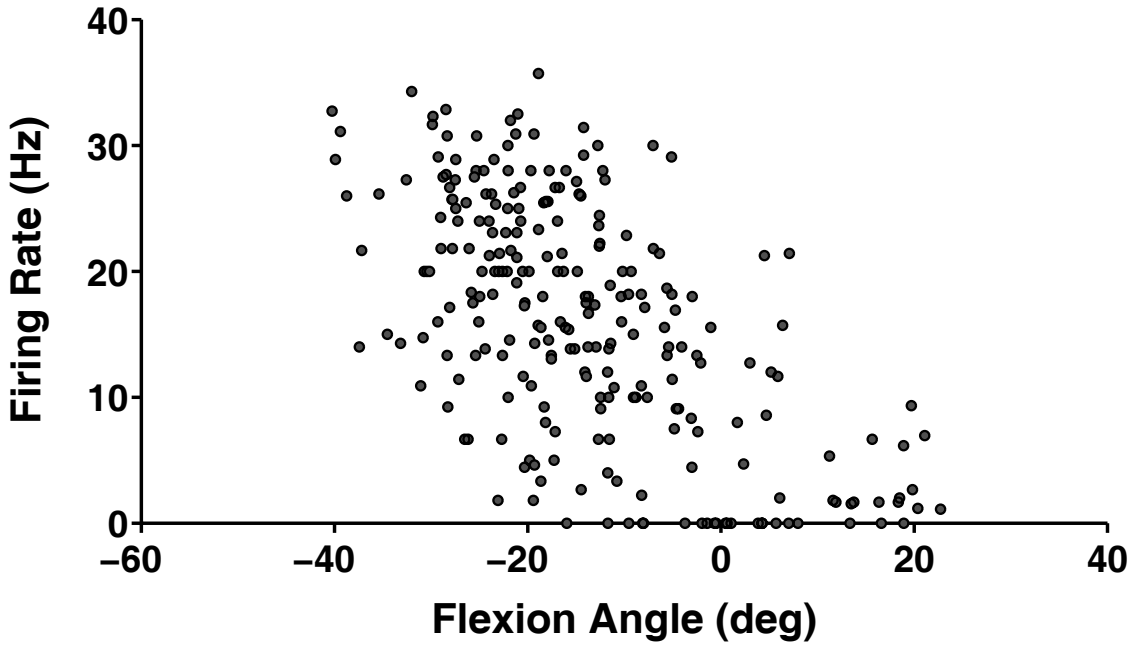

Figure 50. Motor cortical cell firing- wrist flexion angle.

Scatter plot of monkey V cell 2a session 483 firing as a function of wrist flexion angle. On the x-axis is wrist flexion angle and on the y-axis is the firing rate.

The velocity is the instantaneous joint angular velocity (deg/sec) calculated in 30ms bins from the position data. An example of the change in a motor cortical cell firing with respect to joint angular velocity is shown in Figure 51. The wrist DoF in this example is abduction. A

change in the direction of abduction is a positive velocity, while a change toward adduction is a negative velocity (R^2 0.44).

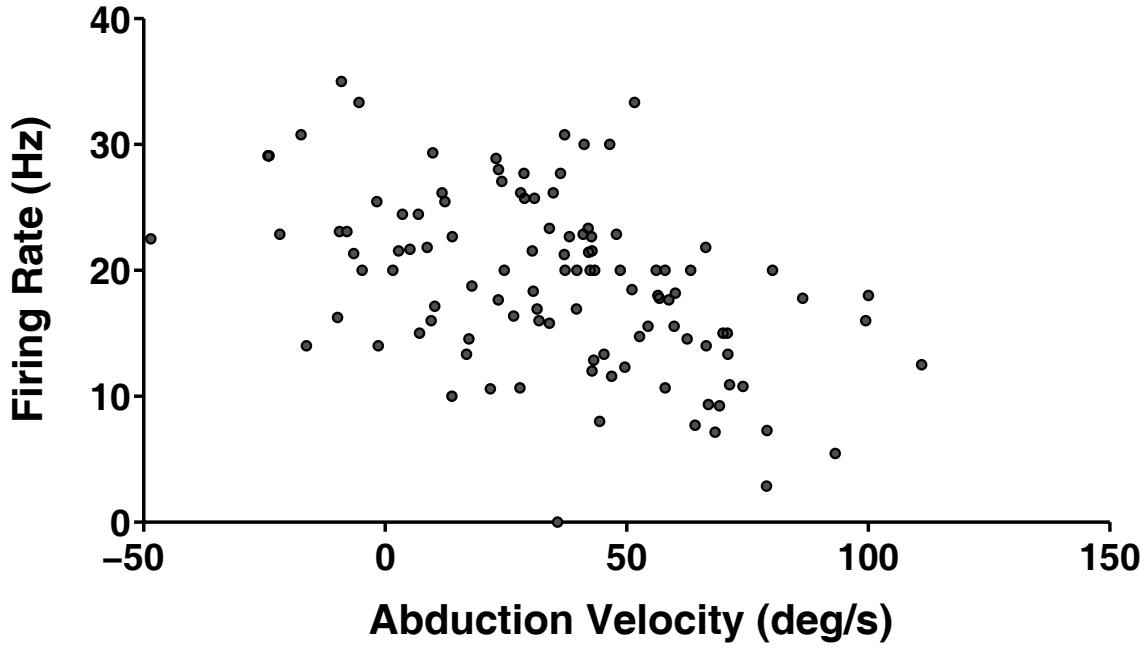

Figure 51. Motor cortical cell firing- with abduction velocity.

Scatter plot of Cell 5a from session 485 with respect to wrist abduction velocity.

A linear regression was used to calculate the correlation between firing rate and joint variables in the above Figures. The regression equation used was …

$$\vec{f} = b_0 + b_w \vec{Z}_w \tag{10}$$

where b is a vector of regression coefficients, $\vec{Z}$ is a vector of wrist angles or velocity, and $\vec{f}$ is a firing rate vector in spikes per second. The subscript $_w$ is changed depending on the wrist DoF in question (flexion, rotation, or abduction).

Equation 10 was used to calculate the correlation between cells firing rate and each wrist DoF for position and velocity. A comparison of the correlation coefficients obtained in these linear regressions can be seen in Figure 52. The blue line in this plot represents a unity line. If both variables are equally related to motor cortical cell firing this line will evenly split the distribution. In this plot the distribution of points around the unity line does not qualitatively give the impression that the population of cells is more correlated with wrist position or velocity.

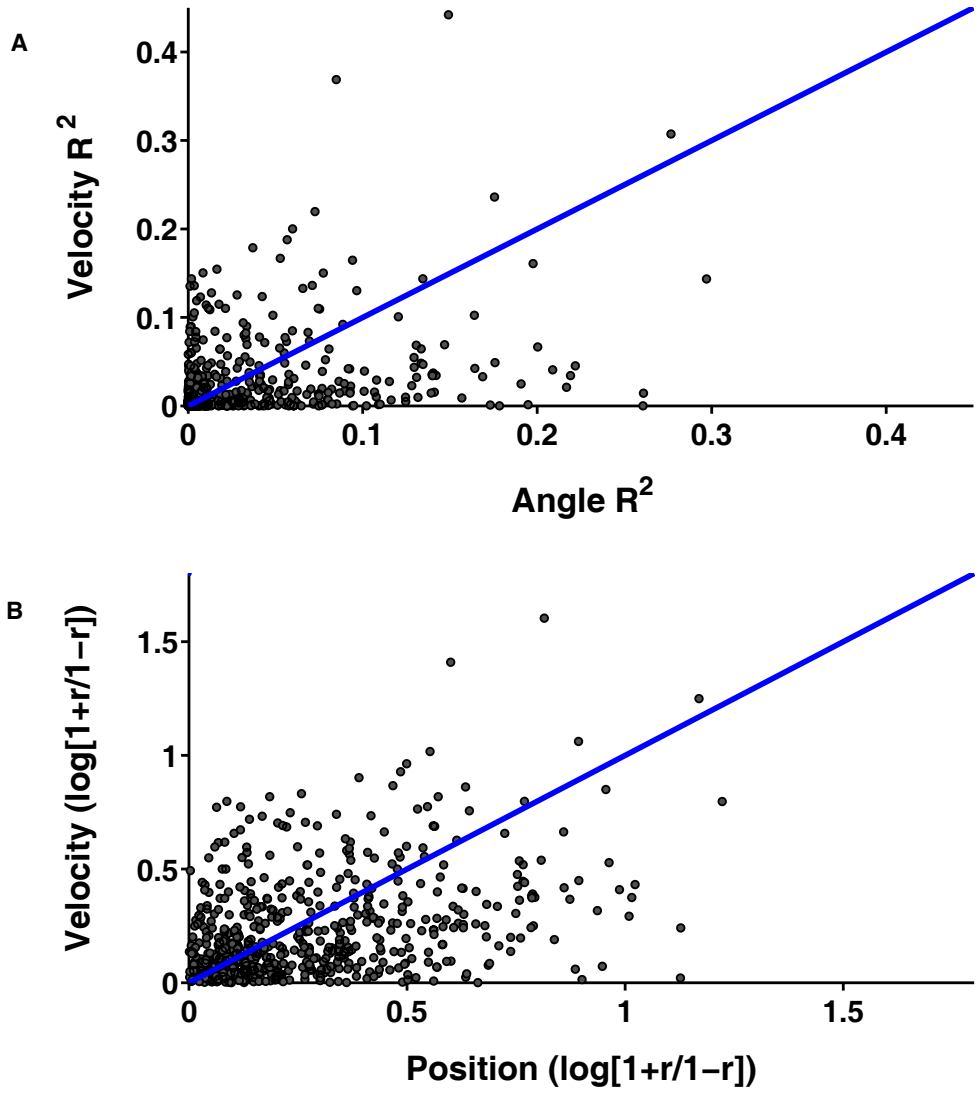

Figure 52. Angular velocity R^2 vs. angle R^2.

Each point represents a cells R^2 between joint angular velocity and joint angle for the three independent linear regressions. The blue line is a unity line.

The distribution of the difference in correlation coefficients between position and velocity is shown in Figure 53. The mean of these distributions is only slightly positive for the three wrist DoFs, slightly more for rotation. This minimal shift indicates that the neural population may be slightly more correlated with wrist angle; however this is not clear evidence.

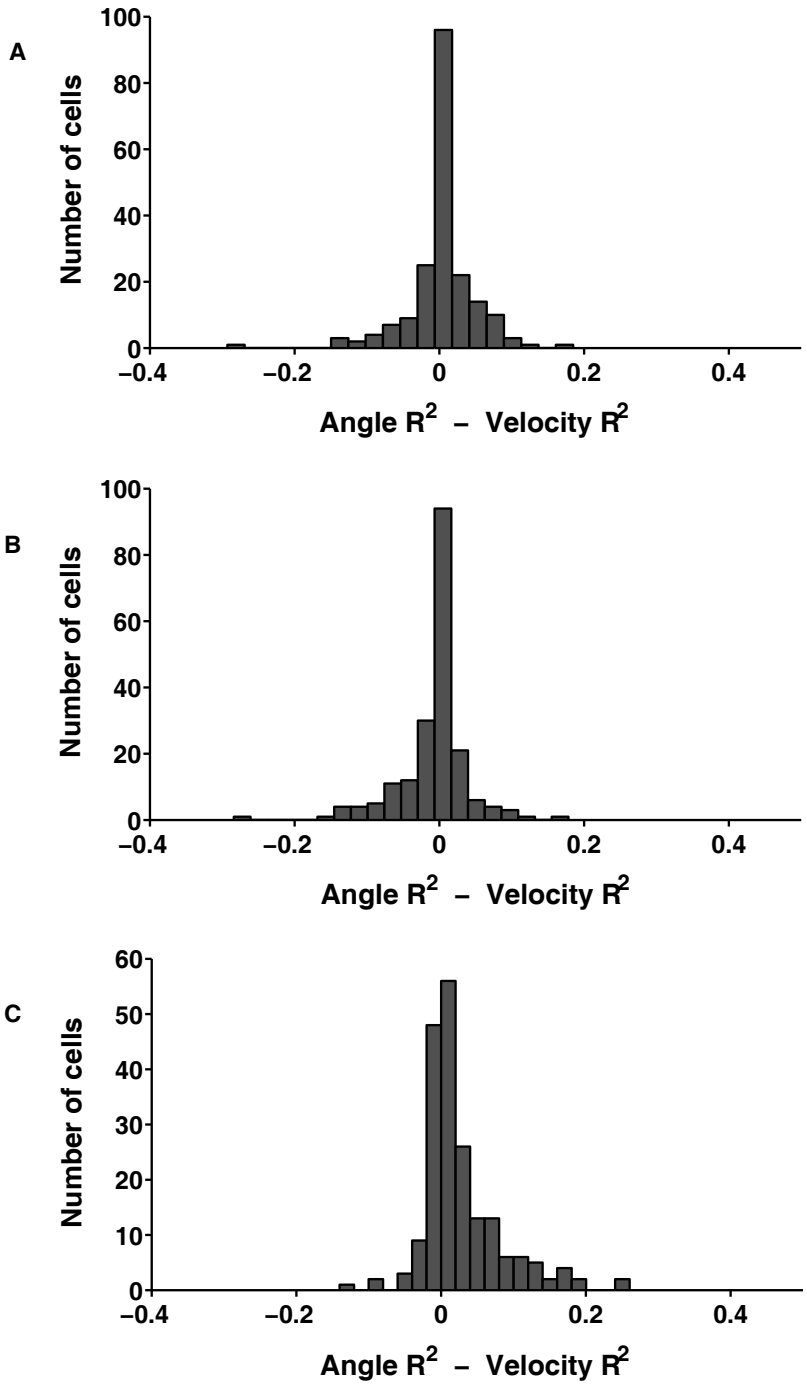

Figure 53. Position and velocity correlation difference histograms.

Plots A, B, and C show a distribution of the correlation difference for wrist flexion, abduction and rotation DoFs. The x-axis values in this Figure are created by subtracting the joint angular velocity R^2 from the joint angle R^2.

The correlation coefficients shown in this analysis were all calculated as independent linear regressions. It is possible that the addition of coefficients in a multiple linear regression will produce more definitive results.

4.3 MULTIPLE DEGREE OF FREEDOM TUNING

The previous sections have focused on motor cortical correlations with individual wrist DoFs utilizing Equation 10. The expansion of this single dimensional linear regression to a multivariate linear fit is shown below.

$$\vec{f}_i = b_0 + b_f \vec{Z}_f + b_a \vec{Z}_a + b_r \vec{Z}_r \tag{11}$$

where …

$\vec{f}_i$ = firing rate vector for unit *i*, in spikes per second.

$\vec{b}$ = vector of regression coefficients for unit *i*.

$\vec{Z}_f$ = vector of wrist **flexion**

$\vec{Z}_a$ = vector of wrist **abduction**

$\vec{Z}_r$ = vector of wrist **rotation**

The vectors $\vec{Z}_f$, $\vec{Z}_a$, and $\vec{Z}_r$ can be comprised of either wrist angles or wrist angular velocities.

The R^2 values obtained from Equation 11 using position variables are shown in Figure 54. It can be seen from Figure A that the motor cortical firing activity is linearly related to multiple wrist DoFs. The distribution has a maximum R^2 of 0.32, and a mean R^2 of 0.078. Panels B, C, and D show the distribution of regression coefficients b_f, b_a, and b_r respectively in (Hz / Degree). The minimum of these distributions is -1.5, the maximum is 1.5 and the means are -0.0263, -0.0239, and -0.0099.

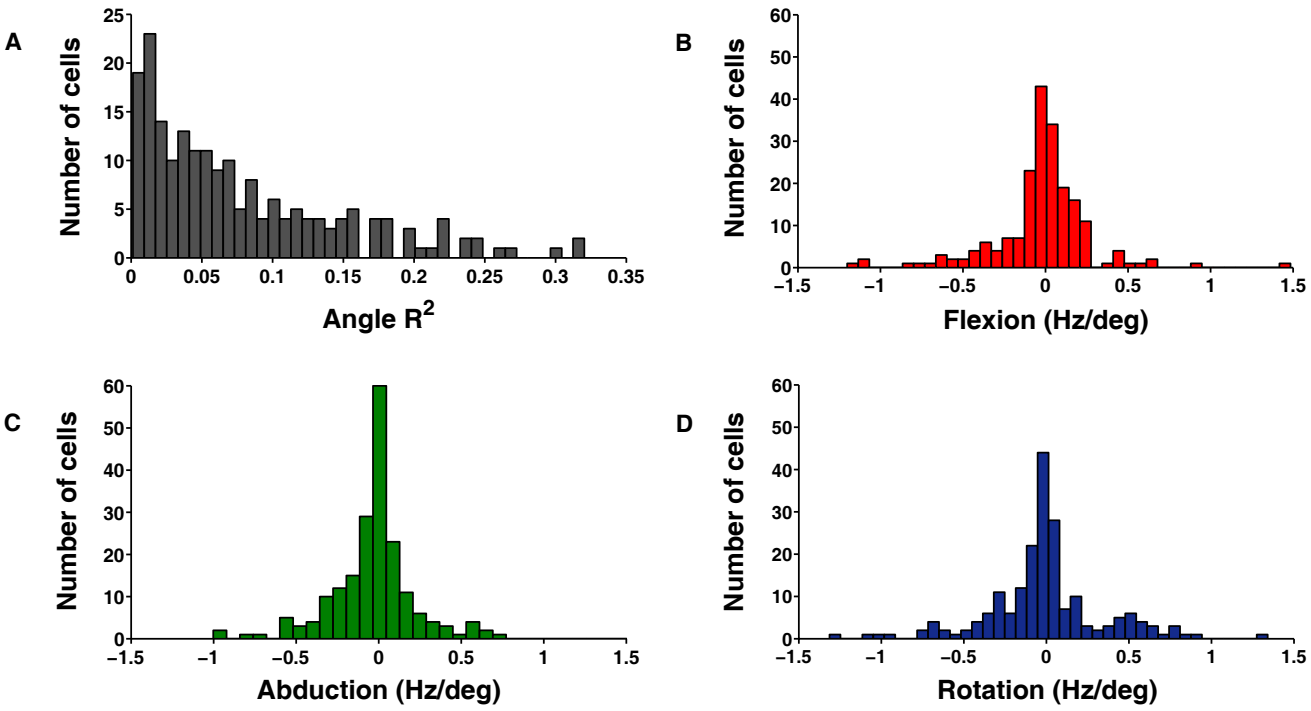

Figure 54. Position histograms.

Figure A shows the distribution of R^2 values obtained from the multiple linear regressions of spike rates and wrist angles. Figures B, C, and D show the distribution of coefficients in (Hz / Degree) obtained from these regressions. Figure B corresponds with flexion, C – abduction, and D – rotational DoFs.

Figure 55 shows a similar set of plots corresponding to wrist angular velocity. These regressions were performed with the same spiking activity; however the independent variables were changed from position to velocity. The maximum R^2 in these regressions was 0.45, the average was 0.044. Panels B, C, and D show the distribution of regression coefficients b_f, b_a, and b_r respectively in (Hz / Degree/sec). The minimum of these distributions is -0.15, the maximum is 0.15 and the means are 0.0019, -8.0437e-005, -0.0039.

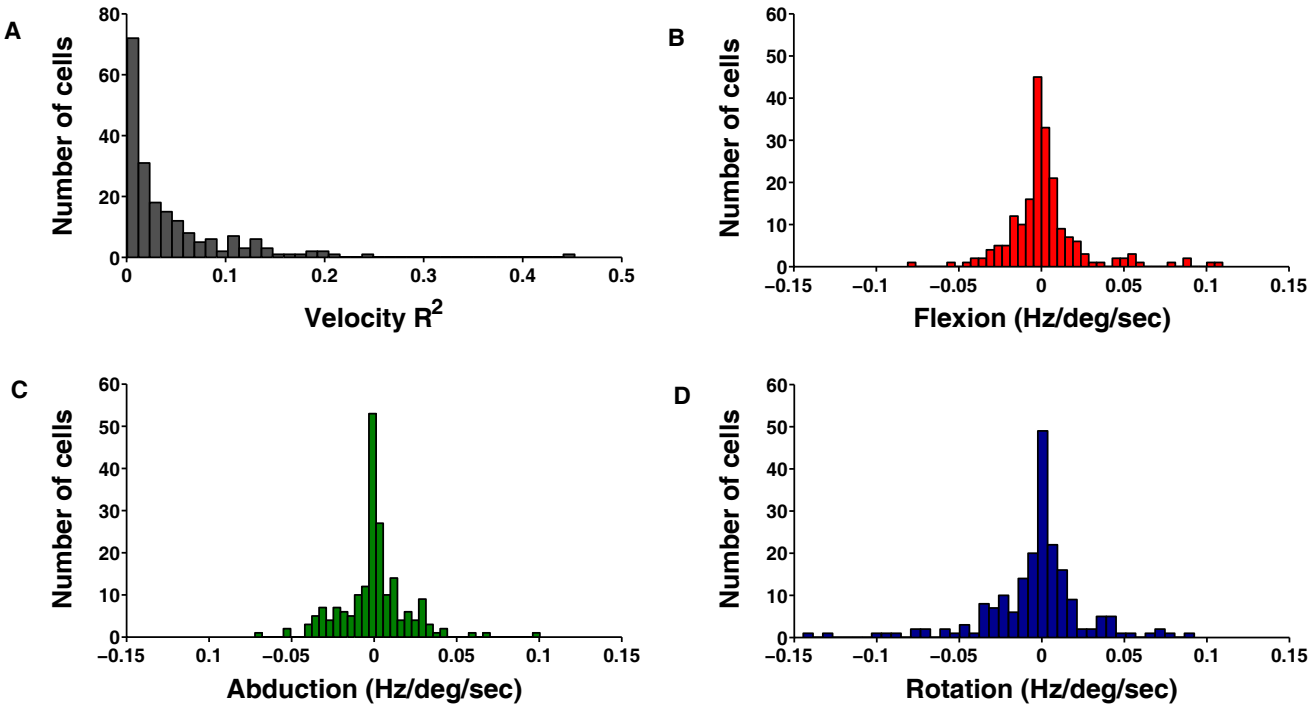

Figure 55. Velocity histograms.

Figure A shows the distribution of R^2 values obtained from the multiple linear regressions of spike rates and wrist angular velocity. Figures B, C, and D show the distribution of coefficients (Hz / Deg/sec) obtained from these regressions. Figure B corresponds with flexion, C – abduction, and D – rotational DoFs.

In linear regression, the size of the coefficient for each independent variable represents the size of the effect that variable has on the dependent variable. The coefficient value indicates how much the dependent variable is expected to increase when the independent variable increases by one if all other variables are held constant. The sign of the coefficient represents the direction of this effect. In the current analysis the scale of the coefficients for position is ten times larger than that for velocity. This does not indicate that the effect of change in position on firing rate modulation is ten times the effect of velocity. This does indicate that a change in one degree has a larger affect on the firing rate than a change in one degree per second.

In order to better understand if the motor cortical population is more linearly correlated to wrist positional or velocity variables we compared the R^2 values from the multivariate regressions. Figure 56 shows two plots comparing velocity and positional multi-dimensional regression correlations. Figure A shows a histogram of the difference between velocity $R^{2'}$s and position R^2's. The positive skew to the distribution indicates that the motor cortical population is more correlated to multiple wrist angles than angular velocities. Figure B shows the R^2 values for position plotted directly against the velocity R^2's with a unity line for easy comparison. The points below the unity line represent those cells that are more tuned to wrist position than wrist angular velocity.

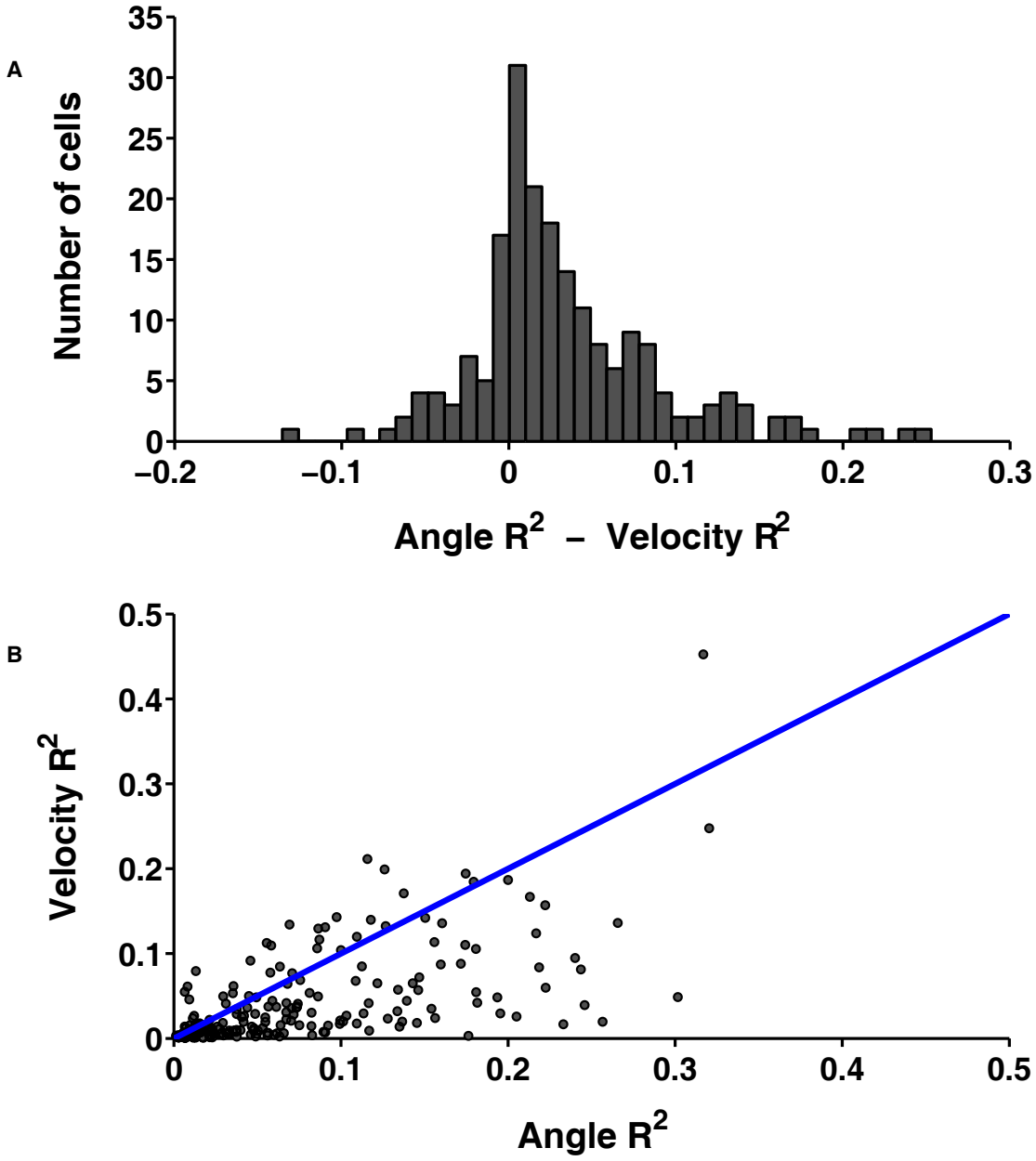

Figure 56. Position correlation histograms.

Figure A shows the distribution of Position minus Velocity R^2's obtained from the multiple linear regressions between all three wrist DoFs and spiking activity. Figure B shows the R^2 values plotted directly against one another. In this Figure the number of data points corresponds to the number of motor cortical cells.

To assess the linearity of the population as it relates to the wrist position, we analyzed the firing rate as a function of the predicted firing rate from Equation 11. Figure 57 shows the distribution of correlation coefficients for predicted firing rates from the linear fit with the actual firing rates. If the three-degree of freedom fit presented above (Equation 11) fully accounted for all the variance in spiking activity the predicted and actual spike rates would be equal (r = 1). If the spiking activity was not at all linearly related to the three wrist angles, the correlation would be zero. The average correlation between predicted and actual firing rates is 0.25.

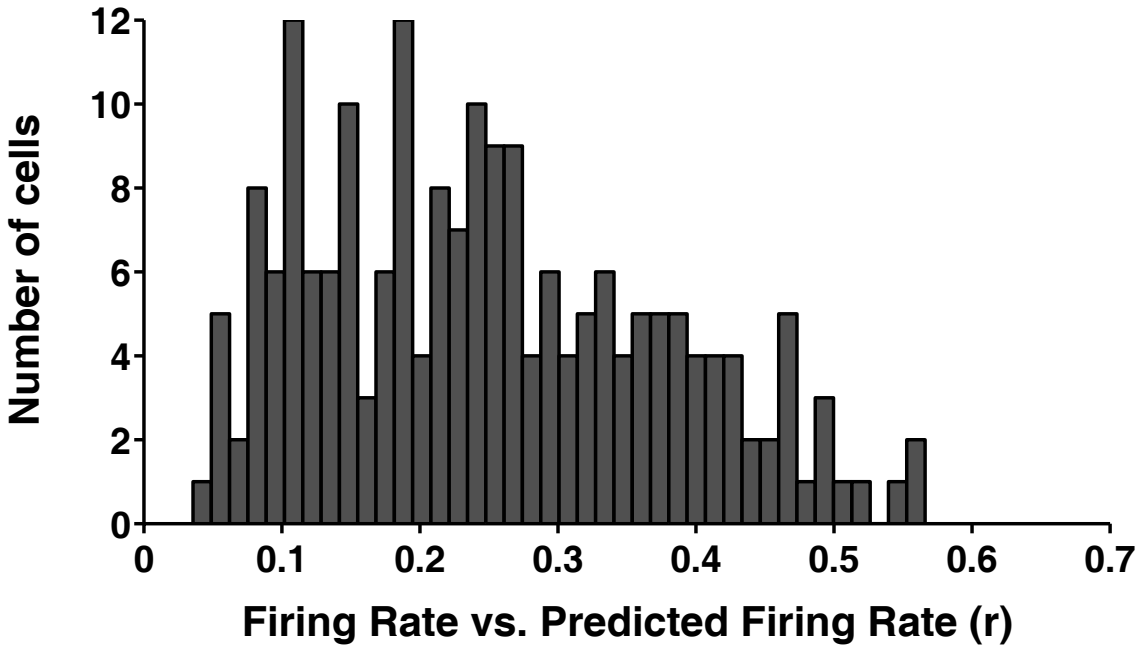

Figure 57. Firing rate versus predicted firing rate.

This Figure shows the distribution of correlation coefficients for the relationship between firing rates predicted from the linear 3 DoFs wrist angle fit and the actual rates recorded in the reach-to-grasp task.

4.4 PREDICTING WRIST JOINT ANGLE FROM POPULATIONS OF MOTOR CORTICAL CELL SPIKING ACTIVITY

Decoding algorithms are used in motor restorative prosthetics that direct the movement of artificial devices from the activity of central nervous system cells. In order to transform the previous analysis into the basis of a decoder we will progress from individual cell analysis to populations.

The cells included in this analysis were chosen based on the following criteria. The neural recording was labeled as “stable”, they were determined to be well isolated, they had an R^2 that was greater than 0.1 from a multiple linear regression with averaged firing rates and averaged wrist angles. Using this criterion, 199 cells were included in the population. The correlation between the averaged cells firing rate and average wrist pronation/supination is shown in Figure 58.

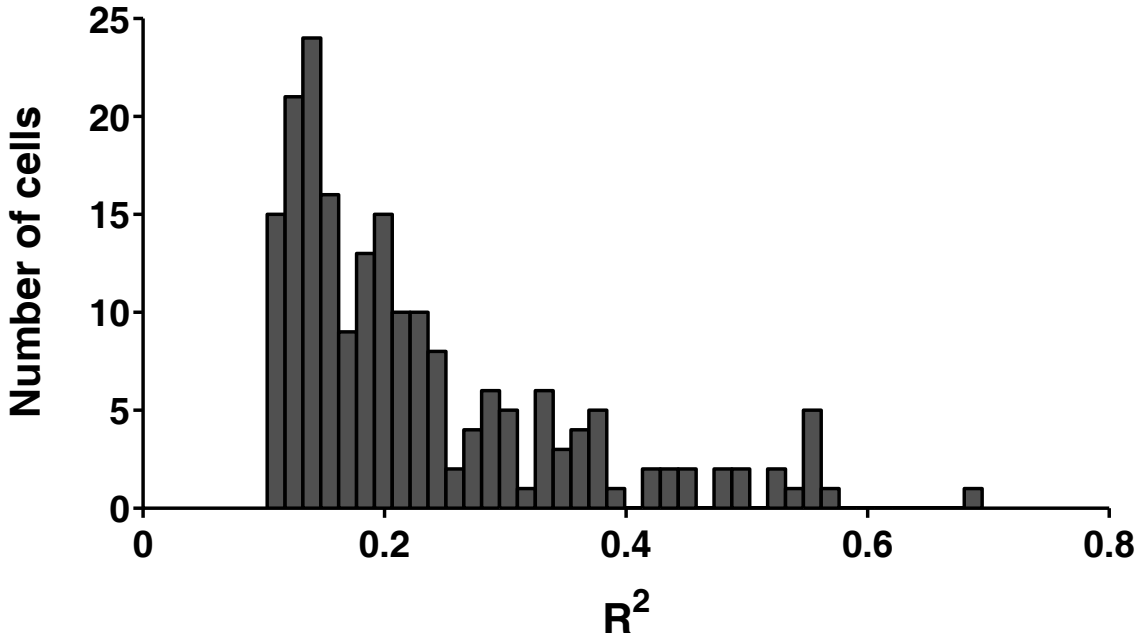

Figure 58. R^2 distribution for cells used for wrist predictions.

This Figure shows the distribution of R^2's for the population of cells used to predict wrist orientation.

The preferred direction vector (pd) presented by Georgopoulos [54] describes the direction of arm movement, in Cartesian coordinates, that is correlated with a motor cortical cell's maximal firing rate. A similar operation has been performed in this work, however the pd is the wrist orientation associated with maximal firing.

A preferred wrist orientation vector (i.e. normalized regression coefficients from Equation 11) was obtained for each cell in the population. These vectors are shown in a single distribution in Figure 59.

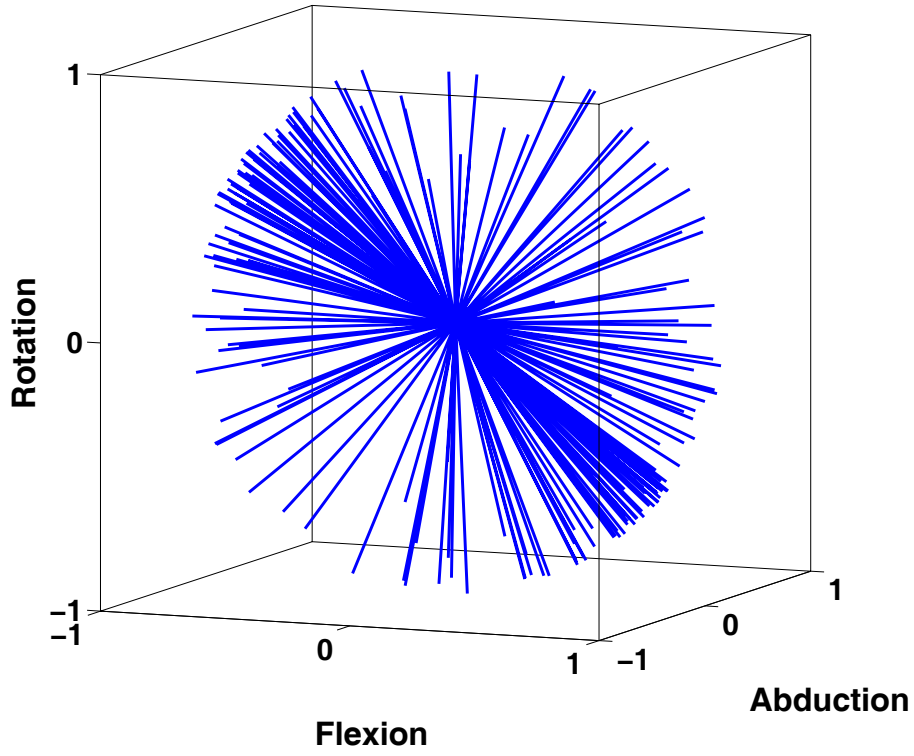

Figure 59. Three dimensional wrist angle preferred direction vectors.

This plot shows a graphical representation of the population of preferred direction vectors. The angle DoFs have all been normalized to a unit length.

If these unit vectors were perfectly uniform, the length of the summed vector would equal zero. The resultant length of the sum of the population of pd's in our population is 9.05. The population is not perfectly uniform, but the pd's in the analysis are sampled from only a small portion of motor cortical cells. The question becomes; can we assume that the larger population of motor cortical cells would have pd's that form a truly uniform distribution?

Using a bootstrapping method, we compared the sum of the pd's in our population with the sum of unit vectors drawn from a uniform distribution (Figure 60). The bootstrap method

created 1,000 unique populations of unit vectors, 200 in each population. For comparison, a vector length calculation was performed by summing the unit vectors in all populations. The length of the vector was used as a measure of non-uniformity. A longer summed vector correlated with a less uniform distribution. The vector distributions were created by…

$$\vec{Z} \sim Unif\left[-1,1\right]$$

$$\vec{\Theta} \sim Unif\left[0,2\,pi\right]$$

$$r = \sqrt{1-\vec{Z}_i^{\,2}}$$

$$\vec{V}_i = \left[r \times \cos(\Theta_i), r \times \sin(\Theta_i), Z_i\right]$$

(12)

where …

$\vec{Z}$ = a vector containing 200 randomly selected points between -1 and 1.

$\vec{\Theta}$ = a vector containing 200 randomly selected angles between zero and two pi.

r = a scaling factor to maintain a unit vector.

$\vec{V}$ = 200 unit vectors created from a spherically uniform population.

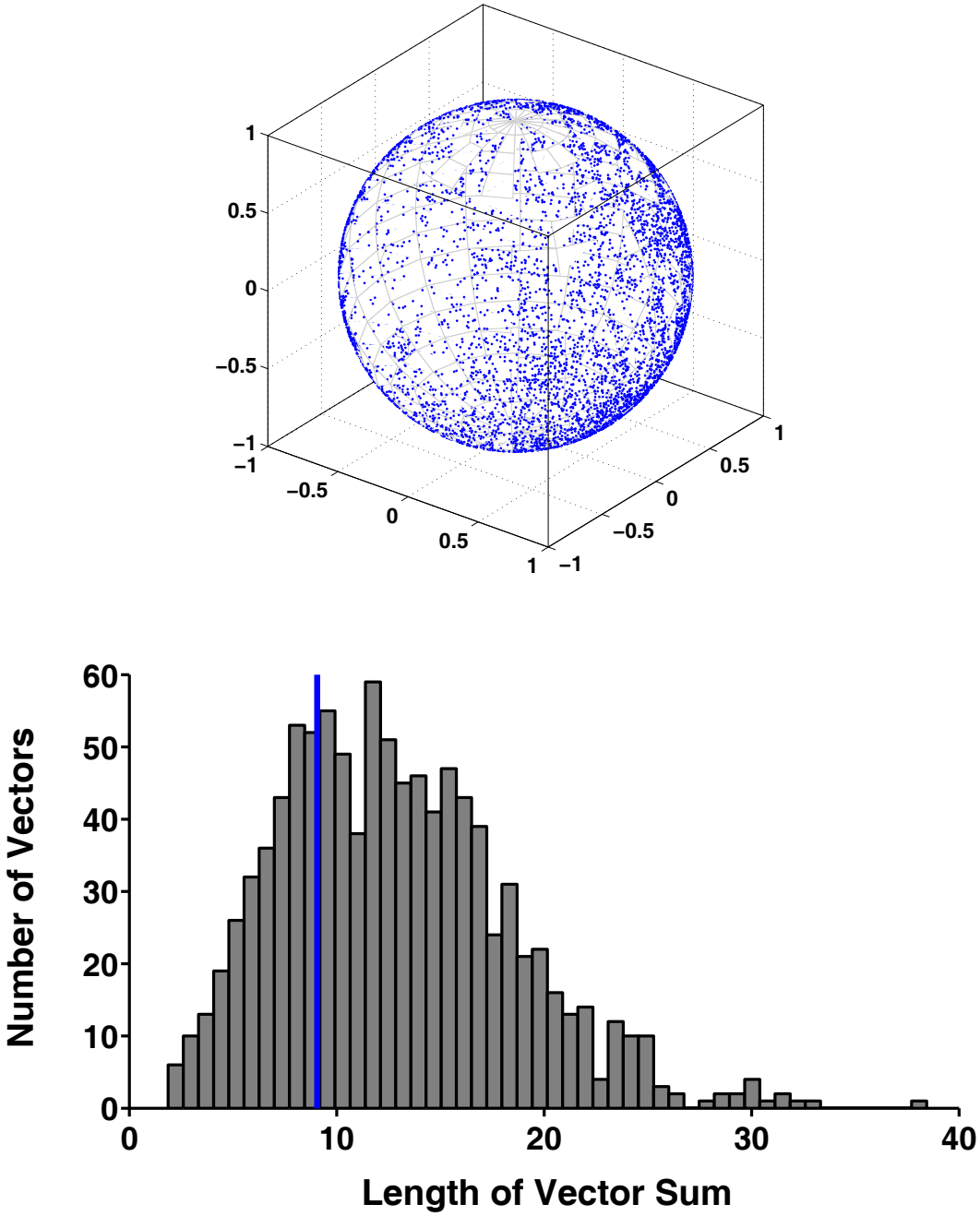

Figure 60. Uniformity of preferred directions.

The top panel of this figure shows an example of the distributions calculated from the equations above. Each dot represents the end-point of a unit vector on a sphere. The bottom panel shows the distribution of vector lengths calculated from the sum of the unit vectors. The length of the summed pd vector is shown in blue.

The length sum of the pd's in our population compared to those drawn from uniform distributions is shown in Figure 60. The measure of uniformity for the population of pd's is within the expected range. The pd's calculated from our population of cells likely represent just a small sample of pd's from a larger uniform population.

The multiple linear regression equation presented in the previous section can be transformed with simple algebra for prediction with an optimal linear estimator (OLE) [84, 85, 86]. Equation 11 can be rewritten as…

$$f_i - b_0 = \vec{b}_i \cdot \vec{Z} \tag{13}$$

where …

f_i is a firing rate for cell i

b_0 is the baseline firing rate for cell i

$\vec{b}$ is the vector of regression coefficients, [1x3]

$\vec{Z}$ is a vector of predictor variables, [3x 1]

…given the regression coefficient vector ($\vec{b}_i$) for each cell…

$$\vec{f}_t - \vec{b}_0 = B \cdot \vec{Z}_t \tag{14}$$

$\vec{f}$ = firing rate vector for *n* cells at time t, [*n* x1]

$\vec{b}_0$ = a vector of baseline firing rates, [*n* x1]

$$B = \begin{bmatrix} b_{1,f}, & b_{1,a}, & b_{1,r} \\ b_{2,f}, & b_{2,a}, & b_{2,r} \\ ...., & ...., & ...., \\ b_{n,f}, & b_{n,a}, & b_{n,r} \end{bmatrix}$$ a [*n* x 3] matrix of regression coefficients

$\vec{Z}$ = a vector of the wrist angles at time t. [3 x 1].

…the prediction equation is …

$$\hat{\vec{Z}}_t = (B^T \cdot B)^{-1} \cdot B^T (\vec{f}_t - \vec{b}_0) \tag{15}$$

…where …

$\hat{\vec{Z}}_t$ = prediction of wrist angles at time t. [3 x 1].

B^T = the transpose of the coefficient matrix

The more linearly correlated cells used in this decoder, the more accurate the prediction. During real-time decoding experiments, researchers have the ability to record from several dozen individual neurons at any single moment in time. In this experiment the maximum number of cells recorded simultaneously was 11. In order to obtain an adequate number of cells while minimizing the variance across many days we utilized average firing rates and average angles for a presented object and orientation. Thus all the cells recorded are combined and treated as if they were recorded simultaneously. The results from the prediction can be seen in Figure 61. This

Figure shows the predicted wrist angle and the actual wrist angle for an average object presentation of the small rectangle in the extension position.

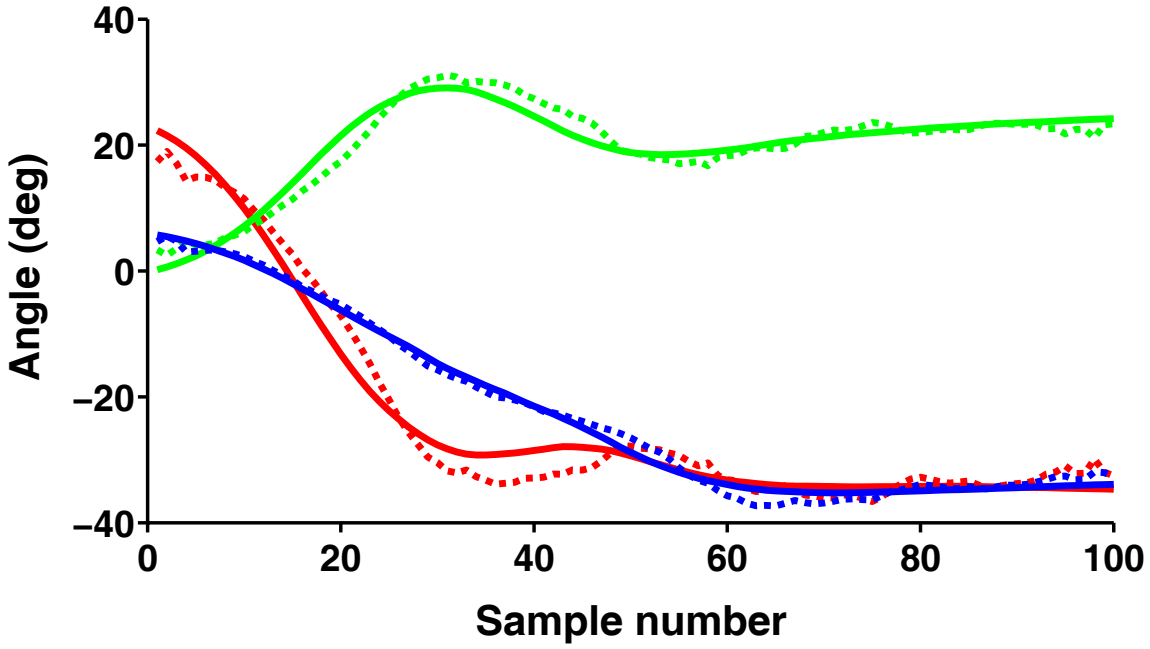

Figure 61. Predicted versus actual wrist orientation.

The figure shows predicted vs. average wrist orientation for the three wrist DoFs. The average firing rates and wrist angles are calculated for small rectangle in the extension presentation. The solid lines are the actual, and the dotted lines are the predicted. The green curve shows the abduction, red the flexion, and blue the rotational DoF. The correlation coefficients for the three curves are 0.89 (green), 0.92 (red), and 0.84 (blue) respectively.

The wrist orientation predictions from motor cortical firing rate shown above were accomplished by using all the cells in the population and average angle data for presentation of the small rectangle in the extension position. This was not a cross validated prediction. For cross validation we chose a 70/30 split for training and testing data. 70% of the original kinematic and firing rate data was used for training, and the remaining 30% was used for testing. The data removed from the training sets are equivalent to removing an object presentation and the

corresponding firing rates. The training data was used to calculate the coefficient matrix (Equation 14). The testing data included the spike rates for those presentations not included in the training data. The cross validation was using testing spike rates to predict average wrist angles for targets not included in the calculation of the coefficients. We applied this analysis to 100 different 70/30 repetitions (separate draws of the training and testing data). The comparison between the actual and predicted wrist orientations for the testing data set is shown in Figure 62.

The red, green and blue lines represent the actual wrist angles for the flexion, abduction and rotational DoFs. The dots on each graph represent the fits prediction of naïve wrist. Figure 63 shows the average prediction accuracy across all presentations. The data points in this plot were obtained by taking the average prediction for all the cross-validation sample points. The average correlation between actual and predicted wrist angles was 0.75, 0.735, and 0.74 for flexion, abduction and rotation respectively.

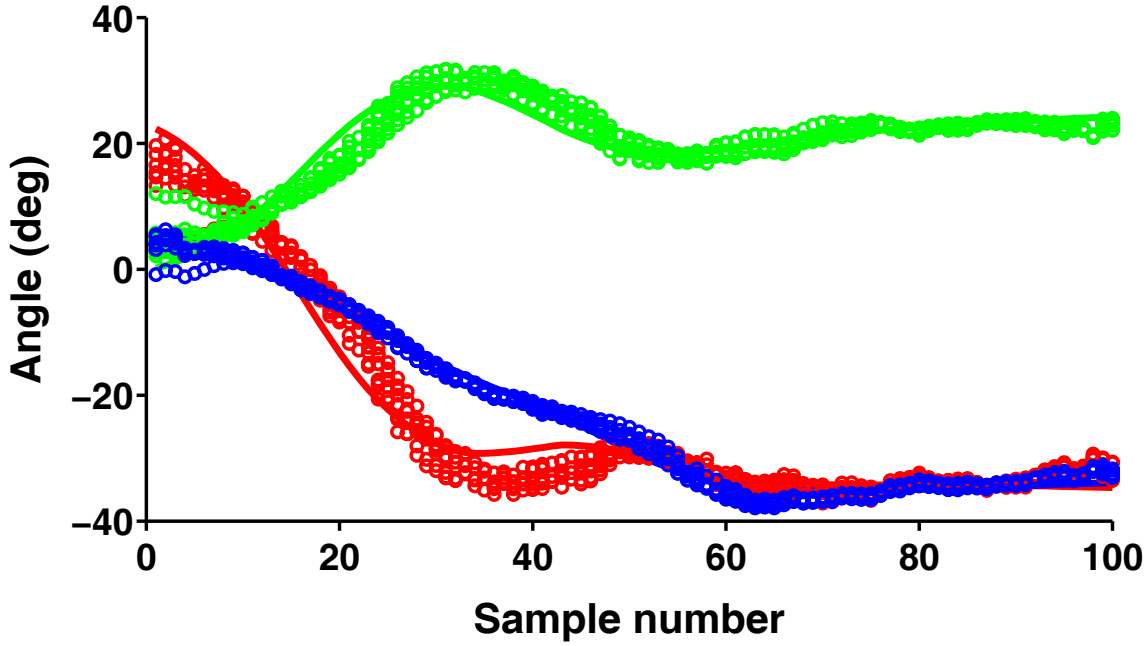

Figure 62. Cross validation of wrist decoding fit

Plots A, B, and C show actual vs. predicted wrist angles for flexion, abduction and rotation DoFs. The solid lines show the actual wrist angles. The black dotted lines in each plot show the predicted angle for the testing data set.

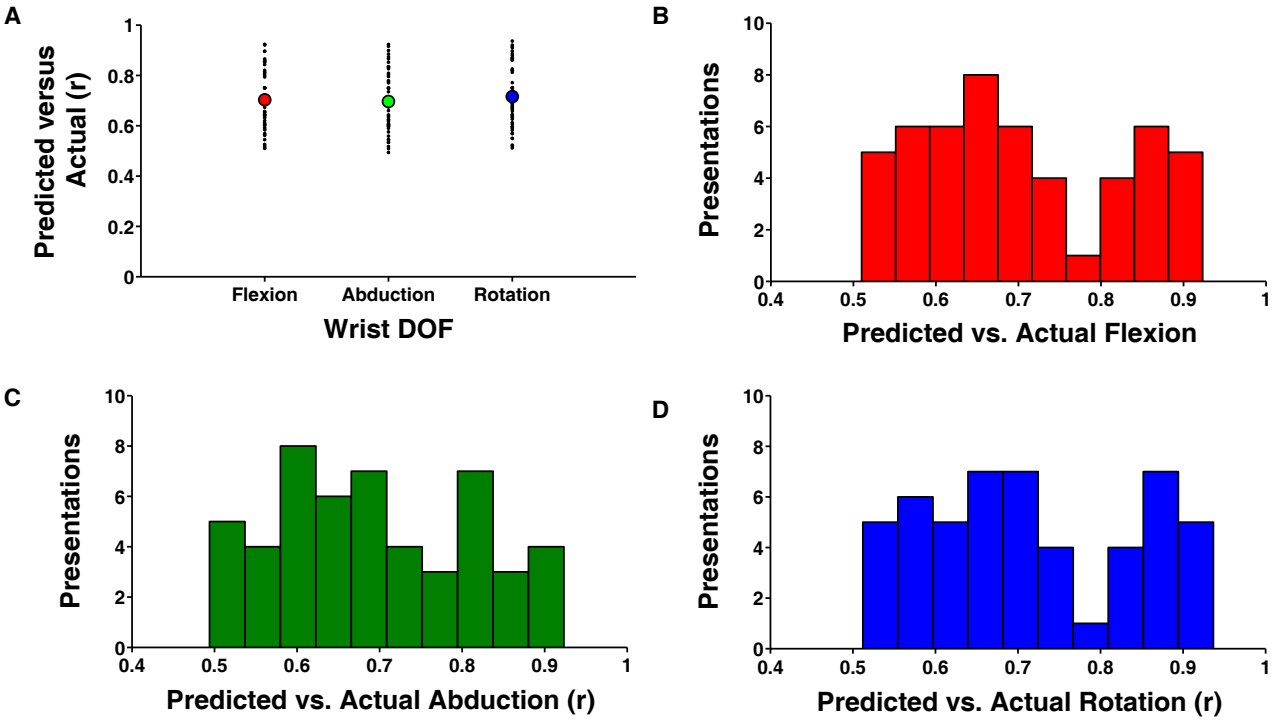

Figure 63. Accuracy of prediction across all presentations.

Plot A shows the prediction accuracy across all presentations. The x-axis shows flexion, abduction and rotational DoFs. The colored circles indicate the mean accuracy for the named DoFs. Figure B, C, and D show the distribution of the correlation between actual and predicted angles for the flexion, abduction and rotational DoFs.

4.5 DISCUSSION

The correlations between the wrist DoFs in well trained monkeys appear to non-physiologic. The wrist DoFs are not naturally correlated in reach-to-grasp movements. The change in these correlations was related to the monkey's ability to perform more movements in a single session.

This was interpreted as a method to decrease the overall energy expenditure, making early fatigue less likely, allowing the animal to receive more rewards per day.

The investigations comparing the correlation between motor cortical firing and wrist kinematics were performed with single and multiple variable linear fits. The single linear fit (Equation 10) compared the correlation between spiking activity for position and velocity variables. One variable was not more correlated to motor cortical spiking dynamics than another. Using a multivariate linear (Equation 11) fit, the populations of motor cortical cells were more correlated with position. This fit was used to calculate a unit vector for each cell that pointed in the wrist orientation corresponding to the maximal firing rate, i.e. preferred direction (pd).

The correlation matrix, calculated from the multivariate linear regressions, was used in an optimal linear estimator to calculate a prediction of average joint angle. The correlation between predicted and actual average flexion, abduction and rotation angles for the small rectangle extension position was 0.89, 0.92 , and 0.84, respectively. The fit was cross-validated using a 70/30 split for training and predicting. The average correlation between actual and predicted wrist angles across all object presentations was 0.75, 0.735, and 0.74 for flexion, abduction and rotation respectively.

One limitation in motor restorative devices is the limited number of simultaneously controlled DoFs. In the past we have used a multivariate linear fit to predict the x, y, z location of the end-point of a robotic arm [65, 87, and 88]. We have recently added a gripper degree of freedom to this control scheme [71].

Advancing a control system beyond four DoFs cortical control would be a significant advancement. The results presented in this chapter show that it is feasible to use individual motor cortical firing activity to predict joint angles of three wrist DoFs. This decoding equation (Equation 14) may be expanded in the future by using real-time data collected from a large population of simultaneously recorded motor cortical cells. This would allow us to move beyond average predictions, and to study the relationship more dynamically. It is likely that a full tuning model including many kinematic variables, sophisticated models that take into account non-linear relationships between spiking activity and wrist movement, will create better control for real-time motor restorative devices.

5.0 GRASPING KINEMATICS CORRELATION TO THE SPIKING ACTIVITY OF SINGLE MOTOR CORTICAL CELLS

The hand has 23 DoFs across 16 joints. Motion about these joints is coordinated during grasping movements [38, 39, 40, and 41]. Complex grasping movements can be characterized by simplified patterns of joint displacement [1, 35, 46, 47, 76], as demonstrated in Chapter 3. A fundamental goal of this work is to better understand how firing rates in the motor cortex relates to changes in hand shape. The motor cortex may direct the hand by controlling many different kinematic variables (finger-tip force, joint velocity, joint acceleration, joint position, end-point velocity etc.). In this study we investigate joint angle, joint angular velocity and grasping synergies as they relate to changes in spiking activity. The information gained by the neurophysiological investigation will guide the predictive methods designed for neural prosthetics.

From a prosthetics standpoint, attempting to control a robot with 23 simultaneous independent DoFs using a neural signal is nearly insurmountable. The neurophysiological results of the variable analysis may show that motor cortical cell do not ‘prefer’ hand synergies as a control signal, however this may still have utility in prosthetics. Controlling a robotic hand with grasping synergies, instead of individual joints, may constrain the robot to more physiologic

postures. It may also be completely unnecessary to control all DoFs of hand shaping for accurate and anthropomorphic hand movements.

From a neurophysiological standpoint it has been shown that lesions of the motor cortex (M1) and its descending projections to the spinal cord (corticospinal tract CST) produce hemiparesis. This is a syndrome characterized by weakened movements that result in simultaneous action of all the fingers when grasping is attempted [89, 90]. Similar deficits are seen when reversible inactivation of monkey M1 hand region was studied [91, 92].This suggests that other descending pathways are capable of producing more rudimentary hand gestures. It has been shown from neural recordings that the firing rate of neurons in the motor cortex is correlated to multiple finger and wrist movements [93]. Combining these results, it suggests that M1 may be directing the coordination of a less complex substrate of hand movement, as opposed to individual muscles or joints.

Based on the aforementioned studies, it is reasonable to theorize that motor cortical spiking activity is highly correlated with object features, individual joints, individual joint velocities, forces, or hand shape synergies. Spiking activity of individual cells certainly changes as a function of object presented (Figure 64). Firing rate modulation may not be merely a consequence of object features, but correlated with changes in hand shape that develop over the entire reach-to-grasp movement.

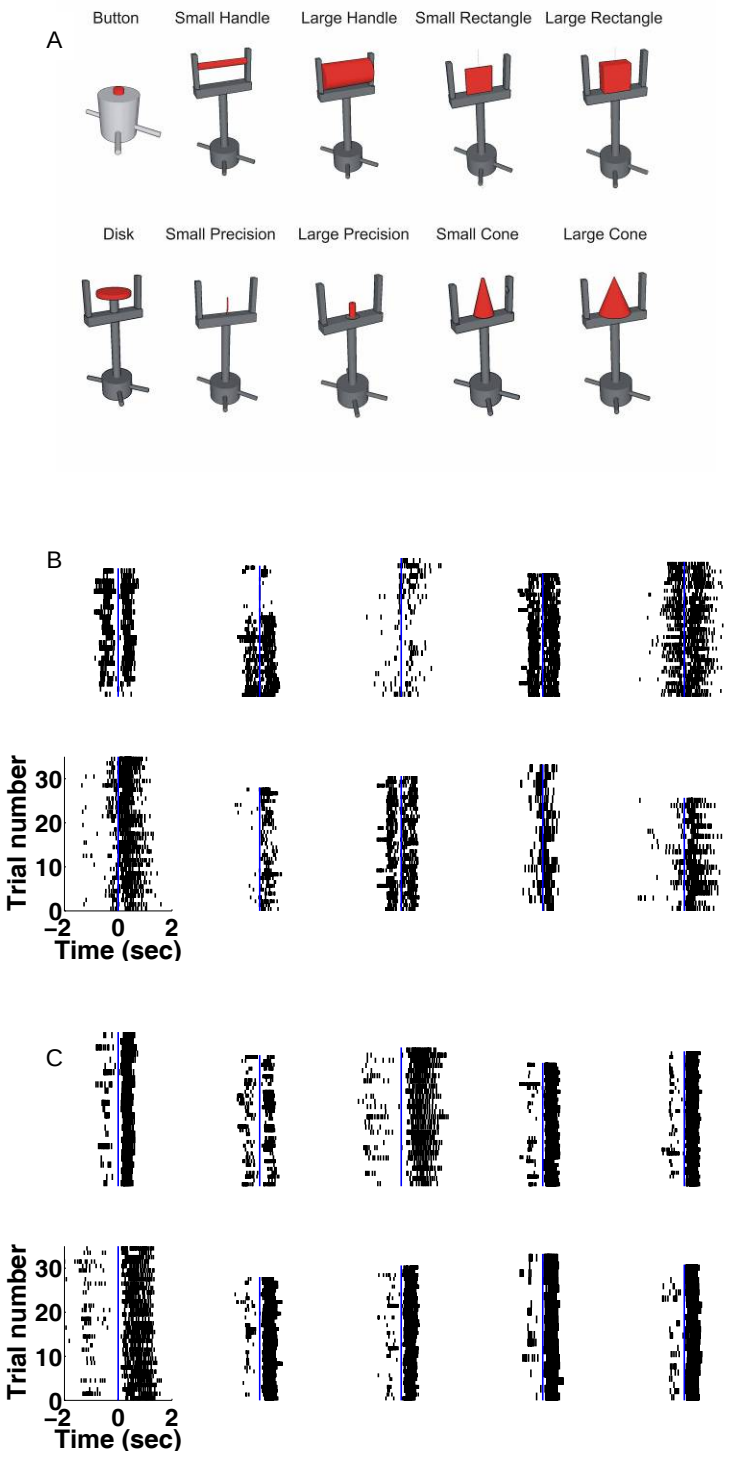

Figure 64. Object related spiking activity.

Plot A shows the ten objects used in the reach-to-grasp task. Plots B (monkey V, Session 42, Cell 2a) and C (monkey B, Session 19, Cell 1b) show raster plots of single cells as a function of object. The trials for a single object

have been stacked vertically into a group. The ten raster groups correspond with the ten different objects grasped in Figure A. Each trial is represented by a horizontal raster. Each dark vertical line, making up a raster plot, represents a single spike. The blue vertical lines correspond to the start of movement.

In this chapter we explore the possibility that the motor cortex is correlated with more than general objects, or general changes in aperture [94, 95]. We focus on individual joints (velocity and position) and hand shape synergies to determine variables that are most correlated with firing rate of a single cell. In previous sections (4.4), corresponding to the wrist DoFs, we performed a similar analysis with independent single linear regression for all joints. Due to the high number of DoFs, we will make comparisons in hand shape using a multivariate approach. The results from this analysis will be used to predict hand shape from populations of individual motor cortical cells.

5.1 SPIKING ACTIVITY AS A LINEAR FUNCTION OF JOINT POSITION, JOINT VELOCITY, AND GRASP SYNERGIES

This analysis has been separated into three categories: position, velocity and grasp synergy. To accurately compare the R^2 values from linear regression, we must use the same number of regressors. We measured 20 DoFs involved with hand shaping. The position and velocity variables nicely fit into this fit, one per joint. However, to compare these variables with grasping synergies we reconstructed the 20 DoFs from a few eigenvectors. The first four eigenvectors were used for reconstruction. This selection was based on the data added per eigenvector in

Figure 39 of Section 3.4.2. This showed that reconstructions done using the first four eigenvectors correlate well to actual joint angles; >90% for the MCP flexion, DIP, PIP DoFs; >70% for the thumb DoFs, but only 40% for the MCP Abduction DoFs.

5.1.1 Multiple Degree of freedom tuning

Using multiple linear regressions we can investigate how a cell's firing rate correlates with position, velocity or reconstructed joint angles. The multiple linear regression fit used for this analysis is:

$$\vec{f}_i = b_0 + b_1\vec{Z}_1 + b_2\vec{Z}_2 + ...b_{20}\vec{Z}_{20} \tag{16}$$

where …

$\vec{f}_i$ = firing rate vector for unit *i*, in spikes per second.

$\vec{b}$ = vector of regression coefficients for unit *i*.

$\vec{Z}_1$ = vector of 1st dimension

$\vec{Z}_2$ = vector of 2nd dimension

$\vec{Z}_{20}$ = vector of N 20th dimension

We analyzed 327 cells, with a constant 150ms lag between firing and kinematics, using Equation 16. The cells included in this analysis are those that had an R^2 of at least 0.1 for a multivariate regression using average firing rates and average hand and wrist angles (the wrist DoFs are used in prediction, Section 5.2), and are not recorded in the data log as being lost at any

time during the recording session. In the prediction section of this chapter, where a population of cells was needed, we used average firing rates and average kinematic variables. This established the criteria for cells to be included in the analysis.

In the single cell analysis we used fractional interval rates calculated on 30ms bins, and average kinematic data over the same 30ms bin. The R^2 values obtained from the multiple linear regressions are shown in Figures 66-68 (66-position, 67-velocity, 68-synergy reconstructed). The corresponding joint numbers have been shown in Figure 65. The histograms of three different R^2 distributions (position, velocity, and synergy) show that the maximum R^2 in the position, velocity, and joint angle reconstruction was 0.65, 0.67, and 0.61 respectively. The average R^2 for the three variables was 0.25±0.13, 0.18±0.11, and 0.20±0.12. In each figure the B plot shows regression coefficients for all joints of a highlighted cell (red asterisk) in plot A. The joints highlighted in the B plots, with red and a green circles, are shown as firing rate versus the highlighted joint. In general, cells are poorly tuned to a single DoF but have a strong linear relationship with respect to multiple joints.

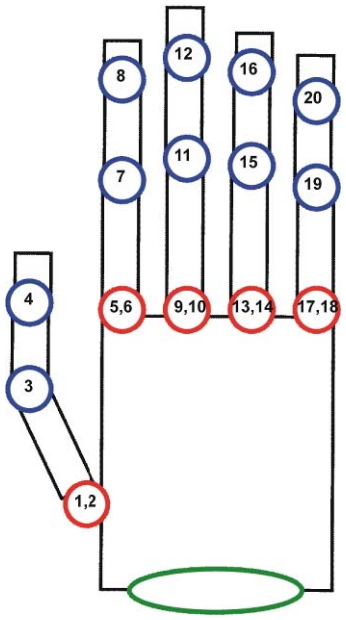

Figure 65. Joint names and corresponding numbers.

This figure represents the joints on a hand, and the corresponding number assigned to them in the following analysis. The joints are as follows 1-Thumb CMC flexion, 2-Thumb CMC abduction, 3-Thumb MP flexion, 4-Thumb IP flexion, 5,9,13,17 – 1^{st} ,2^{nd} ,3^{rd} ,4^{th} fingers MCP flexion, 6,10,14,19 – 1^{st} ,2^{nd} ,3^{rd} ,4^{th} fingers MCP abduction, 7,11,15,19 - 1^{st} ,2^{nd} ,3^{rd} ,4^{th} fingers PIP, 8,12,16,20 - 1^{st} ,2^{nd} ,3^{rd} ,4^{th} fingers DIP.

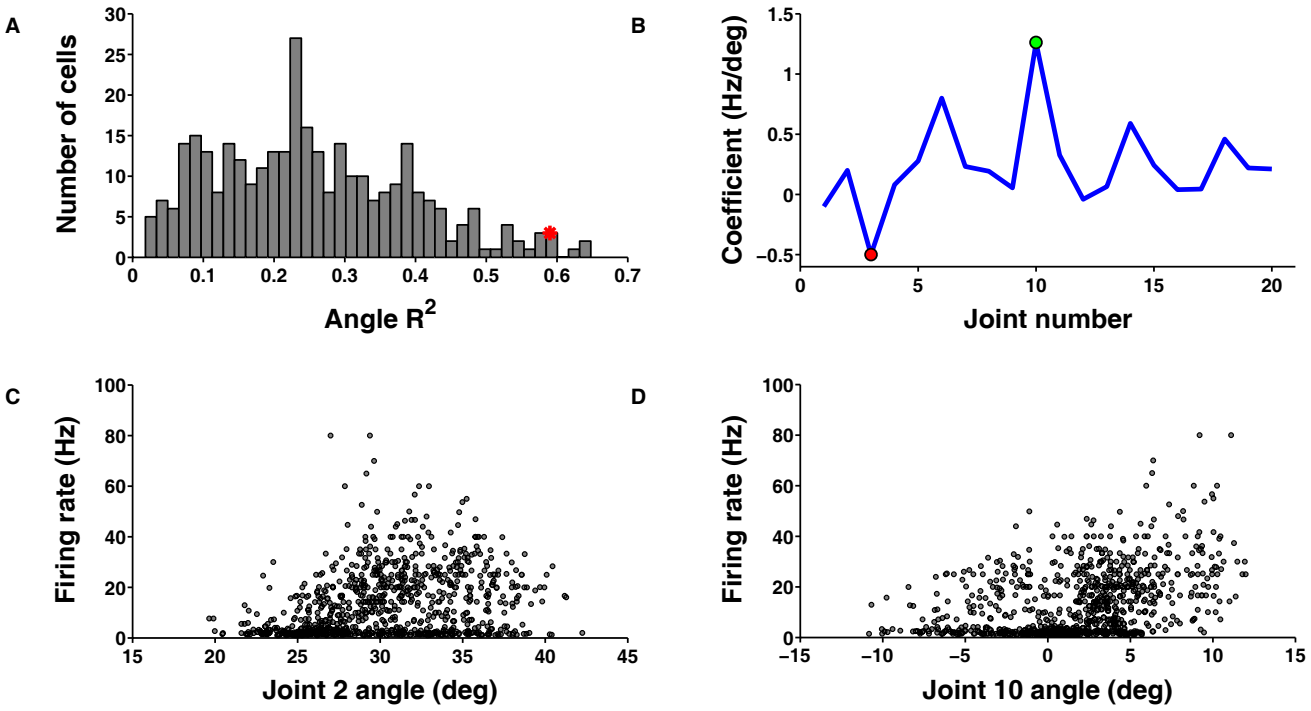

Figure 66. Multiple linear regressions – joint position.

Figure A shows the distribution of R^2 values from multivariate linear regression for 327 different cells with joint position. Figure B shows the regression coefficients for the highlighted cell in figure A (red asterisks). The x-axis shows the joint number relative to the hand in Figure 65. Firing rate as a function of position is shown in Figures C and D for the joints highlighted by the red and green circles in Figure B.

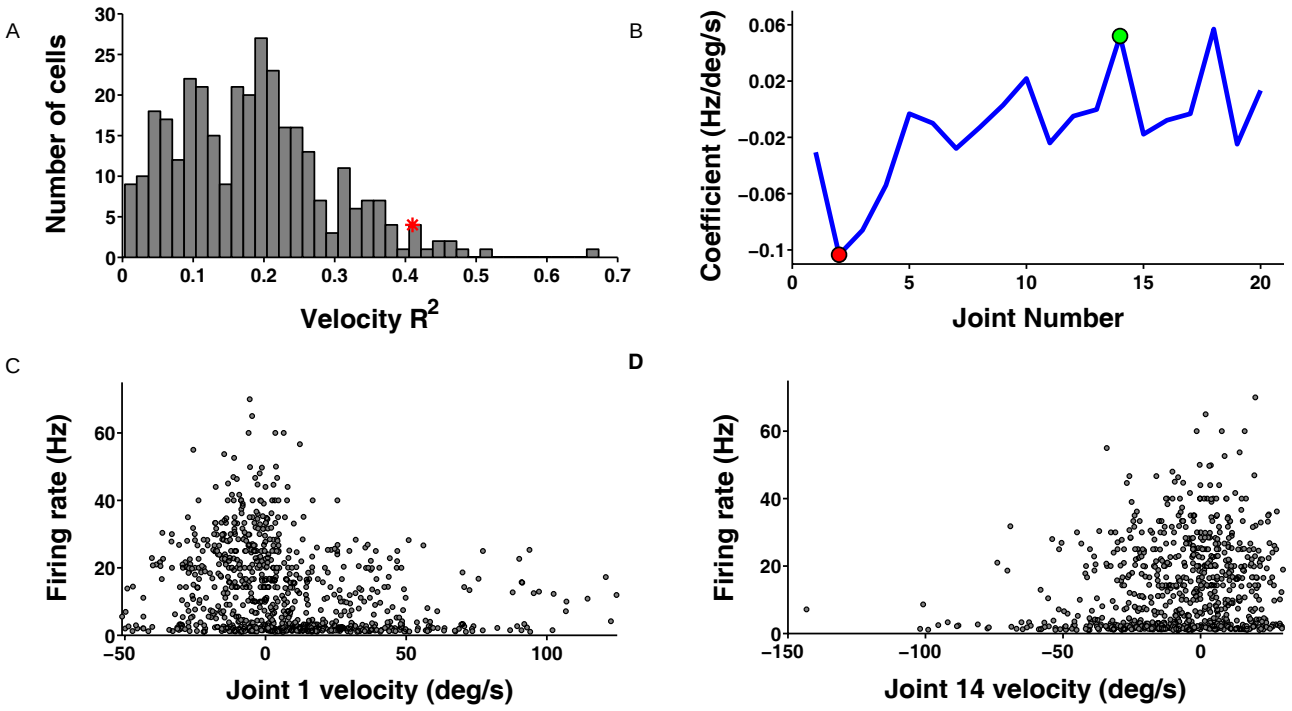

Figure 67. Multiple linear regressions – joint angular velocity.

Figure A shows the distribution of R^2 values from a multivariate linear regression for 327 different cells to joint angular velocity. Figure B shows the regression coefficients for the highlighted cell in figure A (red asterisks). The x-axis shows the joint number relative to the hand in Figure 65. Firing rate as a function of velocity are shown in Figures C and D for the joints highlighted by the red and greed circles in Figure B.

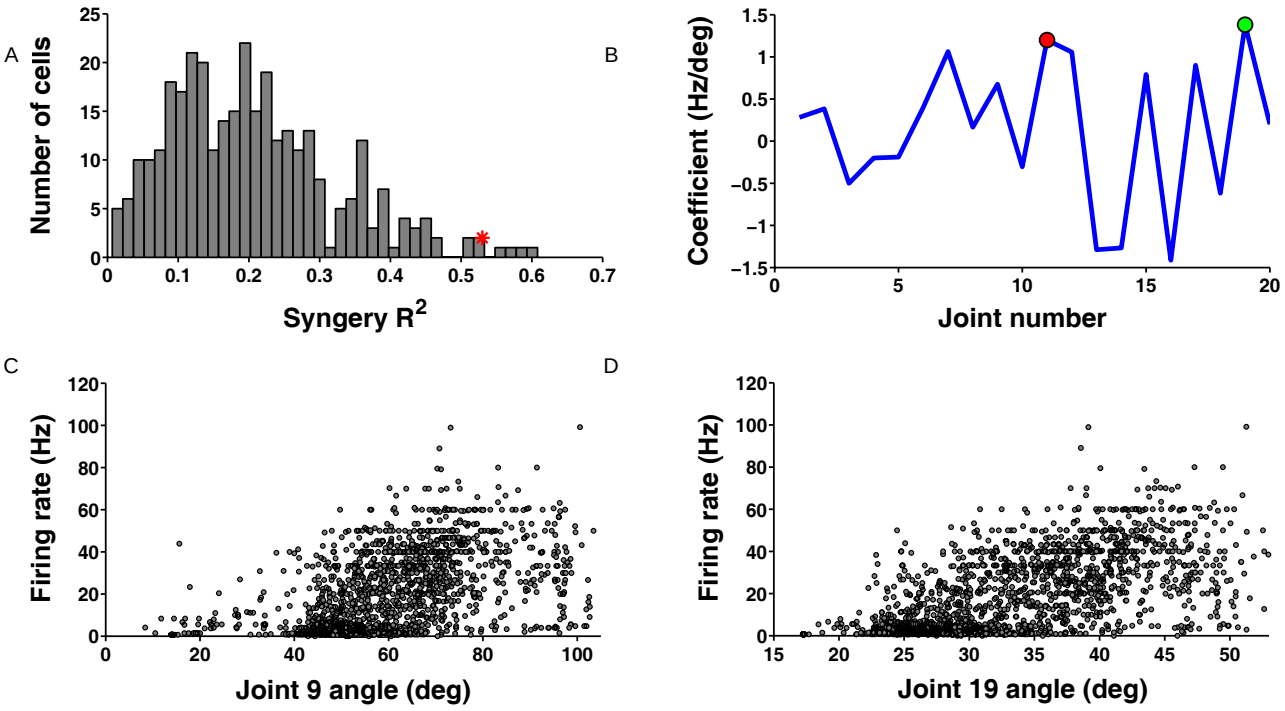

Figure 68. Multiple linear regression – reconstructed joint angles from a few synergies.

Figure A shows the distribution of R^2 values from a multivariate linear regression for 327 different cells to reconstructed joint angle. Figure B shows the regression coefficients for the highlighted cell in figure A (red asterisks). The x-axis shows the joint number relative to the hand in Figure 65. Firing rate as a function of reconstructed joint angle are shown in Figures C and D for the joints highlighted by the red and greed circles in Figure B.

The difference in R^2 values for the above populations may differentiate which variable (position, velocity, and synergy) the motor cortical cells are more linearly tuned (Figure 69). The positive values in both figures indicate that on average the individual firing rates are 15% more linearly correlated with hand shape (position) than velocity, and on average 8% more correlated with hand shape than reconstructions from eigenvectors.

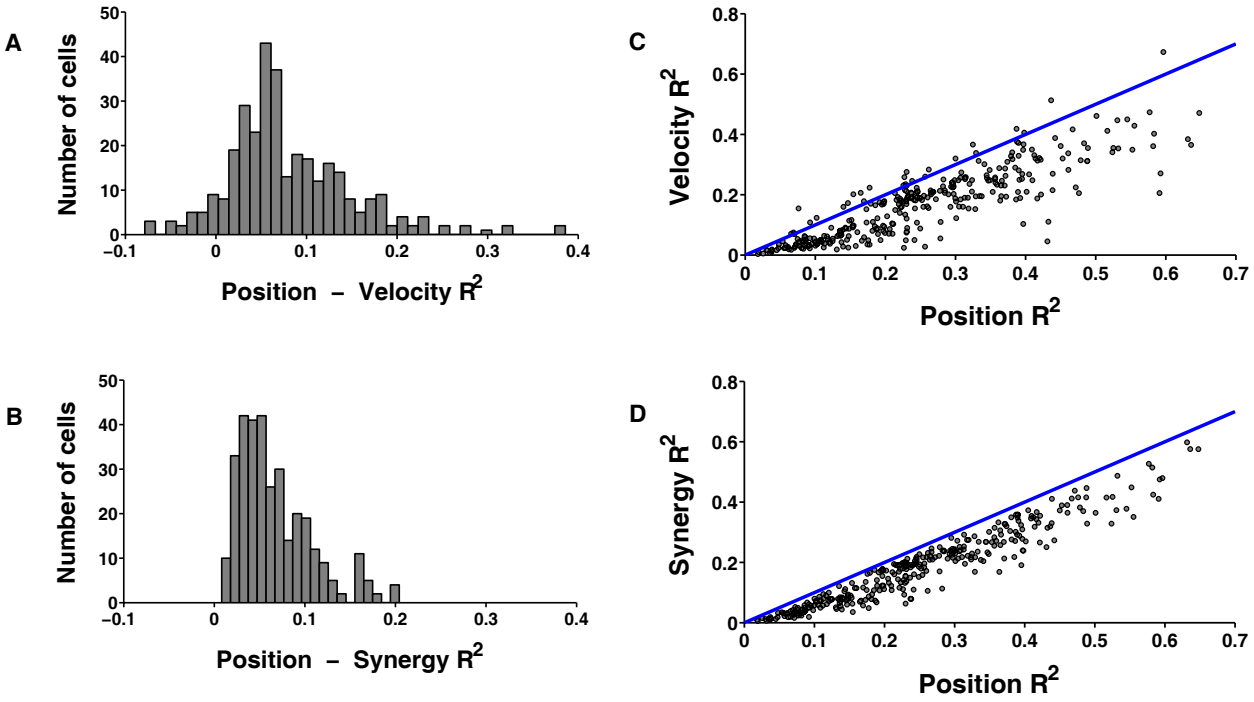

Figure 69. Difference in R^2 – position, velocity and reconstructed hand shape.

Figures A, B show the difference between position–velocity and position-synergy distributions respectively. Figures C and D show the R^2s plotted directly against one another. Each black dot represents a cells R^2 value from a multiple linear regression with 20 DoFs. The blue line shows a line of unity.

The multivariate linear regression using 30ms binned neural and kinematic data show that the population of motor cortical cells is more linearly correlated with joint position than other investigated variables. This is purely a neurophysiological observation. Attempting to control a robotic device using 23 independent joint angle estimates from a population of neural activity may be difficult and produce non-physiologic hand shapes. The synergy reconstruction compared favorably with the individual joint position R^2 values ($r = 0.92$). This suggests that eigenvectors accurately reconstruct the hand, and that little is lost with respect to neural

correlation when using only a few grasping synergies. It may be possible to predict complex grasping movements by predicting the scores of a few eigenvectors.

5.2 PREDICTING HAND SHAPE AND WRIST ORIENTATION FROM THE SPIKING ACTIVITY OF A POPULATION OF MOTOR CORTICAL CELLS

In previous work, Wang and colleagues (2010) presented a decoding algorithm for a motor cortical population that predicts arm translation and hand rotation [83]. In earlier chapters we showed that a population of motor cortical cells could accurately estimate the average angle for three wrist DoFs. Similarly to Wang and colleagues, we will expand the linear fit used to calculate the wrist orientation tuning function to include an estimate of hand shape synergy.

$$\vec{f}_i = b_0 + b_f \vec{Z}_f + b_a \vec{Z}_a + b_r \vec{Z}_r + b_1 \vec{Z}_1 + b_2 \vec{Z}_2 + b_3 \vec{Z}_3 + b_4 \vec{Z}_4 \quad (17)$$

where …

$\vec{f}_i$ = firing rate vector for unit *i*, in spikes per second.

$\vec{b}$ = vector of regression coefficients for unit *i*.

$\vec{Z}_f$ = vector of wrist **flexion** in degrees

$\vec{Z}_a$ = vector of wrist **abduction** in degrees

$\vec{Z}_r$ = vector of wrist **rotation** in degrees

$\vec{Z}_1$ = scores of the 1st eigenvector

$\vec{Z}_2$ = scores of the 2nd eigenvector

$\vec{Z}_3$ = scores of the 3rd eigenvector

$\vec{Z}_4$ = scores of the 4th eigenvector

Using average firing rates for 327 cells and average kinematic variables for one target presentation (see Section 2.5.3) we calculated how well the response variable (firing rate of a cell) was linearly correlated to the seven predictor variables. The distribution of R^2 values from the multivariate linear regression is shown in Figure 70. The cells included in this analysis were only those with an R^2 greater than 0.1. The distribution has a mean R^2 of 0.3375, a standard deviation of 0.129, and a maximum of 0.75. The regression coefficients from Equation 16 were used to build a tuning function for each cell (see below).

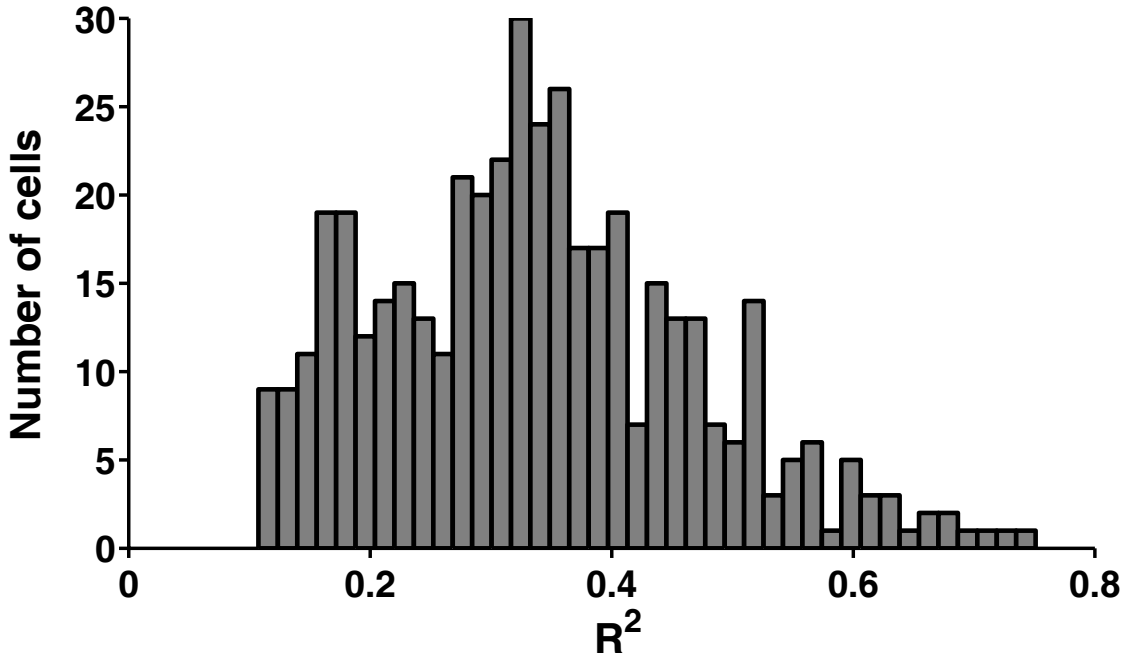

Figure 70. Distribution of correlation coefficients – entire population.

This figure represents the R^2 values obtained from Equation 16. This represents all 327 cells in the motor cortical population.

A decoding algorithm was constructed using an optimal linear estimator [84, 85, 86] to predict hand shape and wrist orientation. The b coefficients were obtained from equation 16 using the averaged binned firing rate and average kinematic data per presentation (5 per session). The transformation of the regression equation into an optimal linear estimator for prediction is shown below.

Equation 16 can be rewritten as…

$$f_i - b_0 = \vec{b}_i \cdot \vec{Z} \tag{18}$$

where …

f_i is a firing rate for cell i

b_0 is the baseline firing rate for cell i

$\vec{b}$ is the vector of regression coefficients, [1x7]

$\vec{Z}$ is a vector of predictor variables, [7x 1]

… given the regression coefficient vector ($\vec{b}_i$) for each cell, a population can be treated…

$$\vec{f}_t - \vec{b}_0 = B \cdot \vec{Z}_t \tag{19}$$

$\vec{f}$ = firing rate vector for *n* cells at time t, [*n* x1]

$\vec{b}_0$ = a vector of baseline firing rates for n cells, [*n* x1]

$$B = \begin{bmatrix} b_{1,f}, & b_{1,a}, b_{1,r}, b_{1,1}, b_{1,2}, b_{1,3}, b_{1,4} \\ b_{2,f}, & b_{2,a}, b_{2,r}, b_{2,1}, b_{2,2}, b_{2,3}, b_{2,4} \\ \ldots, & \ldots, \ldots, \ldots, \ldots, \ldots, \ldots, \ldots \\ b_{n,f}, & b_{n,a}, b_{n,r}, b_{n,1}, b_{n,2}, b_{n,3}, b_{n,4} \end{bmatrix}$$ a [*n* x 7] matrix of regression coefficients

$\vec{Z}$ = a vector of the seven predictor variables (wrist angles and scores) at time t. [7 x 1].

…where *n* is the number of cells (327).

…the prediction algorithm becomes …

$$\hat{\vec{Z}}_t = (B^T \cdot B)^{-1} \cdot B^T (\vec{f}_t - \vec{b}_0) \qquad (20)$$

where …

$\hat{\vec{Z}}_t$ = prediction of wrist angle and scores for first four eigenvectors at time t. [7 x 1].

B^T = the transpose of the coefficient matrix

The last four components of vector $\hat{\vec{Z}}_t$ is a set of scores ([1x4]) of the first four eigenvectors ([20x4]). Multiplying the scores with the transpose of the first four eigenvectors we reconstructed a 20 dimensional representation of the hand at time t.

Following this relatively simple set of equations the firing rates of a motor cortical population were transformed into a predicted representation of average hand shape and orientation. The best correlation between predicted and actual angles using the first four eigenvectors is shown in Figure 71 (small handle). One prediction was made for each sample in

the averaged 100 point trajectory. Each blue curve represents average angles for a joint. The red curve shows the predicted joint angles. The average correlation coefficient across all joints for this prediction was 0.92.

Cross-validation of this fit was performed by separating training and testing data sets with a 70/30 split. The split was across object presentations. There are 64 different presentations, 40 of which were used to calculate a tuning function for each cell (training data), and the firing rates from the other 17 object presentations were used for prediction (testing data). This cross-validation was done over 1,000 different iterations of testing and training data. Those sets that included the small handle extension presentation in the testing are shown in Figure 71B for comparison with the non-validated prediction. The blue trajectories in this plot are the actual joint angles, and the black dots represent predictions from groups of testing data.

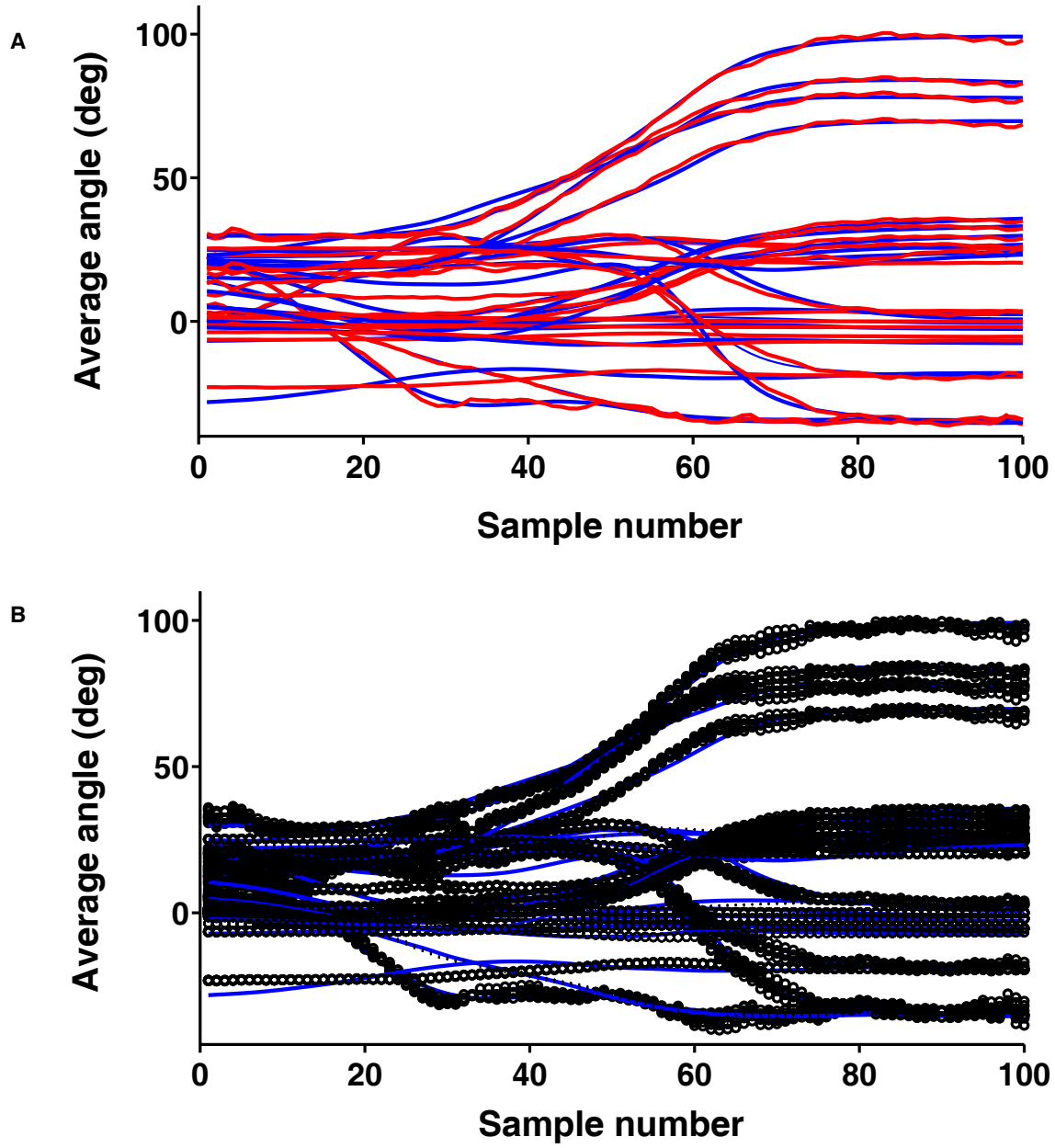

Figure 71. Predicted vs. reconstructed hand shape- small handle.

In Figure A, the blue trajectories show the average joint angle data for presentation of the small hand in the extension position. The red trajectories show the predicted joint angles. Figure B shows the cross-validation of the trajectories in Figure A. The blue curves show the average joint angles for the small handle presented in the extension orientation. The black dots are the cross-validation prediction points.

The trajectory predictions shown in Figure 71 were selected because it represents the best average prediction accuracy. Not all presentations were predicted as accurately, and not all joints were predicted as well as others. Figure 72 compares joint angle prediction accuracy as a function of object presentation. The poorest predicted objects are the button, large rectangle, small and large precision, and the small and large cones. Figure 73 shows the average correlation between predicted and actual hand shape for each joint.

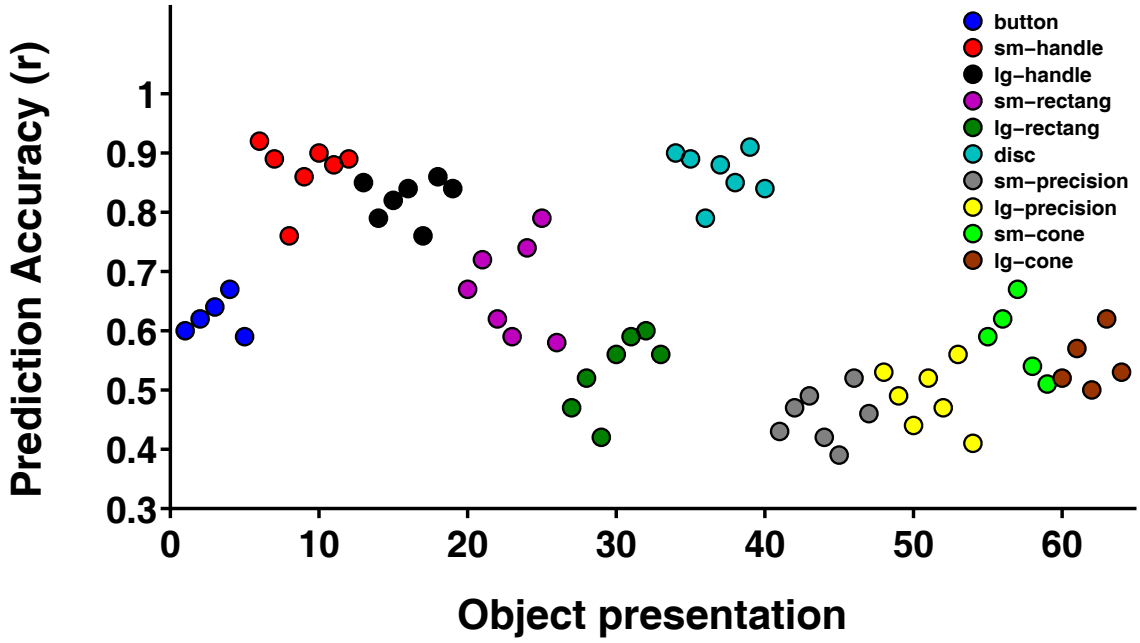

Figure 72. Joint angle prediction correlation as a function of object presentation.

Each dot represents the average correlation coefficient between actual and predicted joint angle across all joints for the designated object presentation. The legend in the upper right hand corner coordinates object and color. The average r-value across all objects is 0.64.

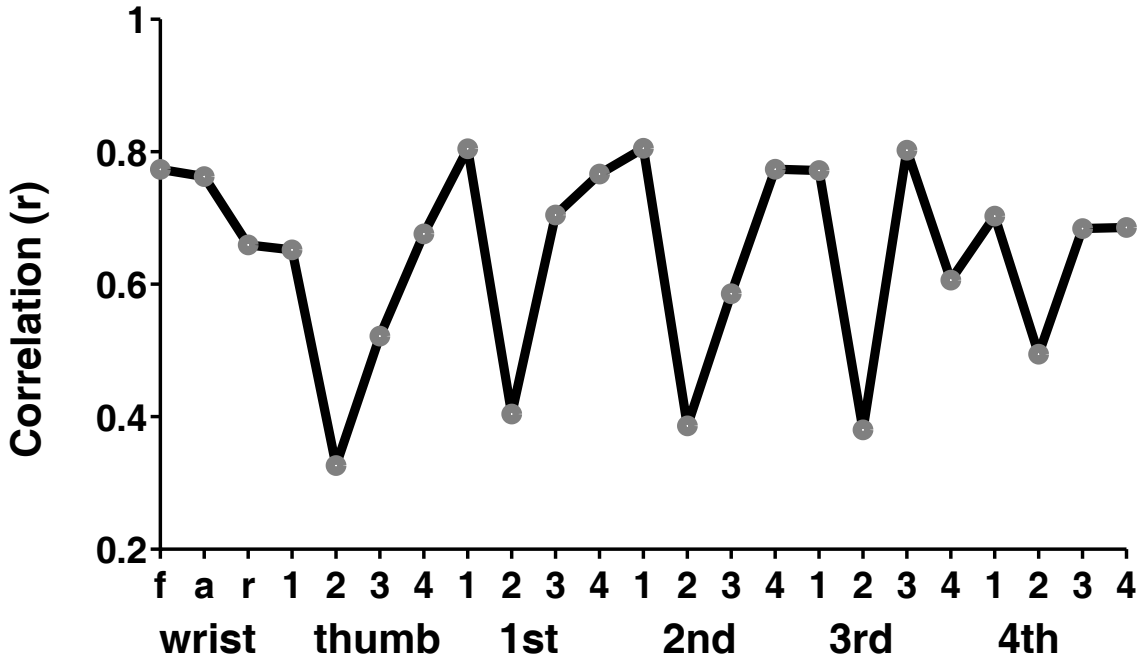

Figure 73. Correlation between actual and predicted hand shape.

This figure shows the average across the 64 presentations. The overall average r value across all joints and all presentations was 0.64.

The average correlation coefficient profile shows that the 2nd DoF for each finger, are the most poorly predicted. These are the MCP abduction joints for the four fingers, and the CMC abduction joint of the thumb. To understand why these joints are poorly predicted we compare these results with the earlier grasping synergies analysis for hand shaping (Figure 74). The joints that are poorly predicted have two similar features. They are those with a minimal amount of variability across many object presentations, and are poorly characterized by the first four eigenvectors.

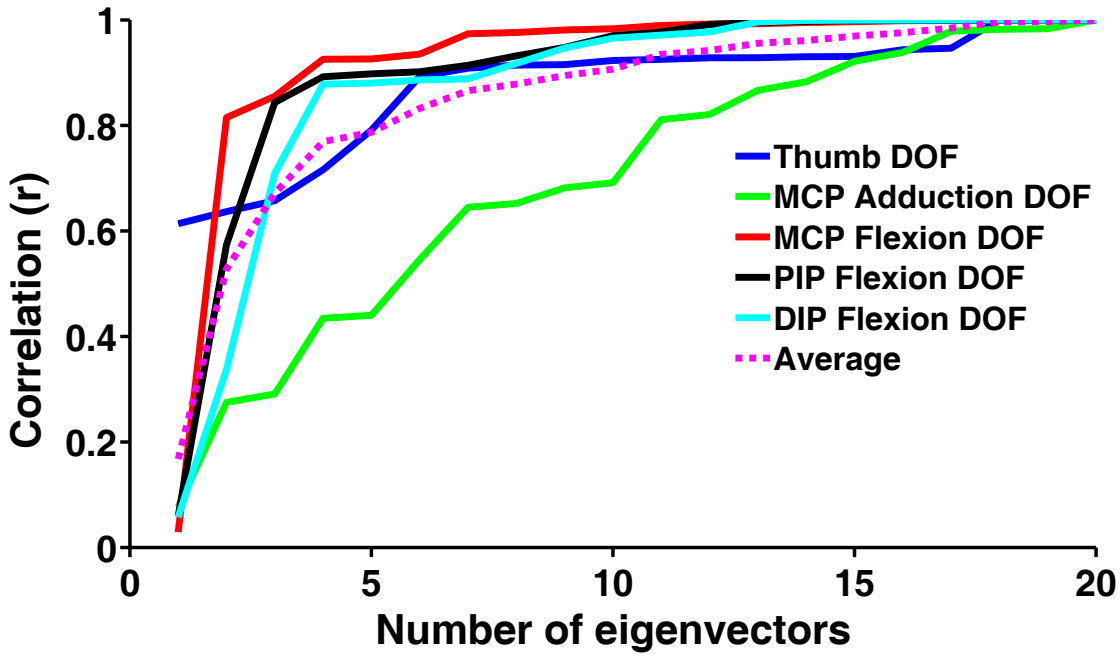

Figure 74. Correlation between actual and reconstructed joint angles for all eigenvectors.

The y-axis is the correlation coefficients between actual and eigenvector reconstructed joint angle data. The x-axis shows the number of eigenvectors used for reconstruction. The dashed line is the average correlation. The blue curve is the correlation data for the Thumb DoFs, green is the MCP abduction/adduction DoFs, red is the MCP flexion/extension DoFs, black is the PIP DoFs, and the light blue is the DIP DoFs.

In this section we showed that a population of motor cortical cells is tuned to grasping synergies. This population was used to predict the weighting of these synergies along with three wrist DOFs. The overall correlation between the average hand shape and orientation predictions using 327 motor cortical cells was 0.64. The prediction equations presented in this section may be a useful starting point for control of a motor restorative device.

5.3 SYNERGY CORRELATIONS WITH MOTOR CORTICAL FIRING

We have shown that monkey grasping kinematics is well represented with only a few patterns (Kinematics Chapter 3). In previous sections (5.2) we also showed that the correlation between individual motor cortical spiking activity and these patterns of movement can be approximated by a linear function. We used this representation to predict hand shape from spiking activity (5.3). In general this worked well, however we noted a consistent pattern in the data that did not fit this simple model. The portion of the data with poor fits corresponded to the same portion that was poorly captured in the data dimensionality reduction algorithm. This suggests that the motor cortex may be directing hand movements using a simplified representation, and thus motivated the following analysis.

In order to analyze preference between single joints and synergies we have transformed our data sets for easy comparison. All of the joint angle data, synergy data, and motor cortical spiking data were concatenated into three separated matrices. The data was calculated using an average angle over a 30ms bin, average score in the same bin, and 30ms binned fractional interval rates. The lag between spiking activity and kinematics was a constant 150ms. The same cells used for prediction in section 5.2 are included in this analysis.

We analyzed the correlation between grasping synergy and joint angles as a function of individual cells. The initial portion of this analysis was to separate synergies from joints based on the rank order of R^2 values from linear regressions. We calculated a rank vector for each cell. The best synergy was established with a separate single linear regression between the firing rate vector and each set of scores. The best corresponding eigenvector was placed in the first position

of a rank vector. Another set of regressions were performed with the best set of scores held constant and all other sets changed. This step consisted of 19 separate two coefficient regressions. The second eigenvector corresponding to the highest two coefficient R^2 was placed in the second position of the rank vector. This iterative process was continued until all eigenvectors were placed in the rank vector. The individual joints were treated in a similar fashion. Examples of normalized individual cell R^2 profiles are shown in Figure 75. The R^2's were normalized so that the maximum for each cell was one, and for easy comparison of profiles across the population.

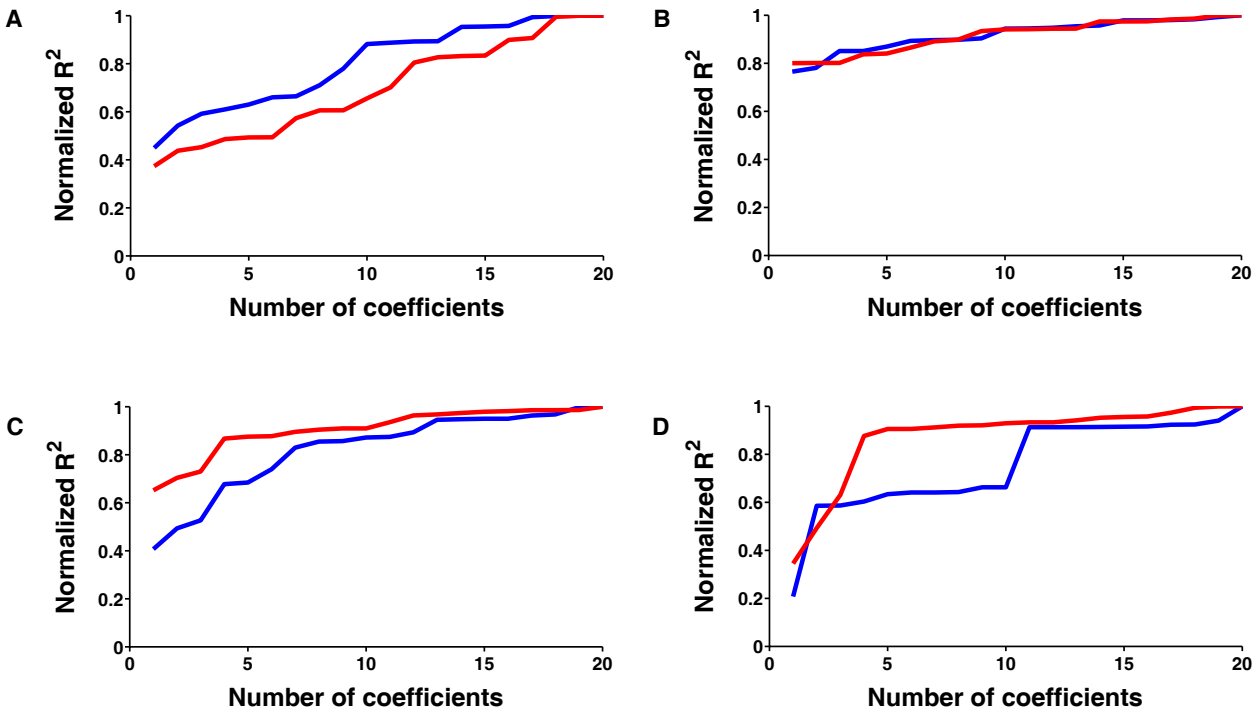

Figure 75. Example R^2 profiles.

The blue line represents the R^2 profile for a cell as a function of the best joints. The first joint is that with the highest R^2, and the last joint is that with the lowest. The red curve represents the R^2 profile for synergies. On the x-axis the number of coefficients corresponds with the number of variables included in the linear regression. Figure

A shows a ‘joint cell’, and Figure C shows a ‘synergy’ cell. Figure B shows a cell that does not show drastic changes in R^2 with increasing the number of coefficients. Figure D shows a cell that shows sharp changes with the addition of just a few coefficients.

The individual cell profiles (Figure 75) show that some cells have incremental increases in R^2 values with an increasing number of regressors. Others show little change with number of coefficients, while others show sweeping changes for joint angles or synergies when just a few coefficients are added. Figure 75A shows and example of a ‘joint’ cell and Figure B shows an example of a ‘synergy’ cell. The average profile for all 327 neurons included in the analysis is shown in Figure 76.

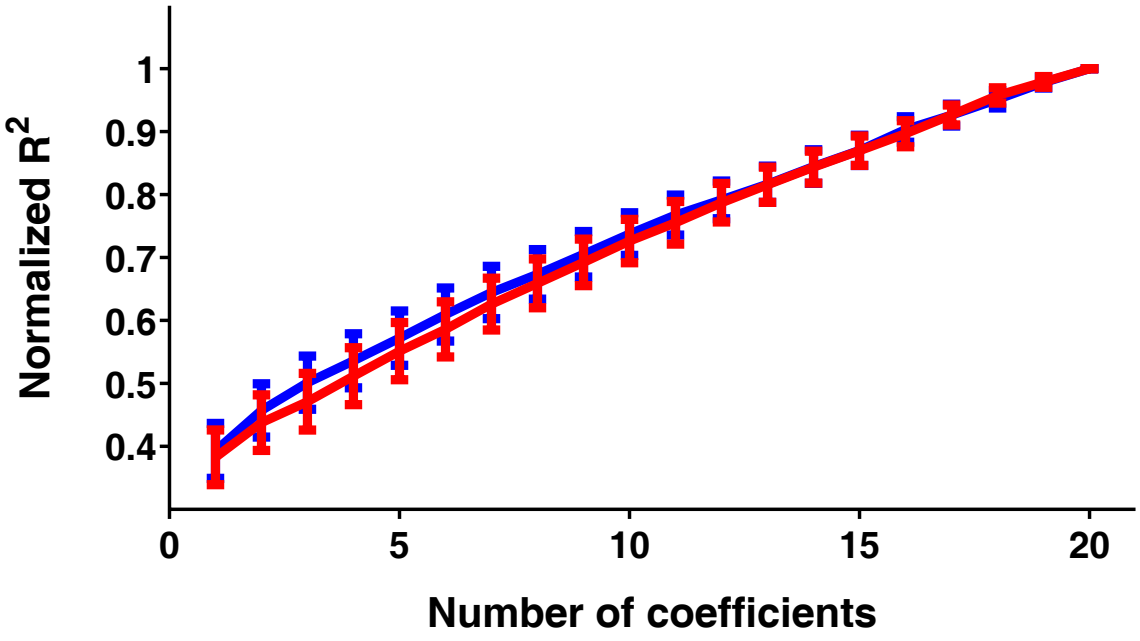

Figure 76. Average R^2 profile for all cells.

The blue line represents the average R^2 profile for joints. The red curve represents the average R^2 profile for synergies. On the x-axis the number of coefficients corresponds with the number of variables included in the linear regression.

If the general trend was that the best linearly correlated DoFs was a synergy, over a joint, this may hint that the population of cells was utilizing the synergies as a fundamental construct for neural control. This, however, was not the case. Although individual R^2 profiles show differences for single joints compared to synergies, there was no significant difference across the population. Even though we have established that the average R^2 profiles are not different, we have not investigated which synergies occupy the first position in the rank order vector. It is reasonable to believe that those joints that contribute to the majority of the variance in kinematic space are well represented in the neural code. This assumption would be reflected in the analysis by having a majority of cells with lower order synergies occupying the first position in the rank order R^2 vector. To investigate this we looked at which synergies are the 'winners' (Figure 77).

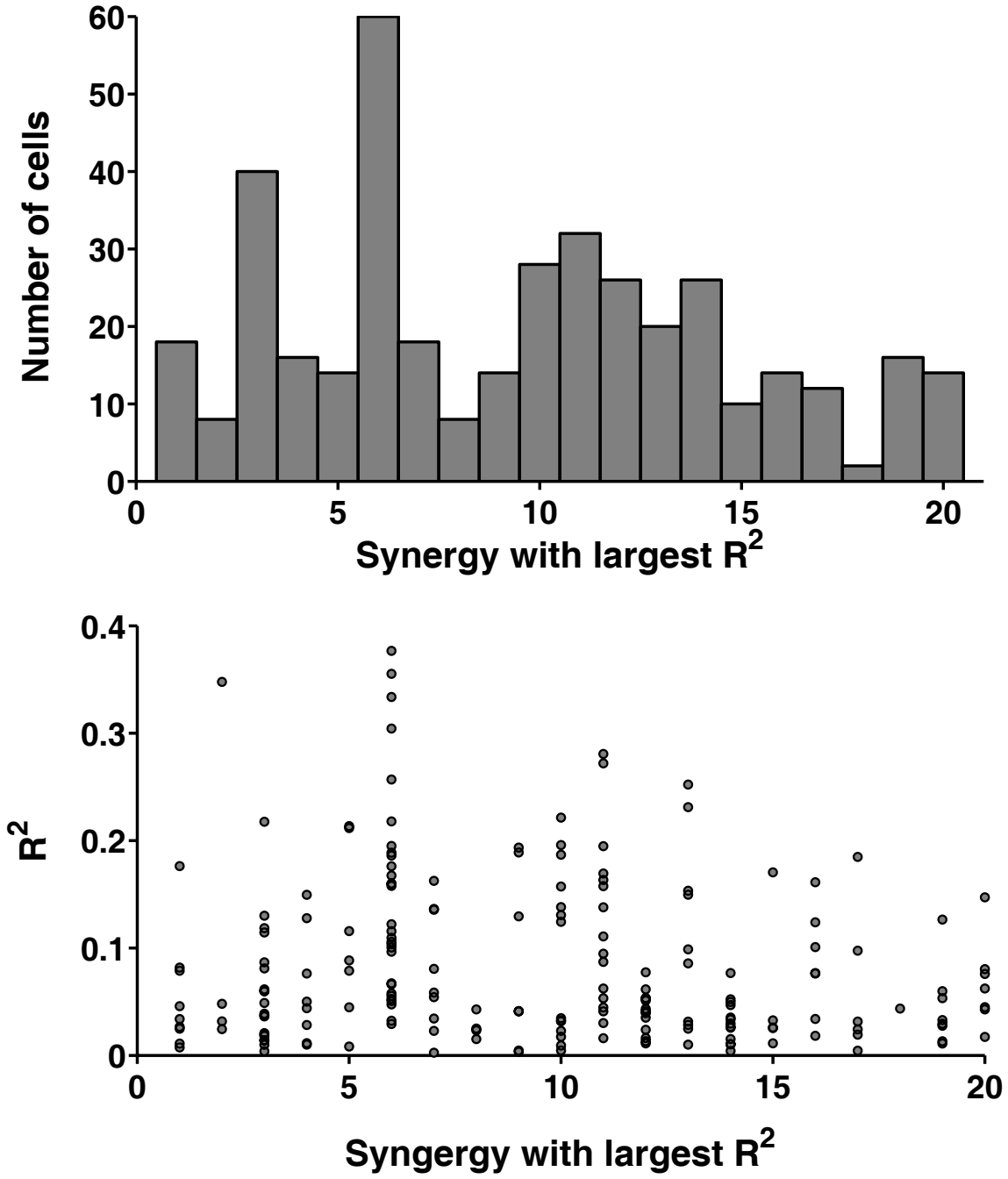

Figure 77. Best correlated synergies.

The top panel shows a histogram of the synergies with the highest R^2 values in the linear regression. The lower panel shows the relationship between R^2 and the best synergy.

The distributions of synergies that represent the first position in the rank order matrix are not skewed in favor of the lower order synergies. In fact, the cells that are best linearly correlated with higher-order synergies are equally well represented as those best correlated with lower order synergies (75% of population). This is surprising since the higher order synergies are often considered to represent complex movements and account for little variability in the joint angle data. This suggests that if the motor cortex is utilizing a simplifying strategy to direct hand shaping, it has not been captured by the eigenvectors from the kinematic data. In other words, the reduced dimensional kinematic space does not capture the majority of variance in the neural space. Another conclusion from this data is that motor neurons may be directing fine adjustments to complex movements versus controlling the majority of kinematic variability.

Although the population R^2 profiles do not differentiate between synergies and joints, some of the individual cells did. In order to further investigate this, we isolated the cells with a large difference in the sum of the first three R^2 values in the rank order matrix for both joints and synergies. The cutoff value used for a cell to be included in this analysis was 30% larger than the comparable R^2 sum. For instance; the sum of the best three synergy R^2s had to be 30% bigger than the sum of the best three joint R^2's, for a cell to be labeled a 'synergy cell'. The same was true for a 'joint cell'. This perturbation produced two data sets. One group of cells that was more correlated with synergies and the other more correlated with joints. The synergy data set had 30 cells, and the joint set had 54 cells. The first three synergies corresponding to both of these data sets are shown in Figure 78.

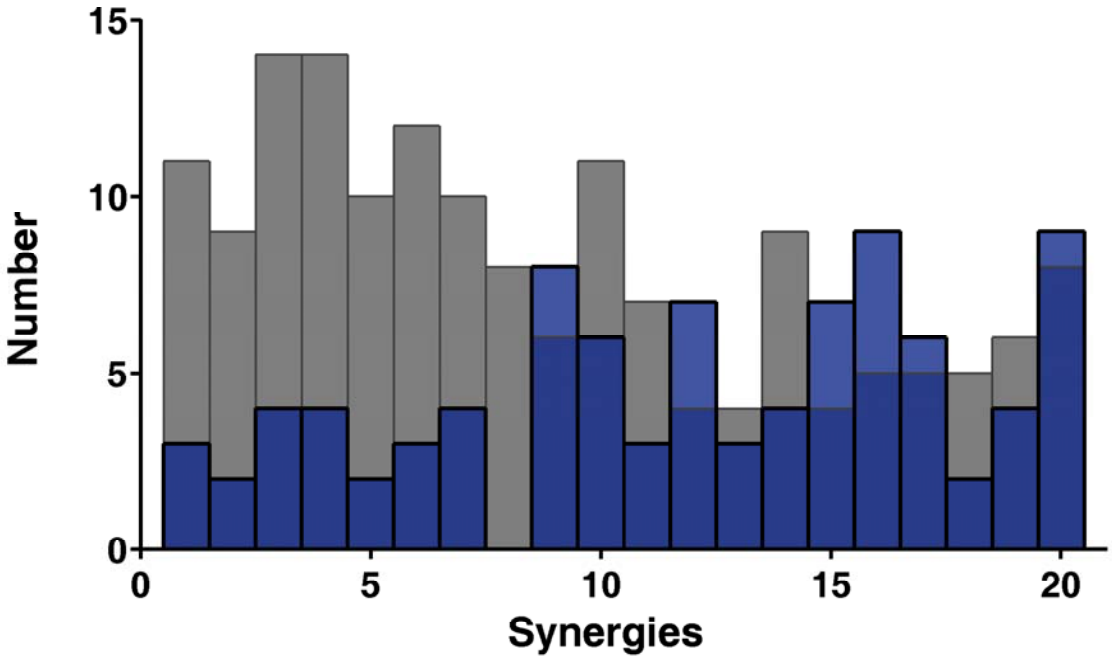

Figure 78. Top three synergies for joint and synergy cells.

The gray distribution shows the top three synergies for the 'joint' cells. The blue plot is the distribution of the top three synergies for the 'synergy' cells.

The distribution of the top three synergies from the rank order matrix shows a stark difference in which synergies are correlated with a 'synergy' cell and a 'joint' cell. Cells that are most correlated with synergies tend to prefer higher order synergies. Stated another way, cells that are most correlated with joints are poorly correlated with lower order synergies. However, the joints to which they were best related are those that are prominent in low order synergies. The separation of lower order and higher order synergies reflect past observation of motor control.

It has been hypothesized that movement is separated into two broad categories; least automatic and most automatic [17]. The least automatic movements are the fine/complex adjustments made to an underlying course ballistic behavior. This type of grasping movement is

only found in higher order primates. On the contrary, most automatic movements refer to those behaviors that are found in early primate infants and lower order species. In relation to the current work, the higher order synergies may represent the least automatic movements and the lower order synergies the most. In a closely related topic, Strick and colleagues [96] raised the notion that motor cortex is organized into two distinct regions based on the differential distribution of cortico-motorneuronal cells. These areas are called “new” and “old” motor cortex. “Old” motor cortex being those cells located near the precentral gyrus, while the “new” motor cortex consists of many cortico-motorneuronal cells in/near the anterior bank of the central sulcus. It is hypothesized that old M1 directs the most automated motor movements, while new M1 directs the least automatic. We investigated the distribution of the best synergy for cells as they relate to the position in recording chamber (Figure 79). A color-map was created progressing from blue (lower-order synergies) to red (higher-order synergies). Qualitatively it is difficult to assess a pattern of color as a function of recording location. However, a correlation becomes clear if we investigate the proximity to central sulcus (Figure 80). A significant ($p<0.05$) correlation exists between a cells likelihood of the best synergy being higher order and proximity to the central sulcus. There is also a significant correlation between lower-order synergies and a more lateral recording site, and no correlation between best joint and recording site.

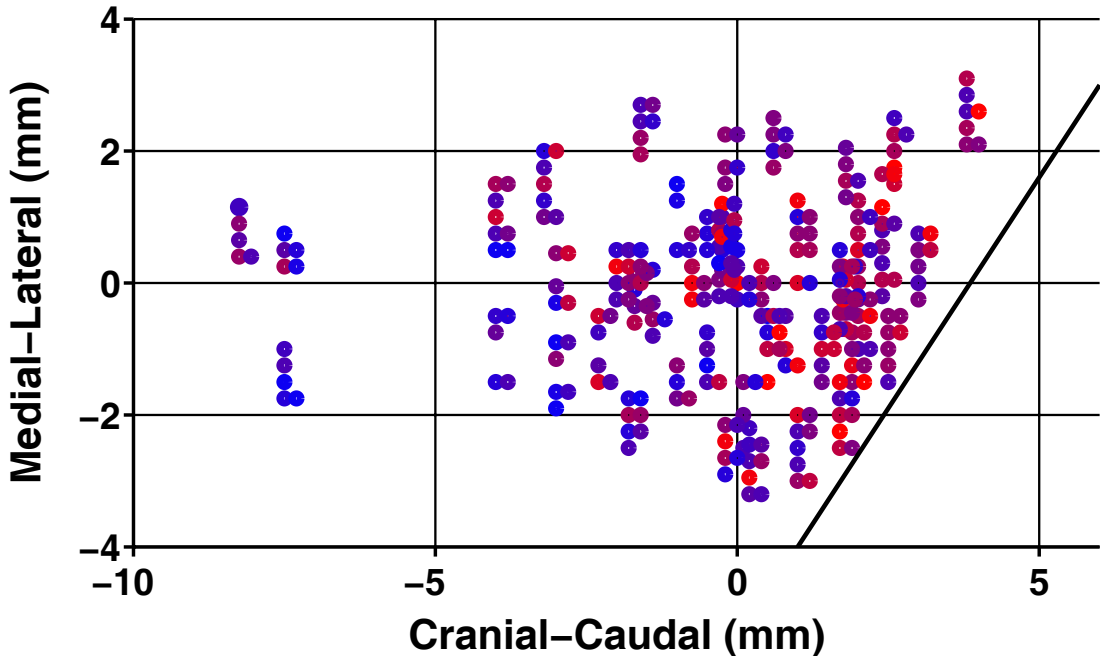

Figure 79. Best synergy as a function of penetration site.

Illustration of all penetration sites for two monkeys, and three hemispheres, overlaid onto one left hemisphere plot. The black diagonal line represents the central sulcus. Each circle shows an electrode penetration site where a cell was recorded. The sites have been color coded according to the best synergy. The color map is from blue to red going from lower → higher order synergies.

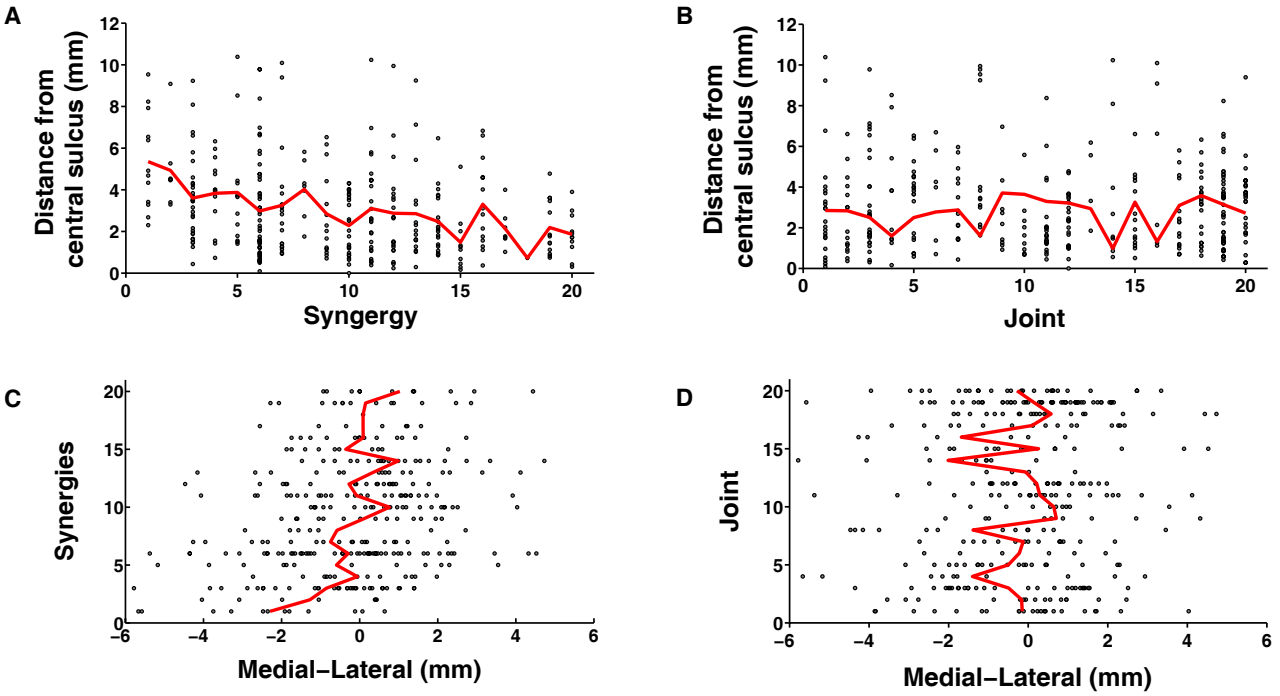

Figure 80. Best synergy as a function of chamber position.

Figures A and B show the best synergy and joint, respectively, as a function of proximity to the central sulcus. Figures C and D show the medial-lateral location in the chamber as a function of best synergies and best joints.

5.4 DISCUSSION

The correlation between motor cortical cells' firing rate and joint angle, velocity and synergies can be approximated with a linear function. This linear fit was constructed based on three wrist DoFs and the scores of the first four eigenvectors. The same tuning function obtained for a single cell can be transformed into a predictive model when using a population of cells. Even though

individual cells are poorly tuned to a single variable, the tuning to many variables, combined with many cells, results in accurate prediction of hand shape. The prediction reconstructions show that the most poorly predicted joints are the abduction joints (CMC of the thumb and the MCP joints of the fingers). These also correspond with the joints most poorly characterized by the first few eigenvectors. If more eigenvectors were used for reconstruction the prediction reconstruction accuracy for these joints may have been higher.

The lower dimensional representation of the hand accounts for the majority of the variability in the kinematic space. If the same reduced-dimensional transformation is applied to the neural data, we may predict that the firing rates would mostly be correlated with lower order synergies. This however, was not the case. Both higher-order and lower-order synergies are well represented in the neural data. This suggests that although we have chosen a model that reduces kinematic variability, it is not the model of choice to capture the majority of neural variability.

We can separate the neural data into two general types of cells; those with a higher correlation with a few joints, and those with a higher correlation with a few synergies. Analyzing the groupings of synergies showed that cells more correlated with eigenvectors tend to be correlated with higher-order synergies. This provides a level of support for the idea that this group of cells may be contributing to fine adjustments in movement (least automatic). We find that cells closer to the central sulcus tend to be best correlated with higher-order eigenvectors.

Cells that are more correlated with higher-order synergies are by definition not correlated as well to the majority of variability in hand shaping. It may be that the cells associated with

higher-order components are coding for fine adjustments to movements accounting for little variability in the kinematic space. The idea that these cells are more likely to be found near the central sulcus supports the idea that these may be ‘new M1’ cells [96]. These cells may also represent just a small portion of a larger network that directs hand movement utilizing an undiscovered method of encoding.

6.0 CONCLUSIONS

This chapter wraps up the findings from the previous three chapters. The section starts with a synthesis of the main findings from this work (6.1) with a focus on wrist DoFs, hand kinematics, and the relationship between motor cortical firing with wrist and hand movements, and concludes with a discussion on future work (6.2).

6.1 SUMMARY OF MAIN CONCLUSIONS

The main finding from this work is that individual motor cortical neurons are not well correlated with single joint variables; rather, they correlate with a number of joints in a complex way. This work provides evidence that hand movements are likely controlled through an intricate network of motor systems, of which motor cortical neurons contribute by making fine adjustments to a basic substrate. These conclusions accrued from analyzing a lower dimensional representation of hand kinematics (synergies) (3.4), neural correlation with three wrist DoF (4.0), and neural correlation to the aforementioned synergies (5.0).

We found that the kinematics of the three wrist DoFs (flexion, abduction and rotation) were rashly independent from hand-shape DoFs, and were considered separately for kinematic

(4.1.2) and neural analysis (4.2). With respect to the wrist DoFs; in early training sessions, wrist angles were poorly correlated compared with late sessions. It appeared that this change was associated with an increase in the number of trials performed daily. It was concluded, that this may represent an energy conservation strategy optimizing for increasing the number of rewards per day. The neural correlations to these variables were treated separately based on the naturally uncorrelated nature of the movements (i.e. early training session).

The pattern of firing of individual motor cortical cells can be approximated by a linear function related to change in wrist variables (4.2). Based on single DoF linear regressions, wrist position was better correlated to spiking activity than wrist velocity. The coefficients from multivariate regressions (b coefficients) were normalized to a unit vector, a preferred direction (pd). The length of the sum of these vectors, measure of uniformity, was not significantly different from the length of summed vectors drawn from a truly uniform population. This suggests that the cells we sampled were drawn from a population with a uniform distribution of pd's, and that no single wrist DoFs is more represented in motor cortex than any other (4.4).

The tuning functions constructed for 200 cells were used in an optimal linear estimator to predict wrist DoFs from neural firing rates. The average wrist angle prediction closely approximated the actual wrist angle (4.4). This simple transformation from firing rate to wrist angle may be implemented in future real-time decoding algorithms for neural control of a three DoFs robotic wrist. This achievement would nearly double the controlled DoFs of the most advanced motor restorative prosthetic [71]. A significant improvement beyond wrist control would be to also direct the DoFs of the hand.

We used principal components analysis to simplify the complex kinematics of the hand (3.3.3). The general characteristics of hand movement, and more specifically the synergies, appear to be closely associated to that of humans (3.4.2). Although the kinematic synergies did not fully characterize neural firing, they were utilized to simplify hand shape decoding. Using an optimal linear estimator, we predicted the average wrist and hand shape from the firing rates of 327 motor cortical cells with an accuracy as high as 92%.

This accuracy was surprising given the relatively poor correlation of single cell activity to individual joints (5.1). The population of cells appeared to be more correlated with a number of joints in a complex way. The average prediction accuracy across all object presentations for all 20 DoFs of hand shaping was 64% (5.2). The majority of prediction error was accounted for by a poor estimate of the MCP abduction DoFs. This inaccuracy was predictable based on the joint variability accounted for by the lower dimensional kinematic model. (3.4.2).

The relatively even distribution of “best” synergies in the population suggests that the lower dimensional kinematic model is not the simplified representation the motor cortical system utilizes for directing hand movement. Further understanding of the control system will be gained by establishing a model that captures both the hand kinematic and neural variability.

6.2 FUTURE WORK

6.2.1 Lower dimensional representation of neural data

The lack of our ability to capture the majority of variability in the neural firing rate data by the synergies derived from kinematic data provides compelling evidence that we do not have an adequate understanding about the relationship between motor cortical firing and complex hand shaping. If the motor cortical system does utilize a simplified representation of the hand for control, it is not what we have uncovered in our experiment. It is possible that the best lower dimensional model is a non-linear representation of hand kinematics, or a simple linear transformation of the synergies in this work, or a force based model, etc. However, the number of possible representations that the motor system has adopted for hand control throughout evolution is endless. Correlating different transformations of kinematic data with neural data is not likely the most efficient approach, nor will it likely produce more than incremental progress to the current study. Applying a method that captures a lower dimensional representation of both kinematic and neural data simultaneously (i.e. conical correlation) is a better approach. Further understanding of the components that establish the structured relationship between a cell firing and hand movement will provide significant progress in a complex area of neurophysiology.

6.2.2 Furthering the current study

The current experimentation is more of a ‘first of its kind’ study, than a validation of past experiments. This work has provided insight into some details of high dimensional motor control analysis, yet has left much to be desired. In the current work kinematic data was collected

simultaneously with neural recordings from the motor cortex. One type of data not collected in this experiment is the spiking activity from arm and hand musculature. The current study has been expanded (Sagi Perel) to include EMG data from 16 muscles in the arm and hand along with hand kinematics and individual motor cortical spiking activity. We hope to further elucidate strategies adopted by the network of motor control systems involved with the complexities of grasping behavior.

6.2.3 Motor restorative devices

The predictive algorithms used in this work provide evidence that a high dimensional brain machine interface may be guided by the firing of population of motor cortical cells. The number of cells used in this work for prediction was relatively high compared to simultaneous neural recordings. This study also predicted average hand shapes and wrist orientations from average firing rates, a luxury unknown in real-time experimentation. It is difficult to extrapolate, with any certainty, the likely number of cells necessary for such work based on the current study. Even with a large population of simultaneously recorded cells, complex control of a high DoFs neural controlled device is a formidable challenge.

We are fortunate enough to have an active neural prosthetics program in our lab. The focus of this program is the neural control of complex, and high DoFs, robotic arms, wrists and hands. The current state-of-the-art neural controlled robotic device guides 4 independent DoFs [71]. A robotic arm, wrist and hand in our lab will soon have the same number of DoFs as a human hand. The predictive equations in this work indicate that we can direct seven independent

DoFs of the wrist and hand. These seven dimensions can be mapped onto a 23 DoFs robotic system to direct all DoFs simultaneously. Controlling a robotic hand by decoding a few synergies will sacrifice some ability for individuated finger movements, but may provide a predictable constraint on the neural decode based in physiology.

BIBLIOGRAPHY

[1] C.R. Mason, J.E. Gomez, T.J. Ebner. Hand Syngergies During Reach-to-Grasp. The Journal of Neurophysiology Vol. 86 No. 6 December 2001, pp. 2896-2910

[2] J.F. Soechting, M. Flanders. Flexibility and repeatability of finger movements during typing: analysis of multiple degrees of freedom. *J Comput Neurosci* 4: 29–46, 1997.

[3] J.M.F. Landsmeer. The coordination of finger-joint motions. *J Bone Joint Surg* 45A: 1654–1662, 1963.

[4] J.M.F. Landsmeer, C. Long. The mechanism of finger control based on electromyograms and location analysis. *Acta Anat* 60: 330–347, 1965.

[5] C. Long, P.W. Conrad, E.A. Hall, S.L. Furler. Intrinsic-extrinsic muscle control of the hand in power grip and precision handling. *J Bone Joint Surg* 52A: 853–867, 1970.

[6] J.R. Napier. The prehensile movement of the human hand. *J Bone Joint Surg* 38B: 902–913, 1956.

[7] M.F. Marzke, R.F. Marzke. Evolution of the human hand: approaches to acquiring, analysing and interpreting the anatomical evidence. *J. Anat.* 2000;197:121–140.

[8] R.W. Young, Evolution of the human hand: the role of throwing and clubbing. *Journal of Anatomy* 2003, 202(1): 165-174.

[9] R.W. Young, Human evolution: The role of throwing and clubbing. *Current Anthropol* 2002

[10] J.R. Napier. The form and function of the carpo-metacarpal joint of the thumb. *J. Anat.* 1955;89:362–369.

[11] J.R. Napier. Studies of the hands of living primates. *Proc. Zool. Soc. London.* 1960; 134: 647–657.

[12] J.R. Napier. Evolution of the human hand. *Proc. Royal. Inst. Great Britain.* 1965;40:544–557.

[13] J.R. Napier. Hands. *Princeton, New Jersey: Princeton University Press*; 1993.

[14] M.W. Marzke, R.F. Marzke. The third metacarpal styloid process in humans: origin and functions. *Am. J. Phys. Anthropol.* 1987;73:415–431.

[15] M.W. Marzke, K.L. Wullstein. Chimpanzee and human grips: a new classification with a focus on evolutionary morphology. *Int. J. Primatol.* 1996;17:117–139.

[16] M.W. Marzke. Evolution of the hand and bipedality. *Handbook of Human Symbolic Evolution.* Oxford: Oxford University Press; 1992a. pp. 126–154.

[17] C.G. Phillips, R. Porter. Corticospinal Neurones: Their Role in Movement. *Monographs of the physiological society.* 1977: 321-402.

[18] S.S. Towers. Pyramidal lesion in the monkey. *Brain*, 1940;63:36-90.

[19] D.G. Lawrence, H.G.J.M. Kuypers. The functional organization of the motor system in the monkey. I. The effects of bilateral pyramidal lesions. *Brain*, 1968;91:1-14.

[20] M.C. Hepp-Reymond, E. Trouche, M. Wiesendanger. Effects of unilateral and bilateral pyramidotomy on a conditioned rapid precision grip in monkeys (Macaca fascicularis). *Expl Brain Res.* 1974;21:519-527.

[21] A.M. Gordon, A. Casabona, J.F. Soechting. The learning of novel finger movement sequences. *J Neurophysiol* 72: 1596-1610, 1994

[22] M. Schieber. Individuated finger movements of Rhesus monkeys: a means of quantifying the independence of the digits. *J Neurophysiol* 1991: 65; 1381–1391.

[23] M. Schieber. How might the motor cortex individuate movements? *Trends Neurosci* 1990: 13; 440–445.

[24] A. Bishop. Use of the hand in lower primates. *Evolutionary and Genetic Biology of Primates* (Ed. J. Buettner-Janusch), Academic Press, New York. 1964: Vol. 2; 133-225.

[25] Schieber, M.H., Hibbard, L.S. How somatotopic is the motor cortex hand area? *Science* 1993: 261; 489–492.

[26] A.V. Poliakov, M.H. Schieber. Limited functional grouping of neurons in the motor cortex hand area during individuated finger movements: a cluster analysis. *J Neurophysiol* 1999 82: 3488–3505.

[27] M.H. Schieber. Motor cortex and the distributed anatomy of finger movements. *Adv Exp Med Biol*. Aug, 12th 2002; 508.

[28] Y. Shinoda, J.Yokota, T. Futami. Divergent projection of individual corticospinal axons to motorneurons of multiple muscles in the monkey, *Neurosci Lett* 23, 1981: 7-12.

[29] M.H. Schieber, M. Santello. Hand function: peripheral and central constraints on performance. *J. Appl. Physiol.* 2004;96:2293-2300.

[30] M. Flanders, J.F. Soechting. Kinematics of typing: parallel control of the two hands. *J Neurophysiol* 1992;67: 1264–1274.

[31] K.C. Engel, M. Flanders, J.F. Soechting. Anticipatory and sequential motor control in piano playing. *Exp Brain Res* 1997; 113: 189–199.

[32] J. Fish, J.F. Soechting. Synergistic finger movements in a skilled motor task. *Exp Brain Res.* 1992; 91:327-334.

[33] D.J. Guirintano, A.M. Hollister, W.L. Buford, D.E. Thompson, L.M. Myers. A virtual five-link model of the thumb. *Medical Engineering and Physics* 1995;17:297-303.

[34] C.G. Phillips. Evolution of the corticospinal tract in primates with special reference to the hand. *Proc. 3rd Int. Congr. Primat. Zurich*. 1971; V2;2-23.

[35] M. Santello, M. Flanders, J.F. Soechting. Postural hand synergies for tool use. *J Neurosc.i* 1998; 18: 10105–10115.

[36] M. Santello, J.F. Soechting, Gradual molding of the hand to object contours. *J Neurophysiol* 1998; 79: 1307–1320.

[37] – M. Santello, J.F. Soechting. Matching object size by controlling finger span and hand shape. *Somatosens Mot Res* 1997; 14: 203-212.

[38] M. Jeannerod. Intersegmental coordination during reaching at natural visual objects. In: *Attention and Performance IX*, edited by Long J and Baddeley A. Hillsdate, NJ: Erlbaum, 1981; 153-185.

[39] M. Jeannerod, B. Biguer. Visuo-motor mechanisms in reaching within extrapersonal space. In: *Advances in the Analysis of Visual Behavior*, edited by Ingle D, Goodale MA, and Mansfield R. Boston, MA: MIT Press, 1982; 387-409.

[40] M. Jeannerod, The timing of natural prehension movements. J Mot Behav 1984; 16: 235–254**.**

[41] R.G. Marteniuk, J.L. Leavitt, C.L. MacKenzie, C.G. Atkeson. Functional relationships between grasp and transport components in a prehension task. *Hum Move Sci* 1990; 9: 149-176.

[42] M.A. Arbib, T. Iberall, D. Lyons. Coordinated control programs for movements of the hand. *Exp Brain Res Suppl* 1985; 10: 111–129.

[43] T. Iberall, A. Fagg. Neural networks for selecting hand shapes. In: *Hand and Brain: The Neurophysiology and Psychology of Hand Movements*, 1996; 243–264.

[44] A.C. Roy, Y. Paulignan, A. Farne, C. Jouffrais, D. Boussaoud. Hand kinematics during reaching and grasping in the macaque monkey. *Behav Brain Res* 2000; 117: 75-82.

[45] A.C. Roy, Y. Paulignan, M. Meunier, D. Boussaoud. Prehension movements in the macaque monkey: effects of object size and location. *J Neurophysiol* 2002; 88: 1491-1499.

[46] C.R. Mason, L.S. Theverapperuma, C.M. Hendrix, T.J. Ebner. Monkey hand postural synergies during reach-to-grasp in the absence of vision of the hand and object. *J. Neurophysiol*. 2004; 91: 2826-2837.

[47] P.H. Thakur, A.J. Bastian, S.S. Hsiao. Multidigit movement synergies of the human hand in an unconstrained haptic exploration task. *J. Neurosci* 2008; 6:28(6):1271-81.

[48] P.R. Kennedy, R.A.E. Bakay. Restoration of neural output from a paralyzed patient by a direct brain connection. *Neuroreport* 1998; 9: 1707-1711.

[49] P.R. Kennedy, R.A.E. Bakay, M.M. Moore,K. Adams, J. Goldwaithe. Direct control of a computer from the human central nervous system. *IEEE Trans. Rehabil. Eng.* 2000; 8: 198-202.

[50] J. Wessberg, C.R. Stambaugh, J.D. Kralik, P.D. Beck, M. Laubach, J.K. Chapin, J.B. Kim, M.A. Srinivasan, M.A.L. Nicolelis. Real-time prediction of hand trajectory by ensembles of cortical neurons in primates. *Nature* 2000; 408: 361-365.

[51] M.D. Serruya, N.G. Hatsopoulos, L. Paninski, M.R. Fellows, J.P. Donoghue. Instant neural control of a movement signal. *Nature* 2002; 416: 141-142.

[51] J.R. Wolpaw, D.J. McFarland. Control of a two-dimensional movement signal by a noninvasive brain-computer interface in humans. *Proceedings of the National Academy of Sciences of the USA* 2004; 101: 17849-17854.

[52] G. Santhanam, S.I. Ryu, B.M. Yu, A. Afshar, K.V. Shenoy. A high-performance brain-computer interface. *Nature*. 2006; 442:195-198.

[53] A.I. Nobunaga, G.K. Go, R.B. Karunas. Recent demographic and injury trends in people served by the Model Spinal Cord Injury Systems. *Arch Phys Med Rehabil*. 1999; 80: 1372-1382.

[54] A.P. Georgopoulos, J.F. Kalaska, R. Caminiti, J.T. Massey. On the relations between the direction of two-dimensional arm movements and cell discharge in primate motor cortex. *J. Neuroscience*. 1982; 2(11): 1527-37.

[55] A.P. Georgopoulos,J.F. Kalaska,M.D. Crutcher, R. Caminiti, J.T. Massey. in *Dynamic Aspects of Neocortical Function* (eds. Edelman, G. M., Goll, W. E. & Cowan, W. M.) 1984; 501-524.

[56] A.P. Georgopoulos, A.B. Schwartz, R.E. Kettner. Neuronal population coding of movement

direction. *Science* 1986; 233:1416-1419.

[57] A.P. Georgopoulos, R.E. Kettner, A.B. Schwartz. Primate motor cortex and free arm movements to visual targets in three dimensional space. II. Coding of the direction of movement by a neuronal population. *J. Neurosci.* 1988; 8: 2928–37.

[58] D.W. Moran, A.B. Schwartz. Motor cortical representation of speed and direction during reaching. *J. Neurophysiol.* 1999; 82: 2676–92.

[59] A.B. Schwartz. Motor cortical activity during drawing movements. Single-unit activity during sinusoid tracing. *J. Neurophysiol*.1992; 68: 528–41.

[60] A.B. Schwartz. Motor cortical activity during drawing movements: population response during sinusoid tracing. *J. Neurophysiol.* 1993; 70: 28–36.

[61] A.B. Schwartz. Neuronal substrate for volitional movement. In: *Insights into the Reach to Grasp Movement*. Eds: K.B.B. Bennett and U. Castiello. Elsevier Science B.V., 1994; 59-83.

[62] A.B. Schwartz, D.W. Moran. Motor cortical activity during drawing movements: population representation during lemniscate tracing. *J. Neurophysiol.* 1999; 82: 2705–18.

[63] A.B. Schwartz. Cortical neural prostheses, *Ann. Rev. Neurosci*, 2004; 27: 487-507.

[64] A.B. Schwartz, X.T. Cui, D.J. Weber, D.W. Moran, Brain-Controlled Interfaces: Movement Restoration with Neural Prosthetics, *Neuron*, 2006; 52: 1-16.

[65] D.M. Taylor, S.I. Helms Tillery, A.B. Schwartz. Direct control of 3D neuroprosthetic devices. *Science* 2002; 296: 1829-1832.

[66] M.D. Serruya, N.G. Hatsopoulos, L. Paninski, M.R. Fellows, J.P. Donoghue. Instant neural control of a movement signal. *Nature*. 2002: 14; 416:141-142.

[67] J.M. Carmena, M.A. Lebedev, R.E. Crist, J.E. O'Doherty, D.M. Santucci, D.F. Dimitrov, P.G. Patil, C.S. Henriquez, M.A.L. Nicolelis. Learning to control a brain-machine interface for reaching and grasping by primates. *PLoS Biology* 2003: 1; 193-208.
.
[68] L.R. Hochberg, M.D. Serruya, G.M. Friehs, J.A. Mukand, M. Saleh, A.H. Caplan, A. Branner, D. Chen, R.D. Penn, J.P Donoghue. Neuronal ensemble control of prosthetic devices by a human with tetraplegia. *Nature*, 2006: 442(7099), 164-171.

[70] K. Sung-Phil, J. Simeral, L. Hochberg, J.P. Donoghue, M.J. Black. Neural control of computer cursor velocity by decoding motor cortical spiking activity in humans with tetraplegia J. Neural Eng.2008: vol. 5, pp. 455-476

[71] M. Velliste, S. Perel, M.C. Spalding, A.S. Whitford, A.B. Schwartz. Cortical control of a prosthetic arm for self-feeding, *Nature* 2008: vol453; 1098-1101.

[72] I.D. Peikon, N.A. Fitzsimmons, M.A. Lebedev, M.A.L. Nicolelis. Three-dimensional, automated, real-time video system for tracking limb motion in brain-machine interface studies. *J. Neurosci. Methods*. 2009; 180: 224-233.

[73] D.G.E. Robertson, G.E. Caldwell, J. Hamill, G. Kamen, S.N. Whittlesey. *Research methods in biomechanics*. Human Kinetics. 2004; 45-52.

[74] I.A. Kapandji. The Physiology of the Joints. Upper Limb (2nd ed.). *London: E and S Livingstone*, 1970; 1: 146–202.

[75] R. Tubiana. Architecture and function of the hand. In: *The Hand*, edited by Tubiana R. Philadelphia, PA: Saunders, 1981, vol. 1, p. 19–93.Walter, W.G. in Consciousness Explained (ed. Dennett, D.C.) 1991; 167.

[76] E. Todorov, Z. Ghahramani. Analysis of the synergies underlying complex hand manipulation, *Proceedings of the 26th Annual International Conference of the IEEE EMBS San Francisco, CA, USA*: 2004

[77] L. Breiman. Random forests. Technical report, Department of Statistics, University of California, 2001.

[78] I.K. Fodor. A survey of dimension reduction techniques. Technical report, Center for Applied Scientific Computing, Lawrence Livermore National Laboratory

[79] N. Cristianini, J. Shawe-Taylor. *An Introduction to Support Vector Machines and other kernel-based learning methods*. Cambridge University Press, 2000.

[80] E.V. Evarts. Relation of Pyramidal Tract Activity to Force Exerted During Voluntary Movement. *J. Neurophysiology*. 1968; 31: 14-27.

[81] D.R. Humphrey. Relating motor cortex spike trains to measures of motor performance. *Brain Research*, 1972; 40: 7-18.

[82] S. Kakei, D.S. Hoffman, P.L. Strick. Muscle and Movement Representations in the Primary Motor Cortex. *Science*, 1999; 285: 2136-2139.

[83] W. Wang, S.S. Chan, D.A. Heldman, D.W. Moran. Motor Cortical Representation of Hand Translation and Rotation during Reaching. *J. Neuroscience*, 2010; 30(3): 958-962.

[84] E. Salinas, L.F. Abbott. Vector reconstruction from firing rates. *Journal of Computational Neuroscience*. 1994; 1: 89-107.

[85] R.E. Kass, V. Ventura, E.N. Brown. Statistical issues in the analysis of neuronal data. *Journal of Neurophysiology*. 2005; 94: 8-25.

[86] S.M. Chase, A.B. Schwartz, R.E. Kass, Bias, optimal linear estimation, and the differences between simulation and closed-loop performance of spiking-based interface algorithms. *Neural Networks* 2009; 1203-1213.

[87] M.C. Spalding, M. Velliste, B. Jarosiewicz, G. Kirkwood, A.B. Schwartz. Direct brain control of an anthropomorphic robotic arm during a feeding task. *2004 Abstract Viewer/Itinerary Planner.* Washington, DC: Society for Neuroscience, 2004.

[88]M.C. Spalding, M. Velliste, B. Jarosiewicz, A.B. Schwartz. 3-D Cortical Control of an anthropomorphic robotic arm for reaching and retrieving. *2005 Abstract Viewer/Itinerary Planner.* Washington, DC: Society for Neuroscience, 2005.

[89] S. Brunstrom. Movement Therapy in Hemiplegia: A Neurophsyiological Approach. New York: Harper and Row, 1970.

[90] C.E. Lang, M.H. Schieber. Differential impairment of individuated finger movements in humans after damage to the motor cortex or the corticospinal tract. J Neurophysiol 2003; 90: 1160-1170.

[91] T. Brochier, M.J. Boudreau, M. Pare, A.M. Smith. The effects of muscimol inactivation of small regions of motor and somatosensory cortex on independent finger movements and force control in the precision grip. Exp Brain Res. 1999; 128: 31-40.,

[92] M.H. Schieber, A.V. Poliakov. Partial inactivation of the primary motor cortex hand area: effects on individuated finger movements. J. Neurosci. 1998; 18: 9034-9054.

[93] [M.H. Schieber, L.S. Hibbard. How somatotopic is the motor cortex hand area? Science. 1993; 261: 489-492.

[94] C.M. Hendrix, C.R. Mason, T.J. Ebner. Signaling of grasp dimension and grasp force in dorsal pemotor cortex and primary motor cortex neurons during reach to grasp in the monkey. *J Neurophysiol*. 2009; 102: 132-145.

[95] J. Zhuang, W. Truccolo, C. Vargas-Irwin, J.P. Donoghue. Decoding 3-D reach and grasp kinematics from high-frequency local field potentials in primate primary motor cortex. *IEEE Transactions in Biomedical Engineering*. 2010.

[96] J.A. Rathelot, P.L. Strick. Subdivisions of primary motor cortex based on cortico-motorneuronal cells. *PNAS* 2009; 106 (3): 918-923.